Probing local quantities in a strongly interacting Fermi gas and the construction of an ultracold Fermi gas apparatus

by

Rabin Paudel

B.A. Physics and Mathematics, Wabash College, 2010

M.S. Physics, University of Colorado, 2013

A thesis submitted to the

Faculty of the Graduate School of the

University of Colorado in partial fulfillment

of the requirements for the degree of

Doctor of Philosophy

Department of Physics

2017

This thesis entitled:
Probing local quantities in a strongly interacting Fermi gas and the construction of an ultracold Fermi gas apparatus
written by Rabin Paudel
has been approved for the Department of Physics

Prof. Deborah Jin (deceased)

Prof. Eric Cornell

Prof. Cindy Regal

Date

The final copy of this thesis has been examined by the signatories, and we find that both the content and the form meet acceptable presentation standards of scholarly work in the above mentioned discipline.

Paudel, Rabin (Ph.D., Physics)

Probing local quantities in a strongly interacting Fermi gas and the construction of an ultracold Fermi gas apparatus

Thesis directed by Prof. Deborah Jin (deceased)

The nature of the normal phase of an ultracold Fermi gas in the BCS-BEC crossover regime is an interesting and unresolved question. As interactions increase, while the many-body ground state remains a condensate of paired fermions, the normal state must evolve from a Fermi liquid to a Bose gas of molecules. In this thesis, I present a technique to spatially select a homogeneous sample from the center of a trapped gas to explore this crossover. Combining this technique with RF spectroscopy, we locally measure Tan's contact as a function of temperature and compare to various many-body theories. In another experiment, we measure the distribution of single-particle energies and momenta for a normal gas across the BCS-BEC crossover. We find that the data fit well to a two-part function that includes a peak corresponding to fermionic quasiparticles and an "incoherent background" that is modeled using the dispersion of thermal molecules. I also describe the construction of a new-generation Fermi gas apparatus.

Dedication

To my parents.

Acknowledgements

My PhD would not have been possible without the support of so many people. I am grateful to Debbie for giving me an opportunity to work in her lab. I feel very fortunate to have been supervised by one of the most brilliant scientists of our generation. Over the years, I learned to think like a physicist from Debbie. I have greatly missed her ability to clarify seemingly complex ideas, her intuition and insight, and her troubleshooting skills. Losing her at such a young age is a profound loss to our community.

When I started grad school, Tara Drake was patient enough to teach me how to work in an ultracold atomic physics lab. Yoav Sagi joined the following year as a postdoc and made the lab very efficient and productive. I have learned so much physics and programming skills from Yoav. Moreover, I have been able to count on both Tara and Yoav for scientific, career and personal guidance during Debbie's absence.

Building the new apparatus would have been difficult without the help of Roman. His focus on details has made sure that our new apparatus is robust and very reliable. Vandy and Xin joined our lab recently. I am sure that they will do great scientific work with the apparatus. I would also like to thank the undergraduate students Sean Braxton and Josh Giles for assembling countless electronic circuit boards.

I would also like to thank the Jin/Cornell group – especially Steven Moses, Phil Makotyn, Dan Gresh, Matt Grau, Cathy Klauss, Jake Covey and Rob Wild. Steven Moses has been a great friend to hike, ski, drink beer and talk physics with. Thanks to Tianlu Yuan and Jamey Szaley for trekking to Everest Base Camp with me. I would also like to thank other JILAns Bryce Bjork, Yuval

Shagam, Gil Porat, Rohan Singh, Bo Yan, Tim Langen, Martin and Vanessa Gaertner, Amodsen Chotia, and Adam Reed for their friendship.

I would like to thank JILA machine shop staff for designing so many parts for the new apparatus. I could even count on Hans Green's help at midnight on the vacuum chamber assembly day. Thanks to James Fung-a-Fat for teaching me how to design and troubleshoot analog electronics and feedback servos. I appreciate Krista Beck for all of her administrative work and helping me with my paperwork.

Last, but not the least, I would also like to thank Eric Cornell, Jun Ye and Cindy Regal for supervising me during the difficult times of Debbie's absence and helping me finish my PhD.

Contents

Chapter

Tables

Table

Figures

Figure

Chapter 1

Introduction

Strongly correlated systems are found in different forms and sizes. High T_c superconductors, superfluid ^{3}He, quark-gluon plasma, neutron stars are all examples of strongly correlated quantum systems [12]. Compared to other strongly interacting systems, ultracold Fermi gases are a little different in the sense that the interaction strength in these systems can be tuned easily from weak to strong in a table-top experiment setting.

Since the advent of laser cooling and the production of the first BEC, interest in quantum gases has increased significantly [13]. Clean systems, controllable dimensality, and tunable interactions make quantum gases quite attractive to study many-body physics [14]. BECs or degenerate Fermi gases of 13 atomic species have been created and hundreds of groups are studying them around the world. In 1999, the fermionic isotope of potassium was cooled to degeneracy by our group [15]. Then, in early 2000s, using Feshbach resonance, these atoms were paired up either as Cooper pairs such as in superconductors or as dimers, to form a fermionic superfluid. That opened an even more new, interesting, and challenging opportunity that is to study strongly-interacting fermions [16]. These superfluids are unique because the critical temperature for the superfluid transition is quite high (compared to T_F). Table 1.1 below lists a comparison between the density and superfluid transition temperature T_c of ultracold Fermi gases and other Fermi systems [17].

Table 1.1: Density and superfluid transition temperature of various Fermi superfluids

System	Density(cm^{-3})	T_c(K)	T_c/T_F
Conventional superconductors	10^{23}	$1-10$	10^{-5}
High T_c superconductors	10^{23}	~ 70	10^{-2}
^{3}He	10^{22}	3×10^{-3}	10^{-3}
Ultracold Fermi gas of ^{40}K atoms	10^{13}	10^{-7}	0.17

1.1 Basic scattering theory and Feshbach resonance

In a simple two-body picture, the collision process between two atoms can be reduced to the solution of the Schrodinger equation of the relative motion [18, 19, 20]. For low energy scattering, when an incoming wave of the form e^{ikz} scatters off of a potential of size r_0, the outgoing wave has the form,

$$\psi(r) = e^{ikz} + f(k)\frac{e^{ikr}}{r}, \tag{1.1}$$

where $f(k)$ is the scattering amplitude. For the case of low k, $f(k)$ can be expanded as,

$$f(k) = \frac{1}{-k\cot\delta_0(k) + ik} \tag{1.2}$$

$$= \frac{1}{a^{-1} - r_0k^2/2 + ik}, \tag{1.3}$$

where a is the s-wave scattering length which is related to the phase shift $\delta_0(k)$. For positive scattering lengths, there exists a bound state with binding energy,

$$\epsilon_b = \frac{\hbar^2}{2ma^2} \tag{1.4}$$

When the energy associated with the two atoms in one channel (open channel) equals with the energy of a bound molecular state in a different channel (closed channel), a scattering resonance known as the Feshbach resonance occurs. If the magnetic moments of atoms in the two channels are different, we can change the energy difference between the two states by tuning the magnetic field. The scattering length tuned by that process around the resonance is given by [18],

$$a = a_{bg}\left(1 - \frac{\Delta}{B - B_0}\right). \tag{1.5}$$

Here, B_0 is the position of the resonance, a_{bg} is the background scattering length, and Δ is the width from the resonance position to the field where the scattering length is zero.

1.2 The phase diagram of an ultracold Fermi gas

The physics described by the phase diagram in Figure 1.1 is known as the BCS-BEC crossover [1]. The crossover is a powerful idea connecting two physicals theories into one first experimentally show in a degenerate Fermi gas [16, 13]. The x-axis is the interaction strength described by the dimensionless quantity $1/k_F a$, where $k_F = (3\pi^2 n)^{1/3}$ is the Fermi momentum of the gas, and n is the total density of the gas. At resonance, when $1/k_F a = 0$, the gas is said to be at unitarity. Since the scattering length diverges, the only relevant length parameter that describes the gas is the density. The y-axis in the diagram is the temperature parameterized by the Fermi temperature T_F. The gas below the critical temperature (T_c) is in the superfluid phase. Depending on the side of the resonance, the superfluid can either be like correlated electrons as described by BCS theory of superconductivity or a Bose Einstein Condensate of K_2 dimers (Figure 1.2). The normal phase is a bit more interesting to explore as various theories do not agree with each other. The normal phase atoms on the BCS side of the resonance behave like quasiparticles described by the Fermi liquid theory. As the interaction is increased, they pair up and form uncondensed dimers on the BEC side of the resonance. However, the behavior of the gas near the resonance is controversial among the community [21, 8]. Some theorists propose a phase similar to pseudogap phase in high T_c superconductors involving many-body pairing of atoms above the critical temperature. The pairing mechanism is many-body as it requires Fermi surface as in Cooper pairing as opposed to two-body dimer pairs. However, other theorists reject this notion of pseudogap physics for a unitary Fermi gas and claim this phase can be described Fermi liquid theory. During my PhD research, we have explored this regime of the strongly interacting Fermi gas using RF spectroscopy to better understand the normal phase behavior of the gas.

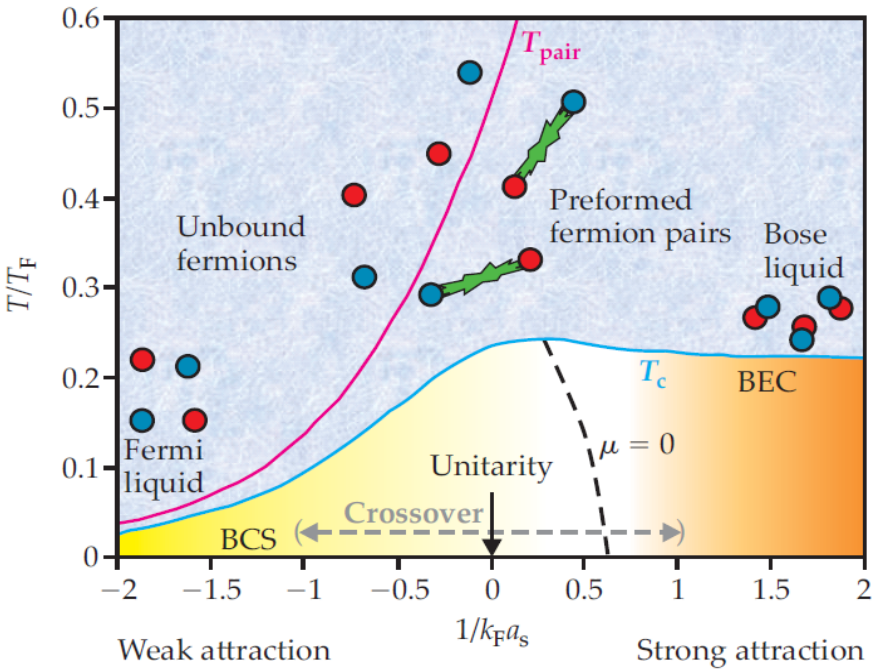

Figure 1.1: Phase diagram of the ultracold Fermi gas. See text for explanation. This figure is reproduced from Ref. [1].

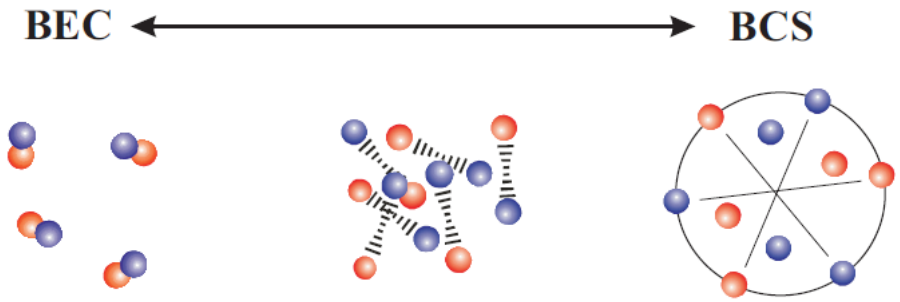

Figure 1.2: BCS-BEC Crossover. On one side of the resonance, the atoms are correlated in momentum near the Fermi surface to form a superfluid as in Cooper pairs in BCS superconductors. On the other side of the resonance, dimers of two atoms are condensed as in BEC of bosonic atoms.

1.3 Homogeneous Fermi gases

For a trapped gas of atoms in a harmonic potential, even though the atoms are in thermal equilibrium, the Fermi temperature is different at different part of the trap due to density variation. Any physical quantity of interest which depends on the scaled temperature, $Q(T/T_F)$, will also vary across the gas. A global measurement of that quantity will yield [22]

$$\bar{Q} = N^{-1} \int Q[T/T_F(\mathbf{r})] n(r) d^3r \tag{1.6}$$

where n(r) is the density distribution and N is the total number of atoms. In general, it can be difficult to interpret the measured quantity $\bar{Q}$. Furthermore, if Q has any sharp features as a function of T/T_F or $1/k_F a$, it can be washed out for $\bar{Q}$.

One example of this is the Fermi surface for a weakly interacting ultracold Fermi gas. It is well known that a Fermi gas at $T = 0$ has a step in momentum (or energy) states called the Fermi surface. At a finite temperature, this step is smoothed out and the width of the sharpness depends on T/T_F, where T_F is the Fermi temperature which depends on density. However, the momentum distribution for a harmonically trapped Fermi gas does not show sharp features(Figure 1.3). Although the center of the cloud is at ultracold temperatures, the outskirts of the cloud are effectively at higher temperature, which means the corresponding Fermi surface is broader. When averaged together, the resulting momentum distribution does not show a sharp feature.

To overcome the issue of density inhomogeneity, some groups have implemented "box" traps of repulsive optical potential to create a homogeneous Fermi gas [23]. In the work described in my thesis, we developed a method based on optical pumping to spatially select the almost homogeneous center of the harmonically trapped gas. You can read more about this technique and the experiments in Tara Drake's thesis [24].

1.4 Thesis outline

In this thesis, I start by explaining the technique we use to spatially select the harmonically trapped atoms and probe the homogeneous sample from the sample of the trap, also colloquially

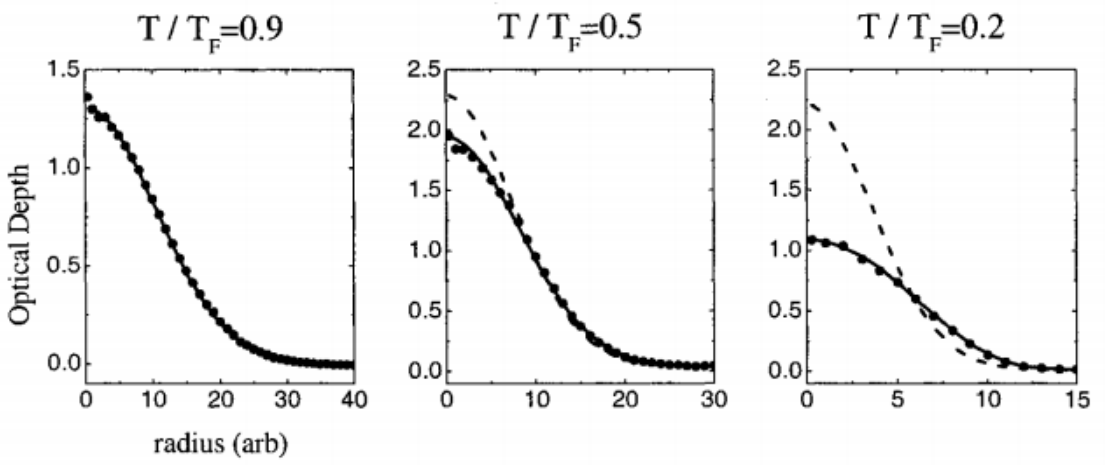

Figure 1.3: Momentum distribution of a harmonically trapped Fermi gas. Even as we lower the temperature of the gas, we do not see a sharp Fermi surface as expected for an ultracold Fermi gas due to density inhomogeneity. The figure is reproduced from [2].

known as the "donut beam technique". In Chapter 2, I will explain the method we use to create the Laguerre-Gaussian beam needed for this technique. I will also describe the proof-of-principle experiment we performed to observe the sharp Fermi surface for the first time in ultracold Fermi gases.

In Chapter 3, I will describe the two experiments we performed that combined RF spectroscopy with the donut beam technique. In one experiment, we measured Tan's contact at unitarity for a homogeneous Fermi gas as a function of temperature. We compared our measurement with various many-body theories. This measurement provides a good benchmark for improving various theoretical tools. We followed this work with the measurement of spectral function of the normal phase of the strongly interacting Fermi gas across BCS-BEC crossover. We also analyzed the data with a two-part function intuitively comparing BCS and BEC physics and extracted quantities like quasi-particle residue, effective mass, Hartree energy shifts, and chemical potential.

In Chapter 4 and 5, I will describe the construction of the new Fermi gas apparatus. I will end the thesis with an outlook of experiments that can be done with interacting Fermi systems. Since the fall of 2016, the Fermi gas apparatus that I built during my PhD has been converted to a strongly interacting BEC apparatus.

Chapter 2

Donut Beam technique to probe a homogeneous Fermi gas

Ultracold quantum gas experiments are usually performed in a harmonic trapping potential. For magnetic traps such as the QUIC trap and Ioffe-Pritchard trap, the potential near the bottom of the trap is harmonic. Similarly, an optical potential created by a Gaussian laser beam is harmonic near the bottom of the trap. Such systems have allowed the ultracold community to perform many important measurements and qualitative observations over the last two decades [13, 25]. However, due to the inherent density inhomogeneity of the trapped gas, time-of-flight measurements are trap averaged. Quantitative analysis on such data can sometimes be quite challenging or sometimes even misleading. Some groups recently have developed "box" traps formed by repulsive optical potentials to create homogeneous gases [26, 23]. We used a different route to tackle this problem. Our method relies on optical pumping of the trapped gas using a hollow beam. In this chapter, I will describe the technique we recently developed to probe the atoms only from the center of the harmonic trap where the density is homogeneous. We apply this technique to a weakly interacting Fermi gas to directly observe the Fermi surface in an ultracold atomic gas for the first time. Much of the content of this chapter is publish in Ref [27].

2.1 Creating a donut beam

A donut beam has a Laguerre-Gaussian (LG) mode. An LG mode for a radial index p (positive integer) and an azimuthal index l (integer) is given by Ref [28] as

$$E_p^l(r,\phi,z) = (-1)^p \left(\frac{r\sqrt{2}}{w}\right) L_p^l \left(\frac{2r^2}{w^2}\right) E^{ikr^2 z/2(z_r^2+z^2)} e^{-r^2/w^2} e^{-i(2p+l+1)\tan^{-1}(z/z_r)} e^{-il\phi}) \tag{2.1}$$

where z_r is the Rayleigh range, w is the Gaussian beam waist, $\tan^{-1}(z/z_r)$ is the Guoy phase of the mode and L_p^l is the generalized Laguerre polynomial. For us, only the $p = 0$ mode is relevant. The cross-section of such beam is a single ring and the intensity is

$$I(r) = \frac{2P}{\pi w^2 l!} \left(\frac{2r^2}{w^2}\right)^l e^{-2r^2/w^2}. \tag{2.2}$$

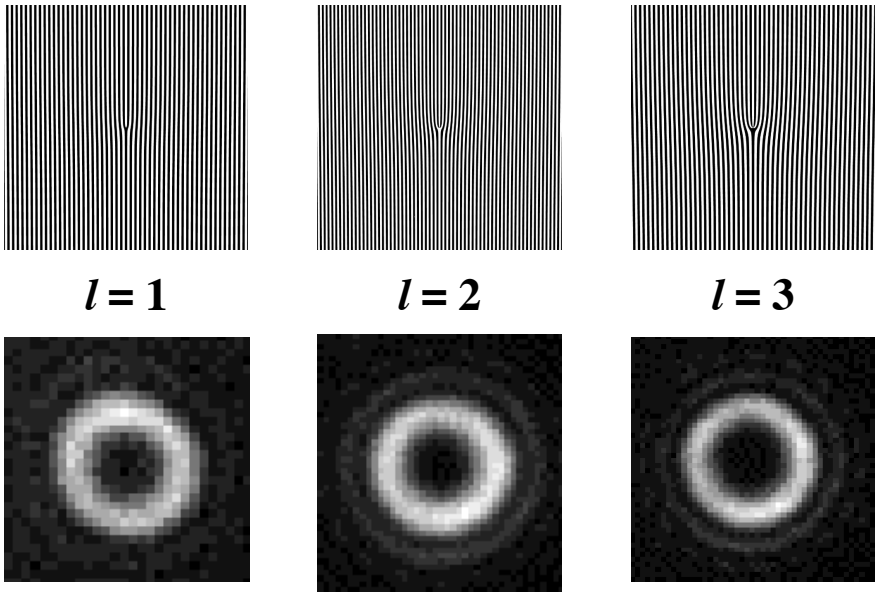

Figure 2.1: Diffraction grating patterns we use to produce Laguerre-Gaussian beam (top) and the corresponding measured cross-section of the intensity profile at the far field (bottom).

These modes can be created in an expensive way by using a Spatial Light Modulator or in a cheaper way by using a holographic plate. In our case, we use an absorptive diffraction grating to realize LG beams. The pattern shown in Figure 2.1 is printed on a glass slide with chromium. The

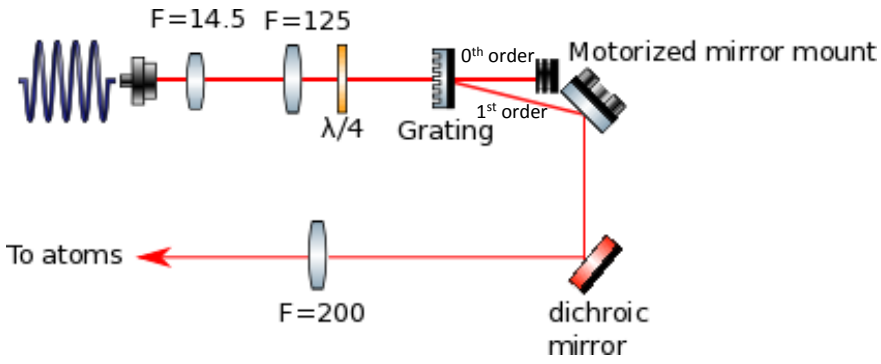

Figure 2.2: Setup to create a Laguerre-Gaussian beam. The beam is focused onto the atom cloud after the last lens.

three patterns correspond to the angular index $l = 1$, 2 and 3. To create LG beams, a Gaussian beam is passed through the set of optics shown in Figure 2.2. An LG mode of $l = 2$ is obtained in the far field after going through the focusing lens that focuses the beam at the atom cloud position. We have two such setups to produce beams of waist 18 μm and 150μm in the horizontal and vertical directions respectively.

We primarily use one of the two optical transitions for the donut beam technique. The first transition is $|F = 9/2, m_F = -7/2\rangle \rightarrow |F' = 5/2, m_F = -5/2\rangle$ and the second one is $|F = 9/2, m_F = -5/2\rangle \rightarrow |F' = 5/2, m_F = -3/2\rangle$. Both of these transitions optically pump the atoms into the $F = 7/2$ hyperfine levels, which are invisible to the probe beam. Thus, only the atoms that not pumped and are at the center of the cloud are imaged after a TOF. Atoms in the excited state decay by spontaneous emission with a branching ratio of 0.955 to the $|7/2, -7/2\rangle$ ground state and 0.044 to the original $|9/2, -7/2\rangle$ state.

2.2 Weakly interacting Fermi gas

The homogeneous Fermi gas is a widely used model in quantum many-body physics and is the starting point for theoretical treatment of interacting Fermi systems. The momentum distribution

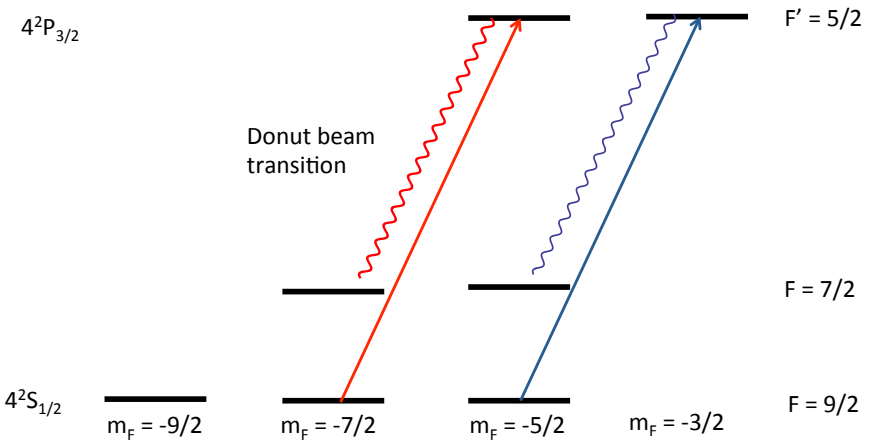

Figure 2.3: Optical pumping transitions for the donut beam. Depending on the experiment, we either use $|F = 9/2, m_F = -7/2\rangle \rightarrow |F' = 5/2, m_F = -5/2\rangle$ or $|F = 9/2, m_F = -5/2\rangle \rightarrow |F' = 5/2, m_F = -3/2\rangle$ transition. Both of these transitions shelve atoms to the upper hyperfine level in the ground state invisible to the probe beam.

for an ideal Fermi gas is given by the Fermi-Dirac distribution:

$$n(k) = \frac{1}{e^{\left(\frac{\hbar^2 k^2}{2m} - \mu\right)/k_B T} + 1}, \tag{2.3}$$

where the $n(k)$ is the average occupation of a state with momentum $\hbar k$, m is the fermion mass, μ is the chemical potential, k_B is Boltzmann's constant, and T is the temperature. Surprisingly, to our knowledge, the momentum distribution of an ideal Fermi gas, with its sharp step at the Fermi momentum, $\hbar k_F$, had not been directly observed in experiments before 2012. For the vast majority of Fermi systems, such as electrons in materials, valence electrons in atoms, and protons and/or neutrons in nuclear matter, one always has an interacting system. A dilute Fermi gas of atoms opens new possibilities with its low density, access to the momentum distribution through time-of-flight imaging, and controllable interparticle interactions. However, these trapped gases have nonuniform density, which has prevented the observation of a sharp step in their momentum distribution and, more generally, can complicate comparisons with theory.

If the change in the trapped gas density is small on the length scale of the relevant physics, one can apply a local density approximation. Measurements can then be compared to theory by integrating the prediction for a homogeneous gas over the density distribution of the trapped gas. While the agreement between experiment and theory can be quite good, characteristic features such as a sharp Fermi surface in k-space can be lost in trap-averaged data. For rf spectroscopy and for thermodynamic measurements, recent work has used *in-situ* imaging of trapped gases combined with knowledge of the trapping potential to yield results that can be directly compared to homogeneous Fermi gas theory [13, 21, 29, 30]. However, this technique cannot probe the momentum distribution, which requires a sudden release of the gas from the trap followed by ballistic expansion and imaging. We developed a method to measure the momentum distribution locally in a trapped Fermi gas and present a direct observation of the Fermi surface in k-space.

2.3 Experimental Sequence

2.3.1 Aligning the beam

We align the donut beam onto the cloud by either looking at the number loss and the peak OD or by looking at the slosh of the cloud in the trap after optical pumping. In the first method, as we scan the position of the donut beam across the cloud we see a "W" shape in number loss corresponding to the shape of the donut beam cross-section (Figure 2.4). At the center, we see that the peak OD of the could same as that without optical pumping. Once the beam is aligned this way, we do a finer scan by optically pumping beam and waiting for a some time before releasing them from the trap Figure 2.5. The slosh of the atoms is minimized for an aligned beam. As the atoms slosh at the trapping frequency this method can be alternatively used to measure the trapping frequency in the most non-perturbative way.

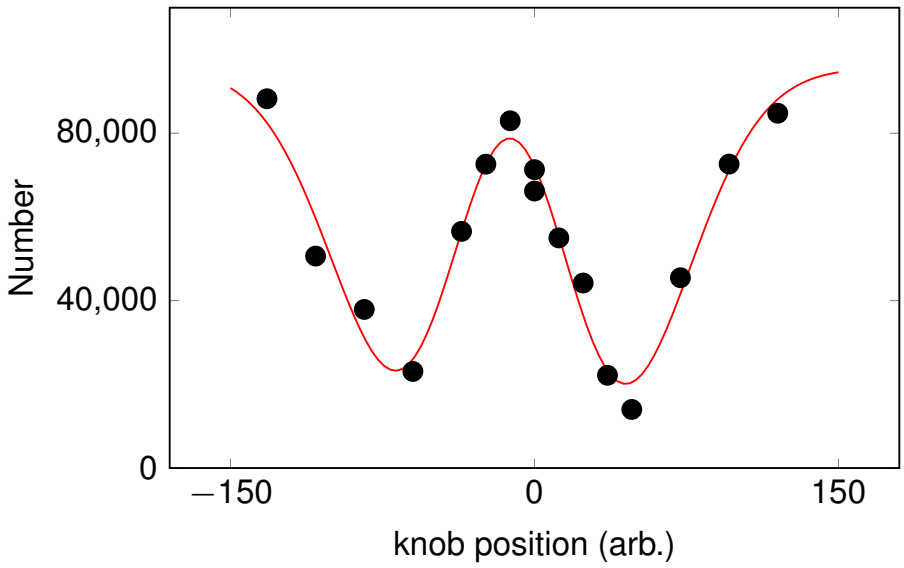

Figure 2.4: Alignment of the donut beam by scanning to position to see a "W" shape in the atom number corresponding to the cross-section of the beam. We scan the motorized mirror shown in Figure 2.2.

We begin with a quantum degenerate gas of $N = 9 \times 10^4$ ^{40}K atoms in an equal mixture of the $|f, m_f\rangle = |9/2, -9/2\rangle$ and $|9/2, -7/2\rangle$ spin states. The atoms are confined in a cylindrically symmetric, crossed-beam optical trap characterized by a radial trap frequency ν_r of 214 Hz and

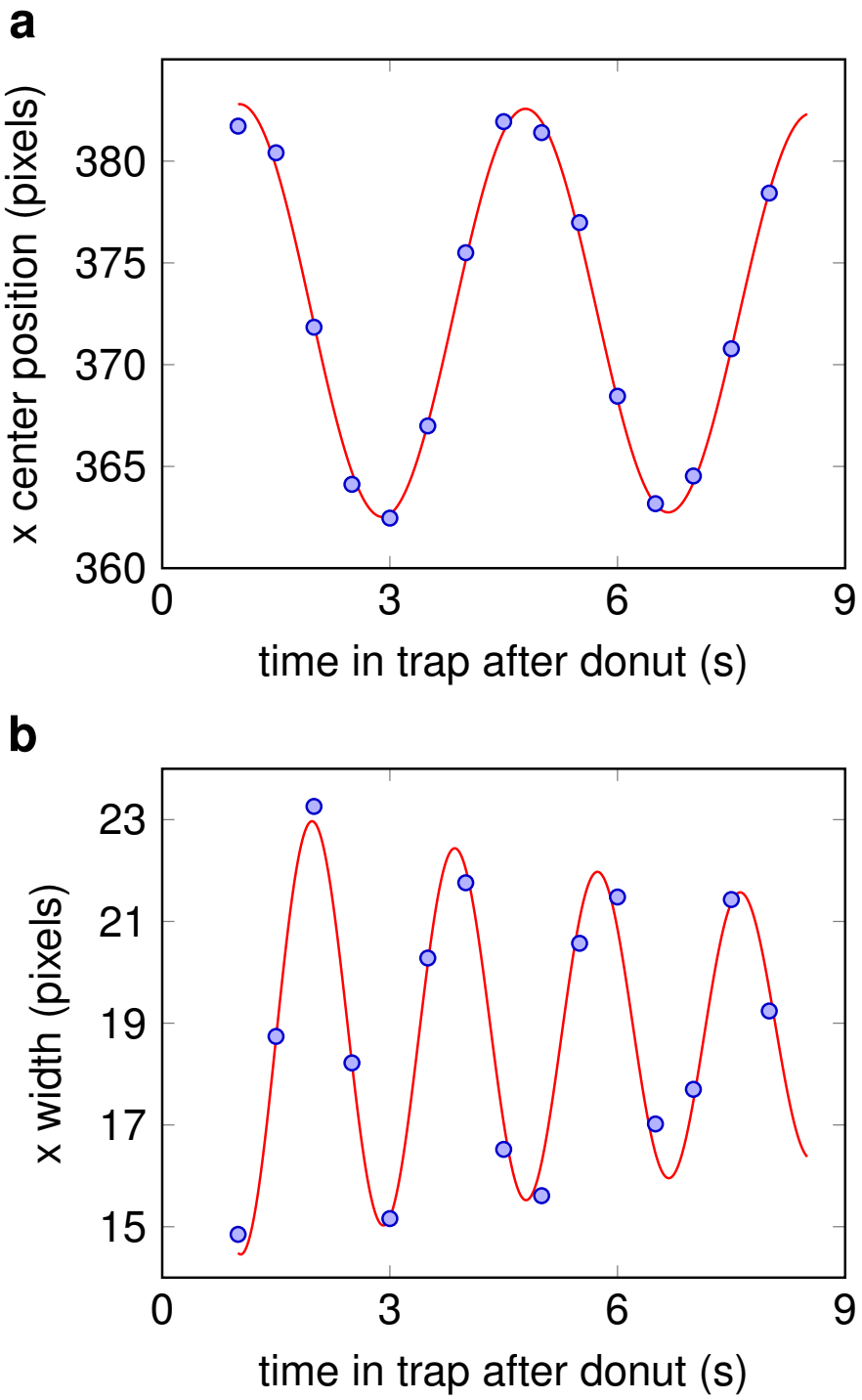

Figure 2.5: Alignment of the donut beam by looking at the slosh and breathe of the cloud at different hold time after a TOF. When the donut beam is aligned to the center of the atom cloud these effects are minimized.

an axial trap frequency ν_z of 16 Hz. To facilitate future application of this technique to probing strongly interacting Fermi gases, we work at a magnetic field that is near a Feshbach resonance between the initial two spin states. We take data at $B = 208.2$ G where the scattering length a between atoms in the $|9/2, -9/2\rangle$ and $|9/2, -7/2\rangle$ states is approximately $-30\ a_0$ [31], where a_0 is the Bohr radius. Here, the gas is very weakly interacting, with a dimensionless interaction strength of $k_F a = 0.011$.

Our measurements probe only the $|9/2, -7/2\rangle$ spin component. We use two intersecting hollow light beams to optically pump atoms into a spin state that is dark to our imaging (see Figure 2.3). The hollow light beams are resonant with the transition from the $|9/2, -7/2\rangle$ state to the electronically excited $|5/2, -5/2\rangle$ state (see Fig. 2.3).

The first beam propagates along the vertical (y) direction, is linearly polarized, and has a waist of 186 μm. Given the elongated shape of the trapped gas, this beam is primarily spatially selective along the long axis (z) of the cloud. The second beam propagates along the axial (z) direction of the cylindrically symmetric trap, parallel to B, and is circularly polarized. This beam has a waist of 16.8 μm and selectively optically pumps atoms based on their location along x and y.

To probe the momentum distribution of the central part of the trapped gas, we first turn off the trap suddenly and illuminate the atoms with the vertical hollow light beam, followed immediately by pulsing on the horizontal beam. The power in the beams in on the order of tens to hundreds of nW and is varied to control the fraction of atoms that are optically pumped out of the $|9/2, -7/2\rangle$ state. Each beam is pulsed on for 10 to 40 μs, with the pulse durations chosen such that the fraction of atoms optically pumped by each of the two beams is roughly equal (within a factor of two). The relative durations of the two pulses are chosen to optimize the relative removal of the beams with respect to the density homogeneity of the remaining cloud and are typically 10 to 40 μs. We have found the optimal homogeneity occurs when the vertical beam alone removes roughly half of the total signal removed; for example, when 66% of our signal is removed, 30% is removed by the vertical beam alone. We then image the remaining atoms in the $|9/2, -7/2\rangle$ state after 10

ms or 12 ms time of flight. The imaging light propagates along the z direction and we apply an inverse Abel transform to the 2D image (assuming spherical symmetry in k-space) to obtain the 3D momentum distribution, $n(k)$.

2.4 Fermi Surface

In Fig. 2.6, we show normalized momentum distributions measured with and without using the hollow light beams. As was first seen in Ref. [15], the trap-averaged momentum distribution for the Fermi gas is only modestly distorted from the Gaussian distribution of a classical gas. The dashed line in the inset to Fig. 2.6 shows a fit to the expected momentum distribution for a harmonically trapped ideal Fermi gas, from which we determine the temperature of the gas to be $T/T_{F,\mathrm{trap}} = 0.12 \pm 0.02$. Here, the Fermi temperature for the trapped gas is given by $T_{F,\mathrm{trap}} = E_{F,\mathrm{trap}}/k_B$, where $E_{F,\mathrm{trap}} = h(\nu_r^2\nu_z)^{1/3}(6N)^{1/3}$ is the Fermi energy for the trapped gas and N is the total number of atoms. After optical pumping with the hollow light beams so that we probe the central 16% of the atoms, the measured momentum distribution (main part of Fig. 2.6) has a clear step, as expected for a homogeneous Fermi gas described by Equation 2.3.

For a sufficiently small density inhomogeneity, the momentum distribution should look like that for a homogeneous gas at some average density. To characterize this, we fit the normalized distributions to the prediction for an ideal homogeneous gas (solid lines). The homogeneous gas distribution is described by its temperature and density. We fix T to that measured for the trapped gas, which leaves only a single fit parameter, k_F, that characterizes the density. The momentum distributions are then plotted as a function of the usual dimensionless momentum, k/k_F. The momentum distribution of the central 16% of the trapped gas fits well to the homogeneous gas result, while the trap-averaged momentum distribution clearly does not.

2.5 How homogeneous is the gas?

In order to quantify how well the measured momentum distribution is described by that of a homogeneous gas, we look at the reduced χ^2 statistic in Fig. 2.7a. The reduced χ^2 is much larger

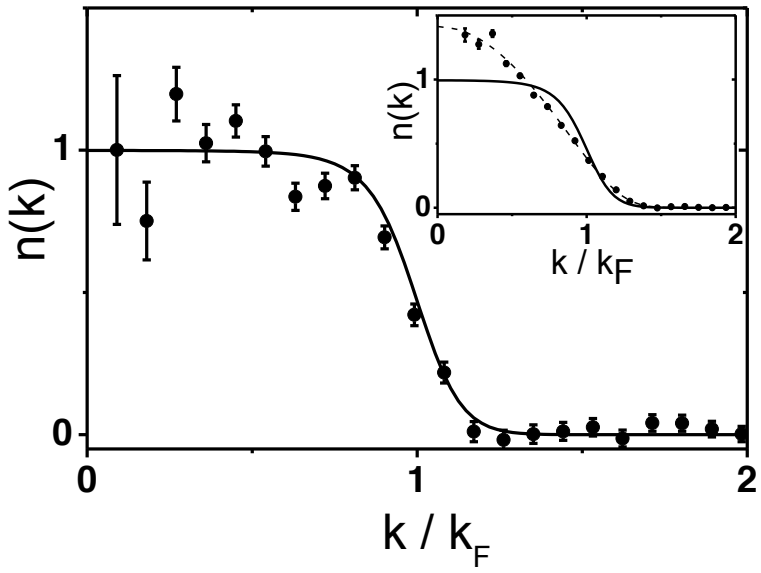

Figure 2.6: Momentum distribution for a weakly interacting Fermi gas after optical pumping with a donut beam. The distribution is an average of 12 images after selecting the central 16% of a harmonically trapped gas. The data is normalized to have the area under the curve to be equal to 1. The solid line is the fit to the Fermi distribution with a fixed T, k_F is the only fit parameter. The inset shows the distribution without optical pumping. The dashed line in the inset shows the expected momentum distribution for a trapped gas with the temperature T.

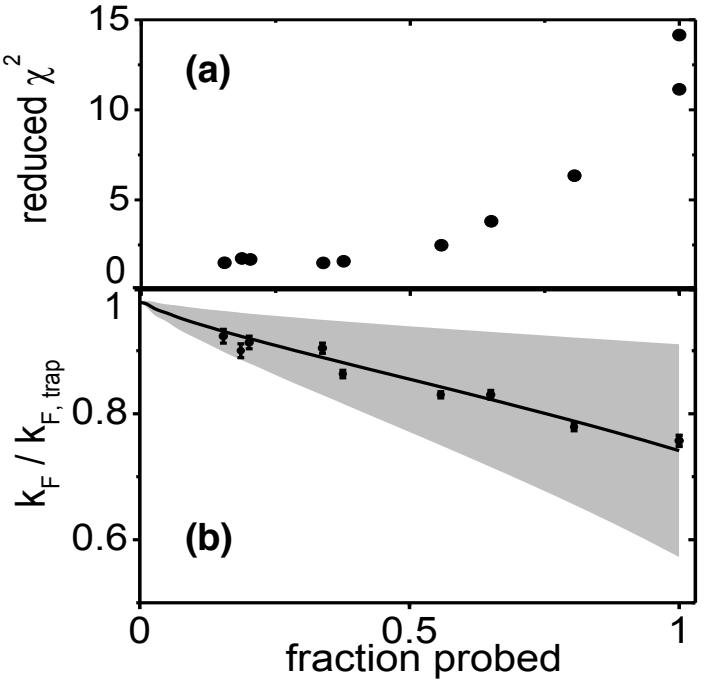

Figure 2.7: We look at reduced the $\chi-$ squared (a) of the fit and the fit parameter k_F (b) as a function of fraction probed. We find that the reduced $\chi-$ squared is lowered as lower fraction of atoms are probed, which means the system is better described as a homogenous gas.

than 1, indicating a poor fit, for the trap-averaged data due the fact that the density inhomogeneity washes out the Fermi surface. As we probe a decreasing fraction of atoms near the center of the trap, χ^2 decreases dramatically and approaches a value of 1.6 for fractions smaller than 40%.

The single fit parameter k_F characterizes the density of the probed gas and should increase as we probe fewer atoms near the center of the trap. Fig. 2.7b displays the fit value k_F, in units of $k_{F,\mathrm{trap}} = \sqrt{2mE_{F,\mathrm{trap}}}/\hbar$. As expected, k_F increases as the fraction of atoms probed decreases. We have developed a model of the spatially selective optical pumping by the hollow light beam, which is discussed below. The model result for the average local k_F, $\langle k_F \rangle$, of the probed gas is shown with the solid line in Fig. 2.7b, and we find that this agrees well with the fit k_F, even when the measured momentum distributions clearly do not look like that of a homogeneous gas. Using the model, we calculate the variance δ^2 of the local k_F, and the shaded region in Fig. 2.7b shows $\langle k_F \rangle \pm \delta$. In the region where the reduced χ^2 indicates that the measured $n(k)$ fits well that for a homogeneous gas (fraction probed $< 40\%$), $\delta / \langle k_F \rangle < 0.08$.

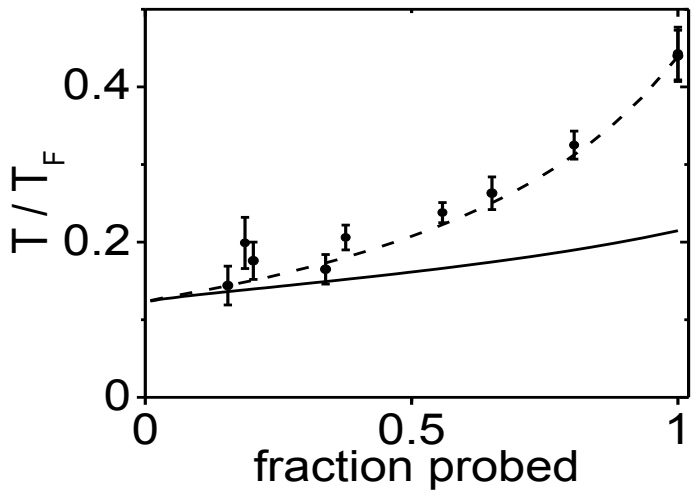

Figure 2.8: Measured T/TF vs the fraction of atoms probed. Here, we fit the measured momentum distribution to a homogeneous gas distribution with two free parameters, T/T_F and k_F. The density inhomogeneity of the probed gas results in T/T_F that is much larger than expected from the calculated average density of the probed gas (solid line). A sharp Fermi surface, characterized by a small fit T/T_F, emerges as the fraction of atoms probed decreases. The dashed line shows the result of fitting to model calculations of the probed momentum distribution, which agrees well with the data.

Instead of fixing T to the value obtained from fitting the trapped gas momentum distribution, we can also look at measuring the temperature by fitting to a homogeneous gas distribution, where both k_F and T/T_F are fit parameters. In this case, a large density inhomogeneity that washes out the Fermi surface will result in an artificially high fit value for T/T_F. This can be seen in Figure 2.8. For comparison to the data, the solid line shows the average $T/\langle T_F \rangle$ for the probed gas calculated using our model. Here, T is fixed and the dependence on the fraction probed comes from the fact that the average density, and therefore the average local T_F, increases as we probe a smaller fraction of atoms that were near the center of the trapped gas. The fit T/T_F approaches the average value from the model as we reduce the fraction of atoms probed, and for $< 40\%$ probed, the two are consistent within our measurement uncertainty. For the smallest fraction probed (data shown in Fig. 2.6), the best fit value is $T/T_F = 0.14 \pm 0.02$. As a check of the model, we can also calculate $n(k)$ for the probed gas and fit this to the homogeneous gas distribution; the results (dashed line in Fig. 2.8) agree well with the data.

2.6 The effect of optical pumping

In modeling the effect of optical pumping with the hollow light beams, we assume that only atoms that do not scatter a photon are probed. The probability to scatter zero photons from each beam is taken to be $P_i = \exp(-\gamma_i \tau_i \sigma)$, where τ_i is the pulse duration and the subscripts $i = 1, 2$ denote the two hollow light beams. The photon flux is given by $\gamma_i = I_i \lambda/(hc)$, where I_i is the position-dependent intensity, c is the speed of light, and $\lambda = 766.7$ nm is the wavelength. For the optical absorption cross section, we use $\sigma = 3\lambda^2 \eta/(2\pi)$, where $\eta = 0.044$ is the branching ratio back to the initial state.

Attenuation of the hollow light beam as it propagates through the atom cloud is observable in the long direction of the cloud (along z), as seen in the inset of Figure 2.9. To include this effect, we consider the two hollow light beam pulses sequentially, and we assume that the number of photons absorbed locally equals the number of optically pumped atoms. Interestingly, the model predicts that the attenuation results in a smaller density variance in the probed gas when compared to a

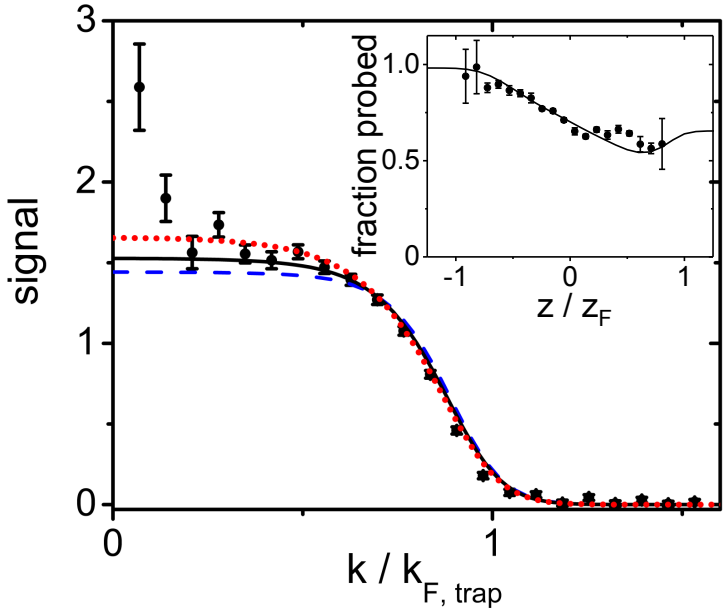

Figure 2.9: Modeling the spatially selective optical pumping. We compare the normalized momentum distribution of the central 38% of the atoms to three different models (dotted, solid, and dashed lines; see text). The data (circles) are obtained from an average of four images. We find that the attenuation of the hollow light beams (inset) does not strongly affect the predicted final momentum distribution when probing a small fraction of the gas. (Inset) We take images of the cloud after a short (1.3 ms) expansion and compare data with the horizontal hollow light beam and without any optical pumping in order to measure the fraction of atoms probed (circles) vs z/z_F , where $z_F = \sqrt{\frac{2E_{F,\mathrm{trap}}}{m(2\pi\nu_z)^2}}$. For this data, the fraction probed is 71%. The prediction of our model (solid line), which includes attenuation of the hollow light beam as it propagates through the cloud, agrees well with the data.

model that ignores attenuation but where we adjust the beam powers to probe the same fraction of the atoms. This effect is relatively small and decreases as one probes a smaller fraction of the gas. This can be seen in Figure 2.9 where we show the measured momentum distribution for the central 38% of the atoms compared to three different models, each of which is adjusted to give the same probed fraction. The solid line is the model explained above, which includes attenuation, while the dotted line show the result when we ignore the depletion of the hollow light beams. For comparison, the dashed line shows the expected distribution if one selects atoms in a cylindrical volume with sharp boundaries.

2.7 Conclusion

In conclusion, we have directly observed the Fermi surface in the momentum distribution of a weakly interacting Fermi gas. To do this, we probe the central region of a harmonically trapped gas. A concern with this approach is that one might be left with very little signal after selecting a small enough region to approximate a homogeneous gas. However, for a gas at $T/T_{F,\mathrm{trap}} = 0.12$ and our typical measurement precision, we find that probing the central 40% (or less) of the gas is sufficient to approximate a homogeneous gas. In the next chapter, I will discuss combining this donut beam technique with RF spectroscopy to measure Tan's contact and the spectral function for a strongly interacting Fermi gas.

Chapter 3

Probing a homogeneous strongly interacting Fermi gas

The collective behavior of an ensemble of strongly interacting fermions is central to many physical systems including liquid ^{3}He, high-T_c superconductors, quark-gluon plasma, neutron stars, and ultracold Fermi gases. However, theoretical understanding of strongly interacting fermions is challenging due to the many-body nature of the problem and the fact that there is no obvious small parameter for a perturbative analysis. Therefore, in order to establish the validity and applicability of theoretical approaches, it is essential to compare them against experimental results. Ultracold atomic Fermi gases are ideal for this purpose, as they provide excellent controllability, reproducibility, and unique detection methods [16, 13]. In particular, changing the magnetic field in the vicinity of a Feshbach resonance enables precise control of the interactions, which are characterized by the s-wave scattering length [18]. On resonance, the scattering length diverges and the behavior of the unitary gas no longer depends on it. Testing theories in this regime is especially desirable.

An outstanding issue for the unitary Fermi gas is the nature of the normal state just above the transition temperature, T_c, for a superfluid of paired fermions. Some theories of strongly interacting Fermi gases (BCS-BEC crossover theories) predict that the normal state is not the ubiquitous Fermi liquid but instead involves incoherent fermion pairing (preformed pairs) in what has been termed the pseudogap state [32]. It has been suggested that the pseudogap state affects the temperature dependence of a quantity called Tan's contact [6]. The contact, which is a measure of the short-range correlation function, has been shown to be an essential thermodynamic parameter for ensembles with short-range interactions [33, 34, 35, 36, 37, 9]. The contact connects many seemingly

unrelated quantities through a set of universal relations that are valid for any temperature, any interaction strength, and any phase of the system. While the value of the contact, as well as many of these relations, were tested successfully at low temperature [38, 39, 40, 41], there are significant discrepancies among theories on how the contact of a unitary homogeneous Fermi gas depends on temperature, especially around T_c [42, 6, 43, 5, 7]. The temperature dependence of the contact was recently measured for a trapped unitary Fermi gas [44]. However, for the trapped gas, averaging over the inhomogeneous density distribution washes out any temperature-dependent features, and the measurement was unable to differentiate between theoretical models. Here we present a measurement of the homogeneous contact, which can be directly compared to the predictions of different many-body theories.

The behavior of strongly interacting quantum gases can be probed in many different ways. In the early days, the momentum distribution after a time-of-flight was measured after ramping into the molecular side of the resonance to either measure the molecular fraction or the condensate fraction [45]. In-situ images provide information on density distribution, which can be used to calculate the pressure of the gas, and thus the thermodynamics of the gas can be studied [21, 30]. Time-of-flight information can be used to study the energy, hydrodynamic and collective behavior of the gas. Bragg spectroscopy [44] and Raman spectroscopy [46] have also allowed to learn the structure factor and the dispersions in the Fermi gas. One other technique to study the strongly interacting Fermi gas is RF spectroscopy [16, 47, 38]. The RF spectroscopy technique allows us to study quantities such as the contact and spectral function of the gas.

In this chapter, I will describe the basics of RF spectroscopy. Then I will describe our measurement of homogeneous contact as a function of temperature at unitarity using this technique. I will then describe another experiment where we performed a momentum resolved RF spectroscopy of strongly interacting Fermi gas across BCS-BEC crossover to measure the spectral function. Most of the content in this chapter was published in Ref. [48] and Ref. [49].

3.1 Tan's Contact

Tan's contact is the measure of the short-range two-body correlation in an interacting quantum gas. In 2008, Shina Tan derived a number of universal relations for an interacting Fermi gas with short-range, or contact, interactions [33, 34, 35, 36, 37, 9]. These universals relations connect microscopic quantities, such as the momentum distribution of the fermions, to macroscopic quantities, such as the total energy of the system. These relations are quite powerful because they are applicable whether the system is many-body and few-body, whether the gas is normal or superfluid and whether the system is homogeneous or trapped.

One of the most intuitive ways to understand the contact is by looking at the gas microscopically [36, 9]. Let's consider a Fermi gas atoms of atoms with spin-up and spin-down, and with s-wave scattering length a between the two spin states, and with $a \gg r_0$, the physical range of interactions. We would like to count the number spin-up and spin-down atoms inside a volume $V = \frac{4}{3}\pi l^3$ with center at the location of spin-up atom. Naively, one would expect the number of pairs in this volume to be $n_\uparrow \times n_\downarrow \times (\frac{4}{3}\pi l^3)^2$, where $n_{\uparrow(\downarrow)}$ is the density of spin-up(down) atoms. For short-range pairs with $l \ll n^{1/3}$, where n is the total density, the number of pairs scales as l^4 instead of l^6 and this enhancement factor corresponds to the Contact.

$$N_{pair} \to \frac{l^4}{4} C \tag{3.1}$$

Because contact measures the short-range correlations, because of the nature of the wavefunction, it appears as the amplitude of the k^4 tail in momentum distribution [34]. That is,

$$C = \lim_{k\to\infty} k^4 n(k), \tag{3.2}$$

where k is the momentum in units of Fermi momentum, $k_F = \frac{\sqrt{2mE}}{\hbar}$, and $n(k)$ is normalized such that $\frac{1}{(2\pi)^3}\int_0^\infty n(k) d^3k = 0.5$.

Another relations that was later derived comes from the high-frequency tail of RF spectroscopy. The high frequency tail of the rf line shape is predicted to scale as $\nu^{-3/2}$, with the

contact connecting the amplitude of the high frequency tail through (see Ref. [9] and references therein):

$$\frac{\Gamma(\nu)}{\int_{-\infty}^{\infty}\Gamma(\nu')\mathrm{d}\nu'} = \frac{C/(Nk_F)}{\sqrt{2}\pi^2\nu^{3/2}} \quad \text{for} \quad (\mathrm{E_F/h}) \ll \nu \ll \frac{\mathrm{h}}{2\mathrm{mr}_0^2} \tag{3.3}$$

where N is the total number of atoms, and $\hbar k_F$ is the Fermi momentum, and ν is the rf detuning in units of the Fermi energy, E_F/h, with h being the Planck constant ($2\pi\hbar \equiv h$).

3.1.1 RF Spectroscopy

RF spectroscopy relies on the manipulation of Zeeman states of the atoms. Around the field near Feshbach resonance, i.e. 202 G, $m_F = -9/2$, $m_F = -7/2$ and $m_F = -5/2$ are separated by about 45 MHz in energy. Hence, we can use RF photons to increase or decrease m_F by one.

RF spectroscopy can be understood using a semi-classical picture of light atom interaction [50]. Let the energy difference between the two spin states $|e\rangle$ and $|g\rangle$ be $\hbar\omega$, $E_e - E_g = \hbar\omega_0$. The electric field of the RF can be written as $E(t) = E_0\cos(\omega_L t)$, where E_0 is the strength of the field and ω_L is the frequency of the RF. The Hamiltonian for this system is $H = H_{atom} + V_{int}$, where

$$H_{atom} = \begin{pmatrix} 0 & 0 \\ 0 & \hbar\omega_0 \end{pmatrix}, V_{int} = \begin{pmatrix} 0 & dE \\ dE & 0 \end{pmatrix}.$$

Here, $d = \langle e|\hat{\pi}\cdot\vec{r}|g\rangle$ is the dipole matrix element. We can use the time-dependent Schrodinger equation to find the population of excited states,

$$i\hbar\frac{\partial\psi}{\partial t} = H\psi. \tag{3.4}$$

The wave function ψ can be written as , $\psi = c_1(t)|g\rangle + c_2(t)|e\rangle e^{i\omega_0 t}$, where c_1 and c_2 are probability amplitude such that $c_1^2 + c_2^2 = 1$. Using RWA approximation,

$$i\frac{d}{dt}\begin{pmatrix} c_1 \\ c_2 \end{pmatrix} = \begin{pmatrix} 0 & \Omega e^{i\delta t} \\ \Omega e^{-i\delta t} & 0 \end{pmatrix}\begin{pmatrix} c_1 \\ c_2 \end{pmatrix}. \tag{3.5}$$

Here, $\Omega = dE_0/\hbar$ is the Rabi frequency and $\delta = \omega_L - \omega_0$ is the RF detuning. We can solve this coupled differential equation with an initial condition of $c_1(0) = 1$ and $c_2(0) = 0$, to get the

population in the excited state as a function of time,

$$|c_2(t)|^2 = \frac{\Omega}{\Omega^2 + \delta^2/4} \sin^2(\sqrt{\Omega^2 + \delta^2/4}t). \tag{3.6}$$

When atoms in $m_F = -9/2$ and $m_F = -7/2$ are strongly interacting, using RF photons to move the atoms from $m_F = -7/2$ to $m_F = -5/2$ is especially useful because the atoms in $m_F = 5/2$ are weakly interacting with the other two spin states. Hence, the information we get by scanning the frequency of RF and counting the number of atoms out coupled is easy to interpret.

3.1.2 Experimental Sequence

We perform the experiments with an optically trapped ultracold gas of ^{40}K atoms in an equal mixture of the $|F, m_F\rangle = |9/2, -9/2\rangle$ and $|9/2, -7/2\rangle$ spin states. We determine the contact by combining rf spectroscopy with the donut beam technique to probe the local properties of a trapped gas as described in Chapter 2. The experimental sequence is depicted in Figure 3.1. The magnetic field is ramped adiabatically to the Feshbach resonance and kept at this value for 2 ms before abruptly shutting off the trapping potential. Before the potential is shut off, the hollow beams are pulsed on, followed by the rf pulse, which transfers a small fraction of the atoms in the occupied $|9/2, -7/2\rangle$ state to the initially unoccupied $|9/2, -5/2\rangle$ state (which is weakly interacting with the other two spin states). We detect these atoms using absorption imaging after 3 ms of expansion. The temperature of the gas is varied by changing the final depth of the optical dipole trap in the evaporation process [31]. The number of atoms per spin state after the evaporation ranges from $50,000$ to $220,000$. For the data presented, the radial trapping frequency, ω_r, ranges from $2\pi \times 200$ Hz to $2\pi \times 410$ Hz, while the axial trapping frequency, ω_z, ranges from $2\pi \times 19$ Hz to $2\pi \times 25$ Hz.

The contact is extracted from a measurement of the rf line shape $\Gamma(\nu)$ [38], where $\Gamma(\nu)$ is the rate of atoms transferred from one of the two interacting spin states to a third state, by an rf pulse centered at a frequency detuning ν. A representative data set, where the hollow light beams were used to select the central 30% of the atom cloud, is shown in figure 3.2. For each line shape, we take data at 30 different detunings between -16 kHz and $+116$ kHz, where $\nu = 0$ is defined as

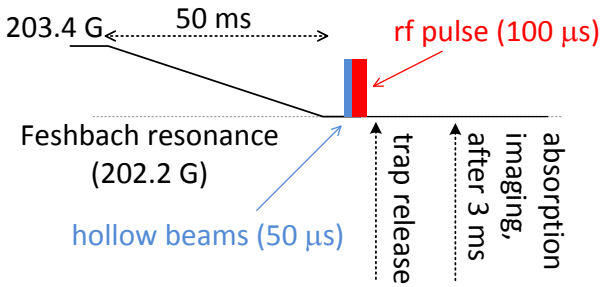

Figure 3.1: Time sequence of the experiment. The magnetic field is ramped from 203.4 G, where the atoms are initially prepared, to the Feshbach resonance. The hollow light beams are turned on 280 μs before trap release; initially, the beam that propagates perpendicular to the long axis of the cloud is pulsed on for 10 μs followed by 40 μs of the second beam. The line shape is measured using an rf pulse with a total duration of 100 μs and a gaussian field envelope with $\sigma = 17\,\mu s$, centered 180 μs before trap release. The cloud expands for 3 ms before being detected by absorption imaging. To improve the signal-to-noise ratio, we remove the remaining atoms from the $|9/2, -9/2\rangle$ and $|9/2, -7/2\rangle$ states and then transfer the outcoupled atoms in the $|9/2, -5/2\rangle$ state to the $|9/2, -9/2\rangle$ state, where we image on the cycling transition [3].

the single-particle transition frequency between the $|9/2, -7/2\rangle$ and $|9/2, -5/2\rangle$ states (measured for a spin polarized gas in the $|9/2, -7/2\rangle$ state).

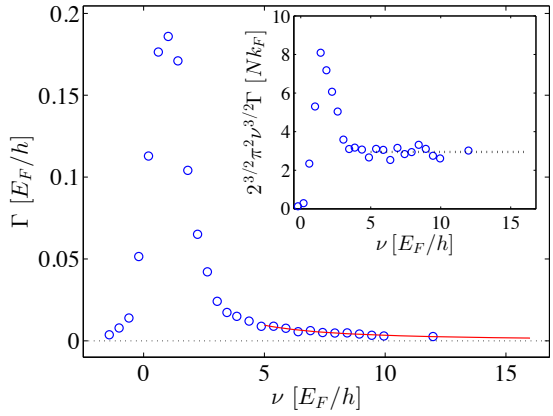

Figure 3.2: An rf line shape for the unitary Fermi gas at $T/T_F = 0.25$ with 30% of the atoms probed. The solid (red) line is a fit to Eq.(3.3) with the normalization $\int_{-\infty}^{\infty} \Gamma(\nu) \mathrm{d}\nu = 0.5$, due to the $50\% - 50\%$ spin mixture. The inset shows the same data multiplied by $2^{3/2}\pi^2\nu^{3/2}$. We make sure the rf pulse induces only a small perturbation, by setting its power to well below the value where we see the onset of saturation of the number of outcoupled atoms. The measurement at different frequencies is done with different rf powers, and when analyzing the data, we linearly scale the measured number of atoms outcoupled at each frequency to correspond to a common rf power.

The inset of Figure 3.2 shows $\Gamma(\nu)$ multiplied by $2^{3/2}\pi^2\nu^{3/2}$, where we observe a plateau for frequencies higher than $5\,E_F/h$. We extract the contact by fitting the measured $\Gamma(\nu)$ for $\nu > 5\,E_F/h$ to Eq.(3.3) (solid line in figure 3.2). For the normalization, we integrate the line shape, including the tail, up to $\nu = \hbar/mr_{\mathrm{eff}}^2$, where r_{eff} is the effective range of the interaction [18] (which is approximately $300E_F/\hbar$).

3.1.3 Contact versus Temperature

The main result of this experiment, namely the homogeneous contact versus the temperature, is presented in figure 3.3. The contact is normalized to the average k_F of the probed sample, and temperature is given in terms of T/T_F, with T_F being the average Fermi temperature of the probed sample. The data show a monotonic decrease of the contact with increasing temperature from

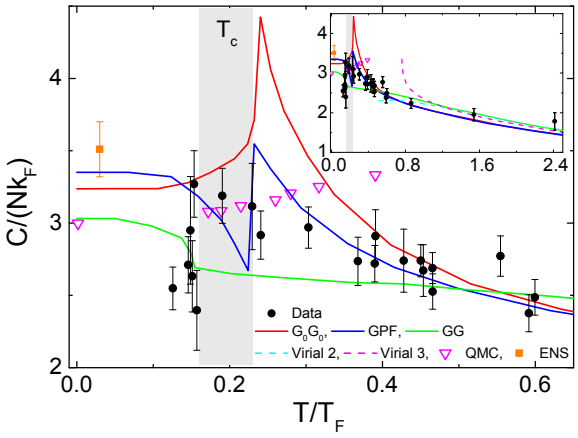

Figure 3.3: The contact of a nearly homogeneous sample (about 30% of the trapped atoms probed), versus T/T_F at unitarity (black circles). The shaded area marks the superfluid phase transition, with some uncertainty in its exact position ($T_c/T_F = 0.16 - 0.23$) [4]. As a comparison, we plot the gaussian pair-fluctuation NSR model (GPF) [5], the self-consistent t-matrix model (GG) [4], the non-self-consistent t-matrix model (G_0G_0) [6], the 2nd and 3rd order virial expansion [5], a quantum Monte-Carlo calculation (QMC) [7], and the contact extracted from a thermodynamic measurement done at ENS [8]. The error bars represent one standard deviation. The inset shows the high temperature behavior of the contact, where we find good agreement with the virial expansion.

a maximum value of 3.3 Nk_F. For $T/T_F = 0.16$, at the edge of our experimentally attainable temperatures, we observe a sharp decrease of the contact to about 2.6 Nk_F. We compare our data with several theoretical models [5] and a quantum Monte-Carlo (QMC) simulation [7]. The many-body theories are in the framework of the t-matrix approximation [5], differing by their choice of the diagrammatic expansion, the particle-particle propagator, and the self-energy. For $T/T_F > 0.4$, the differences between the theoretical models are small, and the predictions all lie within the uncertainty of the data. As expected, at higher temperatures ($T/T_F > 1$), we find good agreement with the virial expansions [5] (see inset of figure 3.3). For $T/T_F < 0.4$, our data do not agree fully with any of the many-body theories. It is worth noting, however, that two of the theories (GPF and G_0G_0) predict a higher value for the contact above the superfluid phase transition than below, which may be consistent with observed sharp decrease near $T/T_F = 0.16$. We note that the predicted T_c/T_F has some uncertainty, as indicated by the shaded region in figure 3.3. The non-self-consistent t-matrix model (G_0G_0) predicts an enhancement of about 50% in the value of the contact around T_c [6], which the data do not show. We also do not observe an increasing trend in the contact for $T > T_c$, in contrast to a recent QMC simulation [7].

3.1.4 Obtaining the in-situ density distribution

As can be seen from Eq.(3.3), the contact is naturally normalized by Nk_F, and the detuning by the Fermi energy. However, a question which arises is how to define E_F in our experiment. For a harmonically trapped gas, E_F is defined in terms of the trap parameters $E_{F,\mathrm{trap}} = \hbar(\omega_r^2\omega_z)^{1/3}(6N)^{1/3}$. On the other hand, the Fermi energy of a homogeneous gas is given in terms of its density (in one spin state), n: $E_{F,\mathrm{hom}} = \frac{\hbar^2}{2m}(6\pi^2 n)^{2/3}$. In our experiment, as we increase the power of the hollow light beams, we probe a smaller portion of the gas that is more homogeneous. The relevant Fermi energy, which we use in figures 3.2 and 3.3, is therefore the average of the local (homogeneous) Fermi energy: $E_{F,\mathrm{avg}} = \frac{\hbar^2}{2mN_p}\int P(\mathbf{r})n(\mathbf{r})[6\pi^2 n(\mathbf{r})]^{2/3}\mathrm{d}^3\mathrm{r}$, where $P(\mathbf{r})$ is the detection probability after optical pumping, and $N_p = \int P(\mathbf{r})n(\mathbf{r})\mathrm{d}^3\mathrm{r}$ is the number of atoms probed.

We use the in-situ density distribution, $n(\mathbf{r})$, in order to calculate the average k_F and E_F of the probed atoms. To get $n(\mathbf{r})$, we use the fact that at unitarity the cloud expands hydrodynamically, and the dynamics are governed by the continuity equation. The solution for the continuity equation with harmonic confinement with a time-dependent trapping frequency $\omega(t)$ is self-similar with the following scaling transformation: $r_i(t) = b_i(t)r_i(0)$, where r_i is the spatial coordinate ($i = x, y, z$), and $b_i(t)$ obeys the equation [51, 13]:

$$\ddot{b}_i(t) = -\omega_i(t)^2 b_i(t) + \frac{\omega_i(0)^2}{b_i(t)\left[b_x(t)b_y(t)b_z(t)\right]^{\gamma}} \quad , \tag{3.7}$$

with the initial conditions $b_i(0) = 1$ and $\dot{b}_i(0) = 0$. The constant γ is the characteristic exponent in the equation of state $\mu(n) \propto n^{\gamma}$, where μ is the chemical potential and $\gamma = 2/3$ at unitarity. For a sudden turn off of the trap, $\omega_i(0)$ is the trapping frequency along the i axis, and $\omega_i(t > 0) = 0$.

In figure 3.4, we plot the measured width of the cloud in the axial and radial directions as a function of the expansion time. The data show a rapid increase in the size in the radial (tight) direction of the cloud and almost no increase in the axial direction–a characteristic of hydrodynamic expansion. The solid lines show the numerical solution of Eq.(3.7) with $\omega_r = 2\pi \times 226$ Hz and $\omega_z = 2\pi \times 19$ Hz (which were measured independently), which agrees very well with the data. We find that after 4 ms of expansion the finite resolution of the optical system does not affect the extracted parameters, and therefore we choose this expansion time for the density measurements. We fit the measured density profiles at 4 ms with a Thomas-Fermi distribution, which we find to be general enough for this purpose.

We have tested our density determination method by looking at the ratio of the peak density at unitarity to the peak density of a weakly interacting gas, at low temperatures. The density distribution of the weakly interacting gas is measured using a fit to a Thomas-Fermi distribution after ballistic expansion. For $T = 0$, this ratio is $n_U/n_0 = \xi^{-3/4}$, where ξ at unitarity is a universal constant that relates the chemical potential to the Fermi energy: $\mu = \xi\epsilon_F$. From the measured density ratio at a temperature of $T/T_{F,\mathrm{trap}} = 0.15$, we extract a value of $\xi = 0.40 \pm 0.05$, which is consistent with recent determinations of this universal constant by other groups [30, 8].

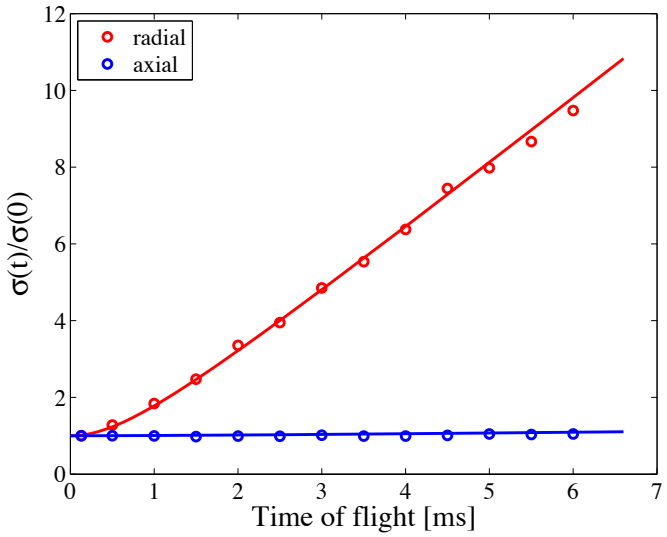

Figure 3.4: Hydrodynamic expansion at unitarity. We start with a weakly interacting gas with $\sim 90,000$ atoms per spin state at $T/T_F = 0.12$ and ramp adiabatically to the Feshbach resonance field. We fit the cloud with a Thomas-Fermi distribution after a variable expansion time and extract the rms widths, $\sigma(t)$, in the radial and axial directions. For the data, we de-convolve the measured width with a gaussian point spread function with an rms width of 2.9 μm, to account for the finite resolution of the optical system. The data is normalized by the initial cloud size, which is 33.4 μm and 2.8 μm in the axial and radial directions, respectively. The solid lines are the numerical solution of the hydrodynamic equation.

The average local Fermi energy can be obtained from the density distribution of the atoms, $n(\mathbf{r})$, and the detection probability, $P(\mathbf{r})$. We measure $n(\mathbf{r})$ by turning the trap off, without applying the hollow light beams, and imaging the cloud after 4 ms of expansion at the resonance. To determine the density distribution in trap, we fit the distribution measured after expansion and rescale the dimensions back to $t = 0$, assuming hydrodynamic expansion [51]. For the fit, we use the Thomas-Fermi distribution, which is known to fit the data well [13].

We obtain $P(\mathbf{r})$ using a model of the optical pumping by the hollow light beams [27]. In the model, we assume that atoms that scatter a single photon are transferred to the dark state, and we account for the attenuation of the hollow light beams as they propagate through the cloud. For a given $n(\mathbf{r})$, the propagation model gives us $P(\mathbf{r})$ after the consecutive application of the two hollow light beams. We note that the results presented in figure 3.3 are not sensitive to the details of the model.

3.1.5 How homogeneous is homogeneous enough?

In figure 3.5, we show the contact at $T/T_F = 0.46$ as a function of the fraction of atoms probed, which is varied by changing the intensity of the hollow light beams. The main part of figure 3.5 shows the contact per particle in units of $k_{F,\mathrm{trap}}$ in order to show the change in the measured signal. We find that the signal increases as we probe fewer atoms near the center of the trapped gas. We compare our results with several theoretical models, where the model lines are calculated by $C_{\mathrm{trap}}^{\mathrm{model}} = \frac{1}{N_p k_{F,\mathrm{trap}}} \int P(\mathbf{r}) n(\mathbf{r}) C_{\mathrm{hom}}^{\mathrm{model}}[T/T_F(\mathbf{r})] k_F(\mathbf{r}) \mathrm{d}^3\mathrm{r}$, with $C_{\mathrm{hom}}^{\mathrm{model}}(T/T_F)$ being the model prediction for a homogeneous contact (normalized to Nk_F), $T_F(\mathbf{r}) = E_F(\mathbf{r})/k_B$ is the local Fermi temperature, and k_B is the Boltzmann constant. We find good agreement of the data with the models.

In the inset of figure 3.5, we plot the contact divided by the average local k_F, defined in the same way as in figure 3.3. For comparison, we also plot theory predictions for the homogeneous contact at the average T/T_F, $C_{\mathrm{hom}}^{\mathrm{model}}(\langle T/T_F \rangle)$, where the notation $\langle\rangle$ stands for density-weighted averaging. A reasonable criterion for homogeneity is when $C_{\mathrm{hom}}^{\mathrm{model}}(\langle T/T_F \rangle) \approx \langle C_{\mathrm{hom}}^{\mathrm{model}}(T/T_F) \rangle$.

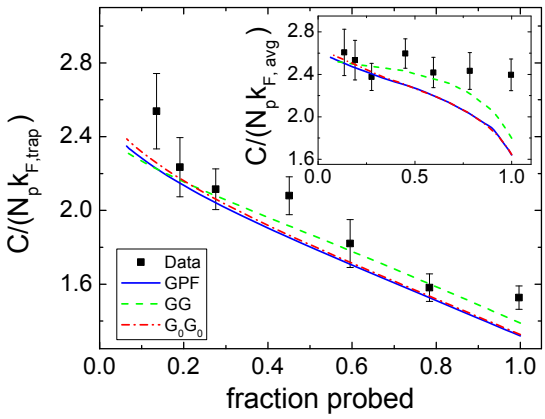

Figure 3.5: Contact versus the fraction of atoms probed for a gas with $T/T_F = 0.46$ at the center of the cloud. In the main plot, the measured contact (squares) is normalized in respect to the trap k_F, and is compared to the predictions of several theoretical models (lines) using the local density approximation. The measured contact increases as we probe fewer atoms at the cloud center, where the local density is largest. The inset shows the contact normalized by the average k_F of the probed atoms (squares), compared to theoretical predictions of the homogeneous contact at the average T/T_F (lines).

When the fraction of the atoms probed is less than 30% we find that this approximation holds to better than 2%. When probing 30% of the atoms, we calculate that the rms spread in the local T_F has been reduced to about 20%. We find that the data for $T/T_F = 0.46$ and fractions lower than 30% agree with theory predictions for a homogeneous gas (see inset of figure 3.5).

3.1.6 The effect of the remaining density inhomogeneity

In figure 3.6, we compare our data to the predictions of several theoretical models. Here we show that the effect of the remaining density inhomogeneity of the probed sample on the theory predictions is negligible. We use the detection probability, $P(\mathbf{r})$, and the density distribution, $n(\mathbf{r})$, for each of the data points, to calculate the average contact predicted by each theoretical model according to:

$$\langle C \rangle = \frac{1}{N_p \langle k_F \rangle} \int P(\mathbf{r}) n(\mathbf{r}) C_{\mathrm{hom}}^{\mathrm{model}}[T/T_F(\mathbf{r})] k_F(\mathbf{r}) \mathrm{d}^3\mathrm{r} \quad , \tag{3.8}$$

where $C_{\mathrm{hom}}^{\mathrm{model}}$ is the prediction for the contact of a homogeneous gas theory (normalized to Nk_F), N_p is the number of probed atoms, and $\langle k_F \rangle$ is the average k_F. The comparison of the average contact, $\langle C \rangle$, and the homogeneous contact for three different models is shown in figure 3.6. The graph clearly demonstrates that (with 30% of the atoms probed) the effect of the remaining density inhomogeneity on the contact is negligible, and hence theories for the homogeneous contact can be compared directly to the data.

3.1.7 Thermometry of a unitary Fermi gas

Thermometry of a strongly interacting gas is not trivial, and different groups have used various techniques, including thermometry with a minority component [8], measurement of the energy versus entropy relation [52], and an empirical temperature extracted from fitting the cloud to a Thomas-Fermi distribution [44]. We base our thermometry on a measurement of the release energy of the gas and the recently reported equation of state [30]. We determine the release energy by taking an image of cloud after 4 ms of expansion at unitarity. Knowing our trapping potential, the equation of state, and the generalized virial theorem at unitarity [52], we are left with only

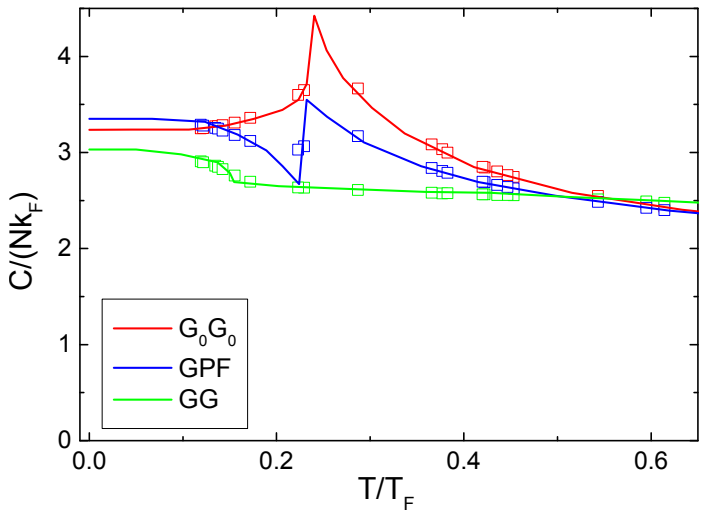

Figure 3.6: Comparison of the homogeneous contact calculated by several theoretical models (solid lines) and the contact averaged over the remaining density inhomogeneity when probing the central 30% of the cloud for the same models (open symbols). The excellent agreement of the points and the lines shows that the effect of the remaining density inhomogeneity on the contact data can be neglected. See text for the explanation of the theories.

the temperature, T, as a free parameter in the calculation of the release energy. We find T by matching the calculated energy to the measured one. We estimate that the one sigma uncertainty in the temperature is 5%. When reporting T/T_F in figure 3.3, we use $T_F = E_{F,\mathrm{avg}}/k_B$.

Our thermometry assumes a knowledge of the trapping potential $V(\mathbf{r})$ and the equation of state $n(\mu, T)$, where T is the temperature and μ is the chemical potential. For a non-interacting gas the equation of state is known, and for the unitary gas, we use the equation of state recently measured at MIT [30]. The trapping potential is calibrated from the known optical trap beam waists and the measured oscillation frequencies in all three directions. We adopt a local density approximation approach; the local chemical potential is given by $\mu(\mathbf{r}) = \mu_0 - V(\mathbf{r})$. For a given T and number of atoms, N, μ_0 is set by the normalization requirement $N = \int n[\mu(\mathbf{r}), T]\,\mathrm{d}^3\mathrm{r}$. The equation of state then determines the complete density profile $n(\mathbf{r})$, from which we can calculate other quantities such as the entropy, total energy, release energy, and shape of the cloud. Since we measure N, we get a one-to-one correspondence between T and these quantities, and therefore any of them can serve as a thermometer. With the unitary gas, we have chosen to use the release energy as a thermometer.

The release energy per particle is calculated from the measured density profile of the expanded gas using

$$E_{\mathrm{rel}} = \sum_{i=x,y,z} E_{i,\mathrm{rel}} = \frac{1}{N} \sum_{i=x,y,z} \int \frac{m}{2} \left(\frac{r_i}{t}\right)^2 [n_t(\mathbf{r}) - n_0(\mathbf{r})]\mathrm{d}^3\mathrm{r} \quad , \tag{3.9}$$

where r_i is the corresponding spatial coordinate ($i = x, y, z$), t is the expansion time, and $n_t(\mathbf{r})$ is the density distribution at time t. In the experiment, we use $t = 4$ ms. We have verified that the release energy measured at $t = 4$ ms is the same as that measured after 12 ms of expansion. For a given potential $V(\mathbf{r})$, the release energy is given by [52]:

$$E_{\mathrm{rel}} = \frac{1}{2}\langle \mathbf{r} \cdot \nabla V(\mathbf{r}) \rangle \quad , \tag{3.10}$$

where the symbol $\langle\rangle$ stands for the density-weighted average: $\langle g(\mathbf{r})\rangle = \frac{1}{N}\int g(\mathbf{r}) n(\mathbf{r}) \mathrm{d}^3\mathrm{r}$. By equating the calculated $E_{\mathrm{rel}}(T)$ to the measured E_{rel}, we determine T.

As a comparison, we have used two other techniques to extract the temperature of the unitary

gas. The first technique we compare to is based on the widely used practice of fitting the strongly interacting gas to a Thomas-Fermi distribution and extracting an empirical temperature, $\tilde{T}$, from the fitted fugacity [44]. At $T = 0$, the empirical temperature is connected to the real temperature by $T = \tilde{T}\sqrt{\xi}$, where ξ is the universal constant defined above [13]. Albeit without a complete theoretical justification, one can then extend this to finite temperatures and extract T [44]. In the following analysis, shown as the blue triangles in figure 3.7, we used $\xi = 0.376$ [30].

The second thermometry method we compare to is based on the entropy of the weakly interacting gas before the ramp to unitarity. We calculate the entropy of the weakly interacting gas from the measured temperature and the trapping potential. In the experiment, we start from the weakly interacting gas and slowly ramp to the Feshbach resonance field. By performing this ramp there and back and comparing the entropy before and after the ramp for a gas initially at $T/T_F = 0.12$ and $T/T_F = 0.22$, we have determined that the entropy increases by about 6% when going to the Feshbach resonance field. Assuming this increase, we use the entropy of the unitary gas together with the equation of state as the thermometer. In figure 3.7, the T/T_F we obtain from these two additional techniques are plotted against the release energy thermometry. We find a good agreement between all the three techniques up to $T/T_F = 0.4$. Above that temperature, the empirical temperature technique becomes unreliable since the effect of quantum degeneracy of the shape of the cloud diminishes. The entropy technique starts to show a small systematic deviation upwards above $T/T_F = 0.4$. The close agreement of the three techniques, which are based on independent observables, up to $T/T_F = 0.4$ gives us confidence in our thermometry. To estimate the errors in T we look at the difference between the entropy and release energy thermometry techniques.

In summary, we have presented a measurement of the homogeneous contact of a unitary Fermi gas versus temperature. Our measurement is based on a novel technique that allows us to probe local properties of the cloud. Our data show good agreement with theory predictions for $T/T_F > 0.4$, but at lower temperatures no single prediction fully agrees with the data. Furthermore, the data do not show an enhanced narrow peak around T_c, which was predicted to exist due to

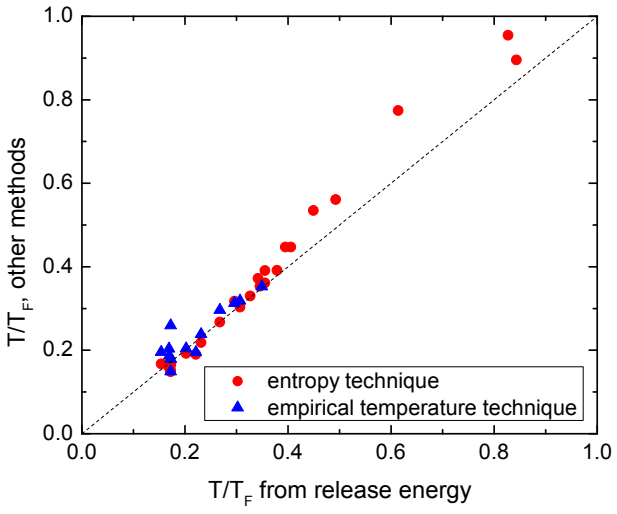

Figure 3.7: Comparison of different thermometry methods. The x-axis is the temperature, T/T_F, where T_F is the trap Fermi temperature, as extracted from the release energy. The y-axis is the temperature we get from the two other thermometry methods (see text for more details). The dashed line is $y = x$.

pair fluctuation in a pseudogap phase.

To provide additional insight into the nature of the normal state of the unitary Fermi gas, I will describe the momentum-resolved RF spectroscopy technique combined with the donut beam in the next section.

3.2 The spectral function of a strongly interacting Fermi gas

The spectral function provides the information about the modification of single particle states due to interaction. A free particle, which shows a quadratic dispersion, is modified to a quasi-particle with an effective mass as interaction increases. When the system is strongly interacting, due to pairing, the single-particle dispersion can also be negative. The measurement of such single-particle excitation spectrum provides us with an insight on the many-body behavior of the system [53].

In condensed matter experiments, the spectral function can be measured by a technique called Angle Resolved Photoemission Spectroscopy (ARPES). ARPES involves shining a laser on the surface of a material and measuring the momentum (k) and the energy ($\epsilon_k = \hbar k^2/2m$) of the ejected electrons. From this information and using the energy and momentum conservation, the spectral intensity can be calculated. The energy of the electrons on the surface is given by,

$$E_s(k) = \epsilon_k + \phi + h\nu \tag{3.11}$$

where ϕ is the work-function of the system and $h\nu$ is the photon energy of the incident beam. The energy E_s gives the dispersion of the system. The spectral function thus measured is the imaginary part of the Green's function in many-body theories. The spectral intensity probed in an ARPES experiment is given by [53],

$$I_{ARPES}(\mathbf{k}, \omega) = f(\omega) M_0(\mathbf{k}, \omega) A(\mathbf{k}, \omega), \tag{3.12}$$

where $f(\omega)$ is the Fermi function, $M_0(\mathbf{k}, \omega)$ is a matrix element which comes from the selection

rule and $A(\mathbf{k},\omega)$ is the spectral function. Because of the Fermi function, the spectral intensity measured with ARPES only contains the information about the occupied spectral function. The spectral function is related to the Green's function $G(\mathbf{k},\omega)$ [54], as,

$$A(\mathbf{k},\omega) = -\frac{1}{\pi} Im(G(\mathbf{k},\omega). \tag{3.13}$$

The Green's function for an interacting fermion is well-known and given by,

$$G(\mathbf{k},\omega) = \frac{1}{\omega - \epsilon_k - \Sigma(\mathbf{k},\omega)}. \tag{3.14}$$

Here, $\Sigma(\mathbf{k},\omega)$ is called the self-energy. The real part of this term contains the information about the effective mass and the imaginary part contains the information about the lifetime of the quasi-particles. Thus, measuring the single particle spectral function of the interacting fermionic system gives us an insight on the most important properties of the system.

3.2.1 Momentum-resolved RF spectroscopy

Our group developed a technique analogous to ARPES to measure the single particle spectral function of an interacting Fermi gas. This technique that is called momentum-resolved RF spectroscopy (or atom photoemission spectroscopy) is an extension of RF spectroscopy work as described in the previous section. The atoms outcoupled by RF photons, in our case, are equivalent to electrons ejected from the material in ARPES. In addition to measuring the outcoupled atoms as a function of RF frequency, we also resolve their momentum after a TOF thus allowing us to get the spectral function. Since, the momentum imparted by the RF photons is negligible, we can get the spectral function by simply using the conservation of energy. The matrix element $M_0(\mathbf{k},\omega)$ in our case is 1. The only requirement for momentum-resolved RF spectroscopy is that the outcoupled atoms do not interact with the remaining two-spin states. In our case, for ^{40}K atoms, the scattering length between the outcoupled atoms in $m_F = -5/2$ and the remaining atoms in spin states $m_F = -9/2$ and $m_F = -7/2$ is around $200a_0$. The interaction effect is negligible enough to measure the momentum distribution after a ballistic TOF expansion. Also, the final-state effect after RF spectroscopy is negligible at this interaction strength.

3.2.2 Experimental Sequence

The experiments are performed with an ultracold gas of ^{40}K atoms in an optical dipole trap. The trapping frequencies are 243 Hz and 21.3 Hz in the radial and axial directions, respectively, with the axial direction of the trap oriented horizontally. The final stage of evaporative cooling is performed at a magnetic field of 203.3 G, after which the field is swept linearly in 50 ms to the final value where we carry out the PES measurement. The initial temperature of the weakly interacting gas, before the adiabatic sweep, is $T_0 = (0.16 \pm 0.02)T_F$ [an exception is the farthest point on the BCS side, where $T_0 = (0.13 \pm 0.02)T_F$]. From our previous measurements of the release energy at unitarity (described in the previous section), we estimate that the temperature at unitarity is $(0.18 \pm 0.02)T_F$. The gas has 80,000 to 120,000 atoms per spin state and is cooled such that the temperature is just above T_c after a sweep to the Fano-Feshbach resonance at 202.20 G [12]. We verified that for all interaction strengths the condensate fraction is less than 1%.

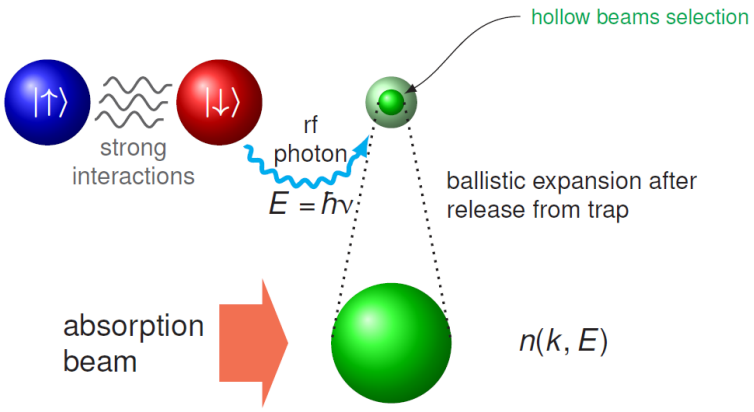

Figure 3.8: Momentum-resolved RF spectroscopy. The atoms in one of the strongly interacting spin states are outcoupled to a third spin state. Since the outcoupled atoms have weak interaction with the atoms in remaining spin states, the momentum distribution and energy of these atoms can be measured after a balistic TOF expansion. The donut beam technique is employed on the outcoupled atoms right before TOF to select the homogeneous sample.

The atom PES measurement uses an rf pulse with a Gaussian field envelope that has an rms

width of 51 μs (17 μs), and a total duration of 300 μs (100 μs), for $\nu < 34$ kHz ($\nu \geq 34$ kHz). We use shorter pulses at higher ν to minimize effects due to the motion of the spin-flipped atoms during the rf pulse. The rf detuning ν is given with respect to the resonant transition frequency ν_0, which is measured for a spin polarized gas. For each PES measurement, we take data for the same 25 values of ν, each of which is repeated three times. The rf power is increased for larger ν, while keeping the fraction of spin-flipped atoms less than 40%. As in the RF spectroscopy work to measure Tan's contact, we measure the dependence of the number of spin-flipped atoms on the rf power, and scale the measurements done at different rf powers to correspond to a common level.

Immediately after the rf pulse, and exactly at trap release, we pulse on the hollow-core light beams, which propagate perpendicularly to each other and intersect at the center of the cloud [20,21]. The frequency of these beams is chosen to optically pump atoms from the $|9/2, -5/2\rangle$ state into the upper hyperfine manifold ($F = 7/2$), where they are invisible to our imaging. Both the rf pulse and the spatially selective optical pumping, which is pulsed for 40 μs, are completed in a timescale that is short compared to motion of atoms in the trap. We typically probe the $|9/2, -5/2\rangle$ atoms that came from the central 30% of the cloud; we find this fraction to be a good compromise between spatial selectivity and signal-to-noise ratio [20,21]. As described in Ref. [3], just before imaging the cloud, we remove the remaining atoms from the $|9/2, -9/2\rangle$ and $|9/2, -7/2\rangle$ states and then transfer the outcoupled atoms in the $|9/2, -5/2\rangle$ state to the $|9/2, -9/2\rangle$ state with two short rf π-pulses. This procedure enables us to image the atoms on the cycling transition, which improves the signal-to-noise ratio.

3.2.3 Two-mode fitting function

Similar to the analysis done in electron systems, we use a two-mode function to describe the PES signal [55]:

$$I(k, E) = Z I_{\text{coherent}}(k, E) + (1 - Z) I_{\text{incoherent}}(k, E) \quad , \tag{3.15}$$

where the first part describes quasiparticles with a positive dispersion, the second part accommodates an "incoherent background" that exhibits negative dispersion, and Z is the quasiparticle

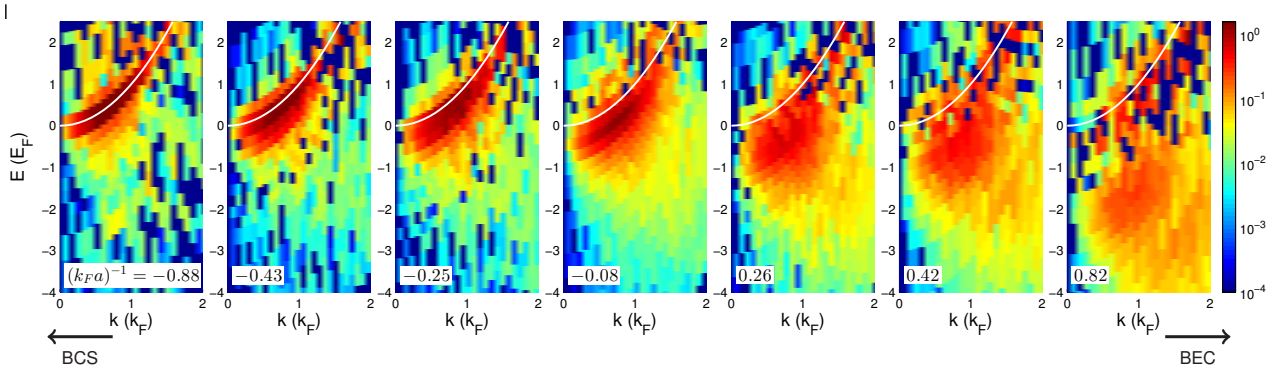

Figure 3.9: Momentum-resolved RF spectroscopy data taken at $T > T_c$ (see text) as a function of interaction strength. The color represents the probability distribution of atoms at a given E and k in the strongly interacting gas. The white line is the quadratic dispersion of free particles.

spectral weight. When these two parts (defined below) are combined, the resulting dispersion can exhibit back-bending.

The quasiparticles in Fermi liquid theory are long-lived and therefore give rise to narrow energy peaks, which, in principle, could be directly observed. However, such peaks would be broadened by our experimental resolution of about $0.25E_F$. This resolution is set by the number of atoms (with E_F scaling only weakly with increasing N) and the rf pulse duration, which must be short compared to the harmonic trap period in order to probe momentum states. We convolve Eqn. 3.15 with a Gaussian function that accounts for our energy resolution before fitting to the data in order to determine the spectral weight of the quasiparticles (Fig. 1d, upper panel).

To describe quasiparticles, we use

$$I_{coherent}(k,E) = 4\pi k^2 \cdot \delta(E - \frac{k^2}{m^*} - E_0) \frac{\left[-(\pi m^* T)^{3/2} \,\mathrm{Li}_{3/2}\left(-\exp\left(\frac{-E_0+\mu}{T}\right)\right)\right]^{-1}}{\exp\left(\frac{E-\mu}{T}\right)+1} \quad , \qquad (3.16)$$

which consists of a quadratic dispersion of sharp quasiparticles multiplied by a normalized Fermi distribution (δ is the Dirac delta function, and Li is the polylogarithm function). We include as fit parameters, a Hartree shift E_0, effective mass m^*, chemical potential μ, and temperature T. Here, energies are given in units of E_F and m^* in units of m, the mass of a ^{40}K atom. This description of Fermi liquid quasiparticles is typically only used very near k_F and for T approaching zero, whereas we fit to data for a larger range in k and with temperatures near 0.2 T_F (just above T_c). The latter is necessitated by the unusually large interaction energy compared to E_F, and we note that 0.2 T_F is still sufficiently cold that one can observe a sharp Fermi surface in momentum, as described in Chapter 2. Any increase in quasiparticle widths away from k_F will have little effect on the data as long as the quasiparticles have an energy width less than our energy resolution, which should be the case for long-lived quasiparticles.

The second part in Eq. 3.15 needs to accommodate the remainder of the signal, which is often referred to as an "incoherent background" in a Fermi liquid description. For fermions with contact interactions, one expects an incoherent background at high momentum due to short-range pair correlations [34, 9, 56]. Motivated by this and by the normal state in the BEC limit, we use

for $I_{\text{incoherent}}$ a function that describes a thermal gas of pairs. The pairs have a wave function that decays as $\exp(-r/R)$, where r is the relative distance and R is the pair size [57], and a Gaussian distribution of center-of-mass kinetic energies characterized by an effective temperature T_p. This gives

$$I_{\text{incoherent}}(k,E) = \Theta\left(-E_p - E + k^2\right) \frac{8k\sqrt{\frac{E_p}{T_p}} e^{\frac{E_p+E-3k^2}{T_p}} \sinh\left(\frac{2\sqrt{2}k\sqrt{-E_p-E+k^2}}{T_p}\right)}{\pi^{3/2}\left(E-k^2\right)^2} \tag{3.17}$$

where Θ is the Heaviside step function, E_p is a pairing energy defined by $k_F R = \sqrt{2/E_p}$, and both E_p and T_p are dimensionless fitting parameters. While this description of the incoherent piece may not fully capture the microscopic behavior except in the BEC limit, we find nonetheless that Eq. 3.15, after convolution with a Gaussian function that accounts for our energy resolution, fits the data very well throughout the crossover.

In Figure 3.10, we show Z as a function of $(k_F a)^{-1}$. For our lowest $(k_F a)^{-1}$, $Z \approx 0.8$; however, Z decreases rapidly going from the BCS side of the crossover (negative a) to the BEC side (positive a), reaching $Z \approx 0.3$ at unitarity. Beyond $(k_F a)^{-1} = 0.28 \pm 0.02$, Z vanishes, signalling the breakdown of a Fermi liquid description. Restricting the fitting to a smaller region around k_F gives results for Z that are consistent with the fits to $k \leq 1.5$ (see Fig. 3a). We note that the interaction strength where Z vanishes, as well as the sharpness with which Z goes to zero, are likely to be temperature dependent [58]. The best fit values for the effective mass, m^* are shown in Fig. 3b, where m^* increases with increasing interaction strength as expected for a Fermi liquid. A linear fit gives $m^* = 1.21 \pm 0.03$ at unitarity, which is somewhat higher than $m^* = 1.13 \pm 0.03$ measured in Ref. [21], but close to the $T = 0$ prediction of $m^* = 1.19$ from Ref. [10].

3.2.4 Energy Distribution Curves

Energy Distribution Curves, commonly known as EDCs, are the cut of the spectral function at a given momentum. The width of these curves give the information on lifetime of the quasiparticles and the peak gives the dispersion. An example of an energy distribution curve is shown in Figure 3.11, which is taken at $(1/k_F a = -0.08)$. The circles are the data points and the lines come from

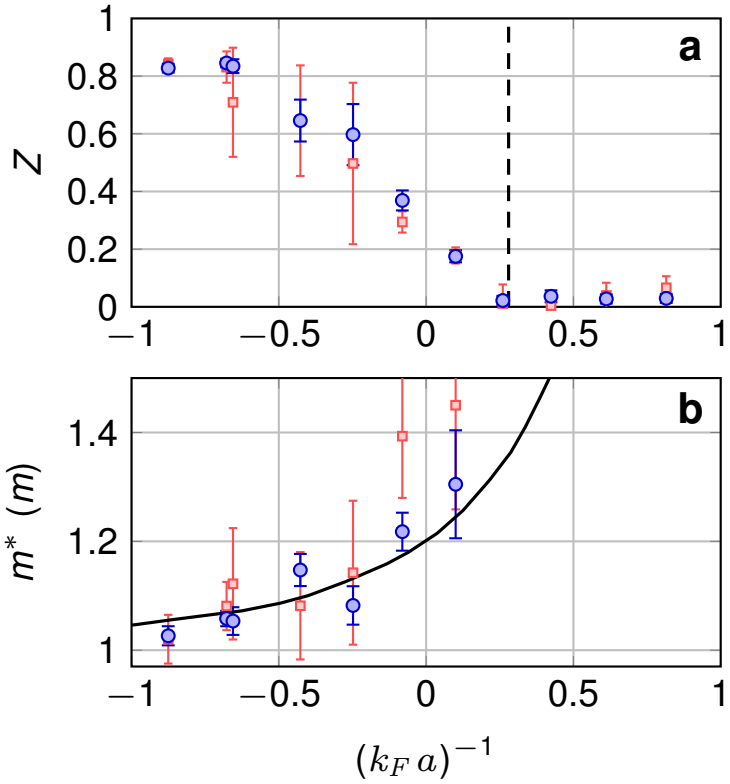

Figure 3.10: The quasiparticle residue Z and the effective mass m^* as a function of the interaction strength. Both of them are the fit parameters in Equation 3.15.

a single surface fit using the two-mode fitting function. In this case, the fit parameters are $Z = 0.37(3), m* = 1.22(3), T = 0.25(2), E_0 = -0.33(2), \mu = 0.19(4), E_p = 0.23(4)$, and $T_p = 1.09(8)$. The reduced χ^2 of this fit is 1.2.

3.2.5 Contact vs interaction strength

As $(k_F a)^{-1}$ increases, short-range correlations are expected to increase. This gives rise to increased weight in the high-k part of the spectral function [56], which is quantified by a parameter called the contact [34, 9, 38, 48]. In a Fermi liquid description, the contact must be accounted for by the incoherent part of the spectral function [56].

We note that our particular choice for $I_{\text{incoherent}}$ has the expected form of a $1/k^4$ high-k tail in the momentum distribution [34] and a $1/\nu^{3/2}$ large-ν tail in the rf line shape [9], where ν is the rf detuning. Remarkably, we find that the contact can be accurately extracted from the fits to the PES data even though we restrict the fits to $k \leq 1.5$. For comparison, $1/k^4$ behavior in the momentum distribution was observed for $k > 1.5k_F$ [38].

In Figure 3.12, we plot the measured contact per particle, C/N, in units of k_F, as a function of $(k_F a)^{-1}$. The data extend previous measurements of the contact at unitarity [48, 44] and agree well with several theoretical predictions [6, 10].

3.2.6 Conclusion

The results presented here can explain how different observations lead to different conclusions regarding the nature of the normal state of the unitary Fermi gas. Although the data here taken just above T_c show that a Fermi liquid description breaks down for $(k_F a)^{-1} \geq 0.28 \pm 0.02$, Z remains finite at unitary. Fermionic quasiparticles may play a key role in thermodynamics, while PES data reveal back-bending and significant spectral weight in an "incoherent" part that is consistent with pairing.

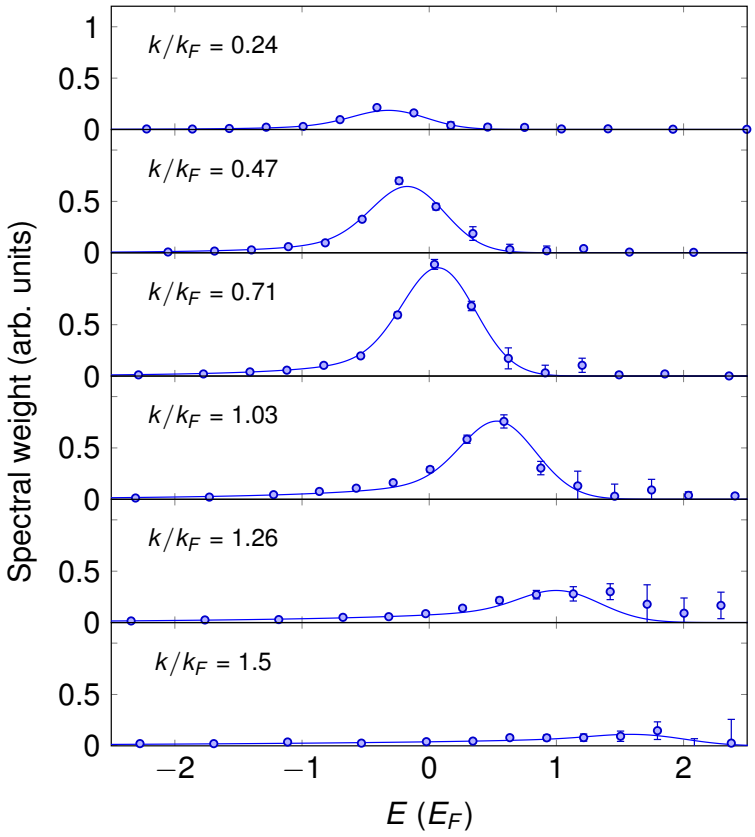

Figure 3.11: Energy Distribution Curves at $1/k_F a = -0.08$. Each panel is the cut of the spectral function at the given k/k_F. The circles are data and the lines are the fits.

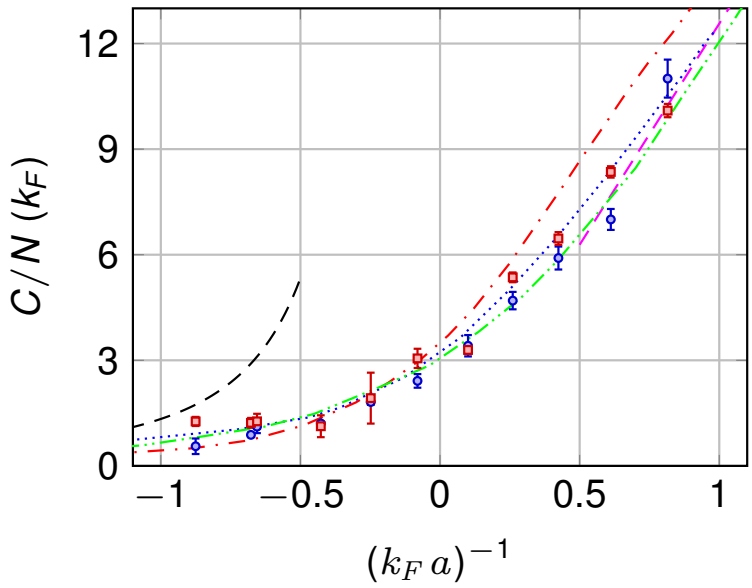

Figure 3.12: The contact density per particle (in units of k_F) for a homogeneous Fermi gas above T_c is shown versus $(k_F a)^{-1}$. The contact measured from the tail of the rf lineshape (blue circles) agrees well with the contact extrapolated from the fits of the PES data (red squares). For comparison, we also plot the BCS (dashed black line) and BEC (dashed magenta line) limits, given by $4(k_F a)^2/3$ and $4\pi(k_F a)^{-1}$, respectively [9], the non-self-consistent t-matrix at $T = 0$ (dotted blue line) and its Popov version at T_c (dash-dotted red line) [6], and the self-consistent t-matrix model at $T = 0$ (double-dotted green line) [10]. We find that the contact measured above T_c agrees well with the $T = 0$ theories.

Chapter 4

New Generation Fermi Gas Apparatus Design

In 2012, we decided that the first generation potassium Fermi gas experiment apparatus was becoming outdated. We were running the last (out of four) potassium dispensers, and expected to exhaust the source within a few years. We started planning for a new generation apparatus in 2012 and started early work of assembling optics, electronics and vacuum chambers in 2013. In December 2014, the very first Fermi gas apparatus was disassembled, and we put all our efforts to the new generation apparatus starting in January 2015.

The new Fermi gas apparatus (Figure 4.2) consists of three chambers. In the first chamber, we put potassium dispensers and make a MOT. The atoms collected in the first MOT are pushed to the second chamber through a differential pumping tube to the second chamber where we make another MOT. The second chamber has a much longer vacuum lifetime, so we can trap more atoms and perform sub-Doppler gray molasses cooling. Atoms are then loaded into a purely magnetic quadrupole trap and transferred to the science cell with a "cart". We do subsequent cooling of the atoms in magnetic and optical dipole traps in this cell down to quantum degeneracy.

4.1 Vacuum chambers

4.1.1 Dispenser Chamber

The dispenser chamber (Figure 4.1) is a 6-way cross glass cell made by Ron Bihler at Precision Glassblowing, Denver. It is made up of pyrex and has six 1.5"(3.81 cm) diameter windows for MOT light. Additionally, there are three 0.5" (1.25 cm) diameter windows, which will be used for push

beam and MOT fluorescence detection. The chamber has two arms for atomic sources. We put an enriched source of potassium chloride (bought from Trace Sciences International at $240 per mg in 2011) in one of them (see the description of how to make the potassium dispensers in Appendix), and we put Rb getters in the second arm. We later noticed that the enriched potassium salt price has increased by four fold starting in 2013. The arms have a diameter of 1.1" (2.8 cm) where the source-boats are placed and are reduced to 0.868" (2.2 cm) tubes that fuse to the main chamber.

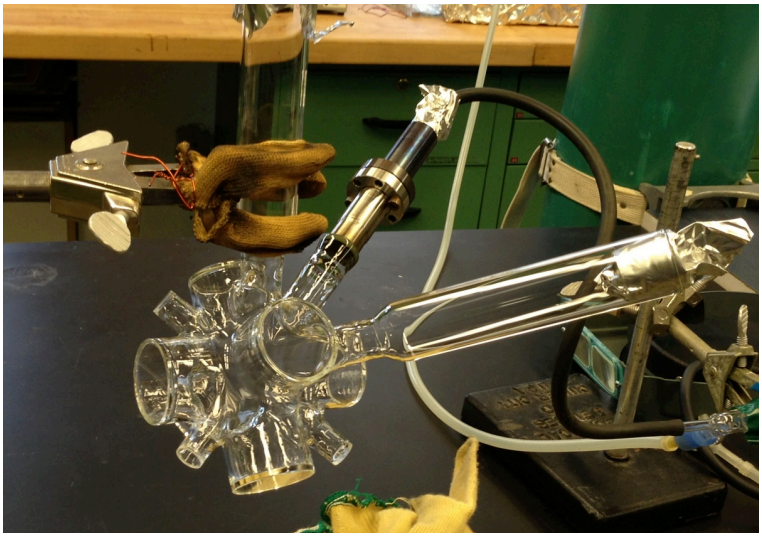

Figure 4.1: Six-way cross glass chamber which contains the atomic source for the system. The potassium atoms are collected in a 3D MOT in the first stage of the experiment.

A transfer tube is fused to the glass chamber with a 2.73" (6.93 cm) long glass tube with a diameter of 0.75 in (1.91 cm). This tube has a glass-to-metal transition to a stainless steel with a 1.33" (mini) CF. A longer stainless steel transfer tube, custom made by MDC Vacuum, is attached to the mini flange. The transfer tube has a length of 10" (25.4 cm) and an inner diameter of 1.1 cm. The diameter is chosen to allow for a good differential pumping between the dispenser chamber and the main MOT-chamber. The other end of the transfer tube has a 2.75" regular CF, which is connected to the main MOT-chamber.

4.1.2 Second MOT-chamber

To save time from glass-chamber manufacturing work, we bought a commercially available stainless steel chamber for our main MOT-chamber. It's a 6-inch Spherical Octagon Chamber from Kimball Physics (MCF600-SphOct-F2C8). The chamber consists of eight 2.75" (6.99 cm) ports and two 6" (15.24 cm) ports. Four of the 2.75" ports and the 6" ports are used for MOT beams. One of the 2.75" port is connected to the transfer tube coming from the dispenser chamber side and the port orthogonal to it is connected to the transfer tube to the science cell. One of the 2.75" port is used for pumping.

The viewports needed for MOT and optical pumping are also bought from Kimball Physics (MCF275-MtgFlg-C1VP and MCF600-MtgFlg-F1VP). The viewports are made up of Corning type 7056 glass.

A pump arm is attached to the spherical octagon chamber. The arm is primarily used for pumping out the dispenser chamber and the octagon chamber. The arm consists of a titanium-sublimation pump (Gamma Vacuum TSP,3 FILAMENT,2.75 CF,MS,STD) and a 75 L/s ion-pump (Gamma Vacuum 75S-CV-4V-SC-N-N). A reducer (MDC ConicalReducer, 4.5"x 2.75") is used to connect the spherical octagon chamber to a four-way cross (MDC 4-WayCross, 4.5"). The TSP is attached to the upper port with another reducer (MDC ConicalReducer, 4.5"x 2.75"); the ion pump is attached to the side and the lower port is used for the initial pumping with a turbo-molecular pump. We use a zero-length reducer (MDC ZeroLengthReducer, 3.38"x2.75"Tapped) to connect the four-way cross with a angle-valve (Lesker, Manual SS All-Metal Angle Valve CF flanged). A turbo-molecular pumping station is attached to the valve during the initial pumping stage and later removed after closing the valve. The port is then sealed off with a CF blank.

The second transfer tube, which connects the second MOT chamber with the science cell, consists of a reducer, an all-metal-gate-valve, a four-way cross and a glass-to-metal transition section to the science chamber. The atoms move 20.87" (53 cm) from the center of the MOT cell to the center of the science cell.

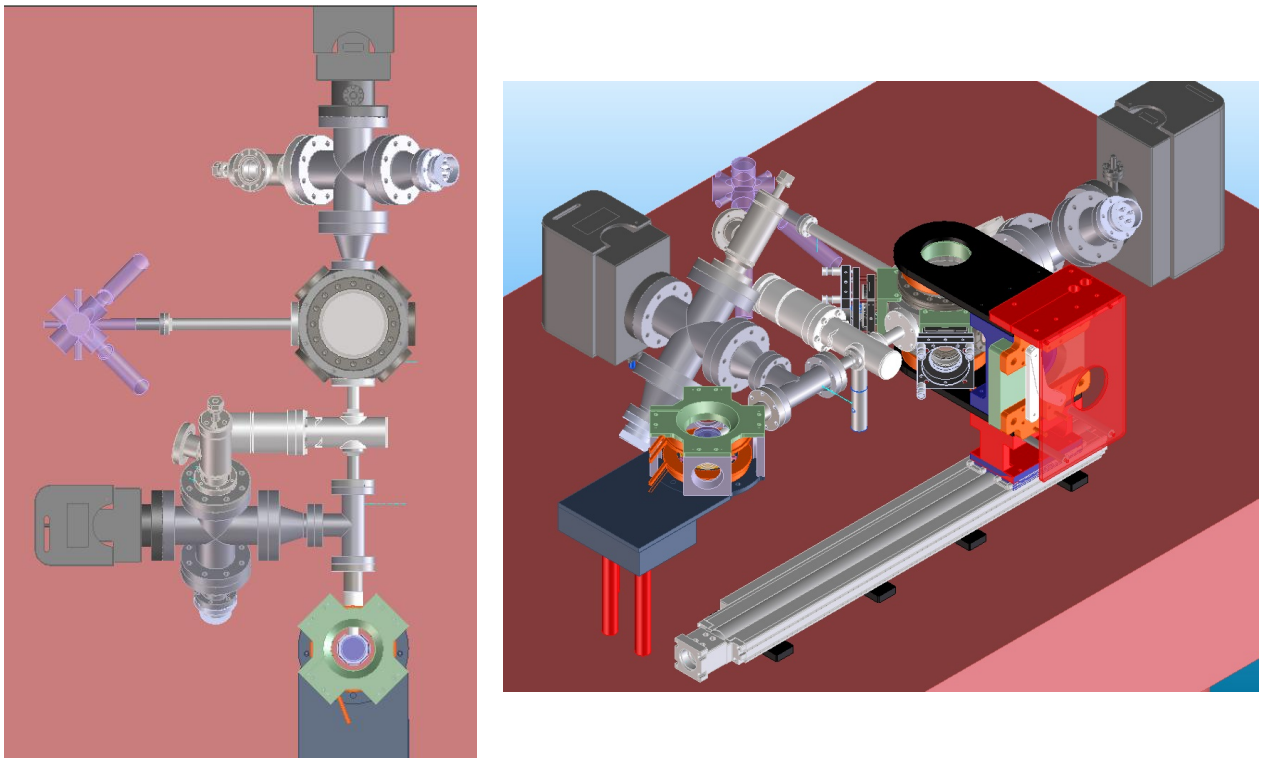

Figure 4.2: CAD Drawings of the apparatus. Left: Top view, Right: Side View

The all-metal-gate-valve (VAT Inc. All-metal gate valve DN 16(5/8")) serves the purpose of separating the MOT section from the science chamber. We put it there such that we can easily change the source or make changes to the science chamber without having to rebake the entire apparatus.

There is another pump arm attached to the science cell that is similar to the first pumping arm except we use a 40 L/s pump (Gamma Vacuum 45S-2V) instead of a 75 L/s pump because the surface area of the science cell is much smaller than that of the Kimball octagon cell. A zero-length reducer (MDC Vacuum ZeroLengthReducer, 2.75"x1.33") is attached to the cross, which is then attached to another 4-way cross (MDC Vacuum 4-WayCross, 2.75"). Like in the pumping arm #1, a TSP (Gamma Vacuum TSP,3 FILAMENT,2.75 CF,MS) is attached to the upper port and the ion-pump is attached to the side. The lower port is used for pumping with a turbo-molecular pump during the initial stage of vacuum pump-down.

4.1.3 Science Cell

The science chamber (Figure 4.3) is designed by Jay Meikrantz from Precision Glassblowing, Denver and is based on the cell designed by Jay for Adam Kaufman (Regal lab) . The cell is designed to have a large optical access enabling us to have beams for a 3D-lattice and also have a high resolution imaging. It is an all-glass spherical octagon with seven 0.625" (1.59 cm) windows. The top and the bottom of the cell consists of a 1.7" (4.32 cm) windows. The chamber is attached to a 1.33" (mini) flange with a glass-to-metal transition tube with a diameter of 1.9 cm.

The cell is coated inside and out such that it has a good transmission of both 767 nm and 1064 nm beams. Figure 4.4 shows the transmission data we measured for a large and a small window before they were assembled.

Figure 4.3: The Science Cell: the cell is manufactured by Precision Glassblowing in Denver and has seven 0.625" windows and two 1.7" that are double AR-coated at around 767 nm and 1064 nm.

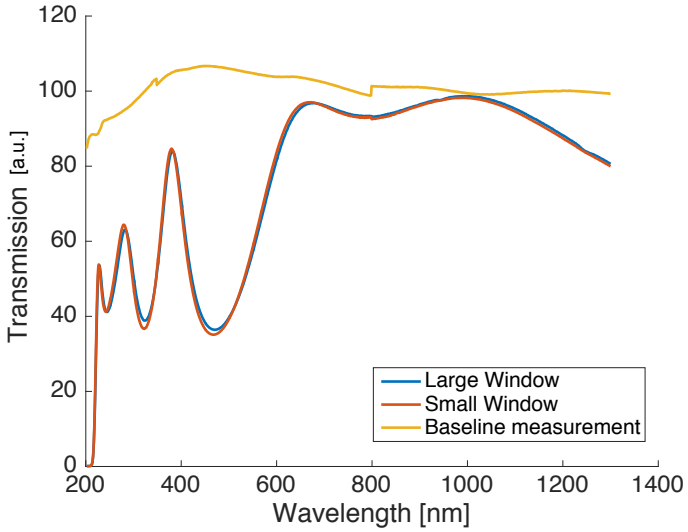

Figure 4.4: Transmission data for the science cell windows. The windows are AR coated for 767 nm and 1064 nm light on both sides. The baseline measurement was done without any windows in place.

4.2 Pumping Speed Calculations

4.2.1 Basics

Considering the nature of the gas and the relative quantity of gas through a tube, the gas flow can be either in the continuum flow or in the molecular flow regime [59]. In the high pressure regime, the gas flow can be either viscous or turbulent, and is termed continuum flow. All of the pressures we work at ($< 10^{-9}$ Torr) are described by the molecular flow regime in which the mean free path is long compared to the tube size making the flow dynamics entirely governed by gas-wall collisions.

The quantity that describes the flow in a tube is called conductance (C), which is measured in L/s. The conductance of a cylindrical tube in the continuum flow regime is given by [59],

$$C[\mathrm{L/s}] = 78\frac{d^3[\mathrm{in}^3]}{l[\mathrm{in}]} \tag{4.1}$$

where d is the tube diameter in inches and l is the length of the tube in inches. The coefficient includes all the factors for units conversion.

When there are multiple tubes connected in either series or parallel, the total conductance follows the following equations:

$$\frac{1}{C_{\mathrm{total}}} = \sum_i \frac{1}{C_i} \rightarrow \text{Series Conductance} \tag{4.2}$$

$$C_{\mathrm{total}} = \sum_i C_i \rightarrow \text{Parallel Conductance,} \tag{4.3}$$

where the symbols used are obvious.

Similarly, when there is a 90 degree elbow in a tube, Monte Carlo simulations have shown that the conductance is reduced to 22% of the original conductance.

Another important quantity in the calculation is the pumping speed. The chamber surfaces outgas with a certain rate depending upon the material. These outgassed materials need to be pumped out to maintain a desired vacuum pressure. The pumping speed depends on the

conductance of the tube to which it is connected. The effective pumping speed is given by,

$$\frac{1}{P_{\text{effective}}} = \frac{1}{P_{\text{pump}}} + \frac{1}{C}, \tag{4.4}$$

where $P_{\text{effective}}$ is the effective pumping speed at the chamber, P_{pump} is the pumping speed of the vacuum pump and C is the conductance of the tube which connects the vacuum chamber with the vacuum pump.

We will usually have an idea of the effective pumping speed we want based on the following equation,

$$\text{Pumping speed} = \frac{\text{outgassing rate} \times \text{surface area}}{\text{Desired Pressure}}. \tag{4.5}$$

4.2.2 Conductance in our vacuum system setup and pressure estimates

The outgassing rate depends upon the materials and temperature used. For a baked 316L stainless steel, it is 2×10^{-13} Torr L/s cm^2. Because we have an idea of the effective pumping speed, we use Eq. 4.4 to calculate the required pumping speed of the vacuum pump.

The conductance of the tube that connect the dispenser chamber and the main MOT chamber is given by,

$$C_{12} = 78 \times \frac{0.43^3}{14.54} = 0.43 \text{ L/s}. \tag{4.6}$$

Now, let's calculate the conductance of the pumping arm. First, let's estimate the conductance of the cone,

$$C_{\text{cone}} = \frac{1}{2} \times 78 \times \frac{1.375^3 + 2.375^3}{2.95} = 211 \text{ L/s}. \tag{4.7}$$

The conductance of the cross is,

$$C_{\text{cross}} = 78 \times \frac{2.375^3}{6.73} = 155 \ L/s \tag{4.8}$$

Hence, the net conductance of the pumping arm is,

$$C_{\text{pump arm}} = (C_{\text{cone}}^{-1} + C_{\text{cross}}^{-1})^{-1} = 89 \text{ L/s} \tag{4.9}$$

The total conductance from the dispenser MOT to the ion pump is,

$$C_{\text{1P}} = (C_{12}^{-1} + (0.3 \times C_{\text{pump arm}})^{-1})^{-1} = 0.43 \ L/s \tag{4.10}$$

We have a 75 L/s pump in this arm but the effective pumping speed in the dispenser chamber is dominated by the transfer tube which is 0.43 L/s. Considering the outgassing rate of Pyrex from the glass cell [59], the estimated pressure in the dispenser chamber is given by,

$$P = \frac{\text{surface area} \times \text{outgassing rate}}{\text{pumping speed}} \tag{4.11}$$

$$= \frac{(195 \text{ cm}^2 \times 1.5 \times 10^{-10} \text{ Torr L/s/cm}^2)}{0.43 \text{ L/s}} = 7 \times 10^{-8} \text{ Torr} \tag{4.12}$$

Next, the main MOT chamber. The effective pumping speed is the same as the conductance of the pump arm, which is 41 L/s. The surface area is 687 cm^2 and the outgassing rate of stainless steel is 10^{-13} Torr L/s/cm^2. Hence, the estimated pressure is 1.7×10^{-12} Torr.

Next, let's calculate the effective pressure in the science cell. The conductance of the tube from the cross to the cell is 2.93 L/s. The conductance of the pump arm is 13 L/s. We have a 40 L/s ion pump in this pumping arm. The net conductance is 1.85 L/s. The outgassing rate of the glass is 10^{-12} Torr L/s/cm^2. And the surface area of the cell is 56 cm^2. Hence, the estimated pressure is,

$$P = \frac{56 \times 10^{-12}}{1.85} = 3 \times 10^{-11} \text{ Torr} \tag{4.13}$$

4.3 Pumping down to ultrahigh vacuum

Since the science cell was not ready, we assembled the apparatus in two phases. In the first phase we assembled upto the gate valve, then a year later we assembled the science cell. During the construction we made sure that all the fasteners we use are 316L stainless steel to avoid any magnetization in the future.

Reaching an ultrahigh vacuum requires a thorough cleaning of the vacuum parts. We started by cleaning all the stainless steel parts in an ultrasonic bath of soap-water (alconex) solution for 10 minutes. Then, we rinsed them with deionized water. The next step of cleaning process involved ultrasonic bath of acetone, methanol and isopropanol (in that order) for 2 minutes each.

We found the hard way that glass chambers cannot be cleaned in an ultrasonic cleaner. Our first MOT cell got shattered beyond mending while cleaning in an ultrasonic cleaner.

After the vacuum chambers parts are cleaned and assembled, the first stage in pumping down is with a turbo-pump (Agilent Technology Turbo-V-301-AG). We reached a pressure of about 10^{-8} Torr with just a turbo-pump. To go below this value, we constructed a brick oven around our vacuum chamber (Figure 4.5). We used heating plates underneath the chamber to uniformly heat the oven. We slowly increased the oven temperature to 300 C over a course of the day and kept the entire system at that temperature for about 10 days. We also fired all our Ti-Sub pump filaments during the bake to clean them out. We took out the magnet from the ion-pump while the oven was hot. After over a week of bakeout and cooling down, we reached a pressure of 2×10^{-11} Torr. The pressure log during the first stage of baking is shown in Figure 4.6.

4.4 Lasers

We decided to switch to DBR lasers (PH767DBR080T8) manufactured by Photodigm from the usual homemade External Cavity Diode lasers (ECDLs) that we used in the previous generation machine. The main motivation for the switch was the stability of the DBR lasers. The linewidth for these lasers is slightly wider ($\sim$ 1 MHz) than typical ECDLs (few hundred kHz). Since the transition linewidths for potassium atoms are $\sim$ 6 MHz, we didn't expect any problems. These diodes also come with an in-built thermisor/TEC and are quite compact.

We use two DBR lasers with maximum power of 80 mW for the D2 MOT setup. One of them is locked to the absorption signal of ^{39}K crossover line (Figure 4.9) using Pound-Drevor-Hall (PDH) technique. The transition is shifted to the correct frequency of ^{40}K using AOMs. The remaining light is used for repumping. The second laser is beatnote locked to this laser with an

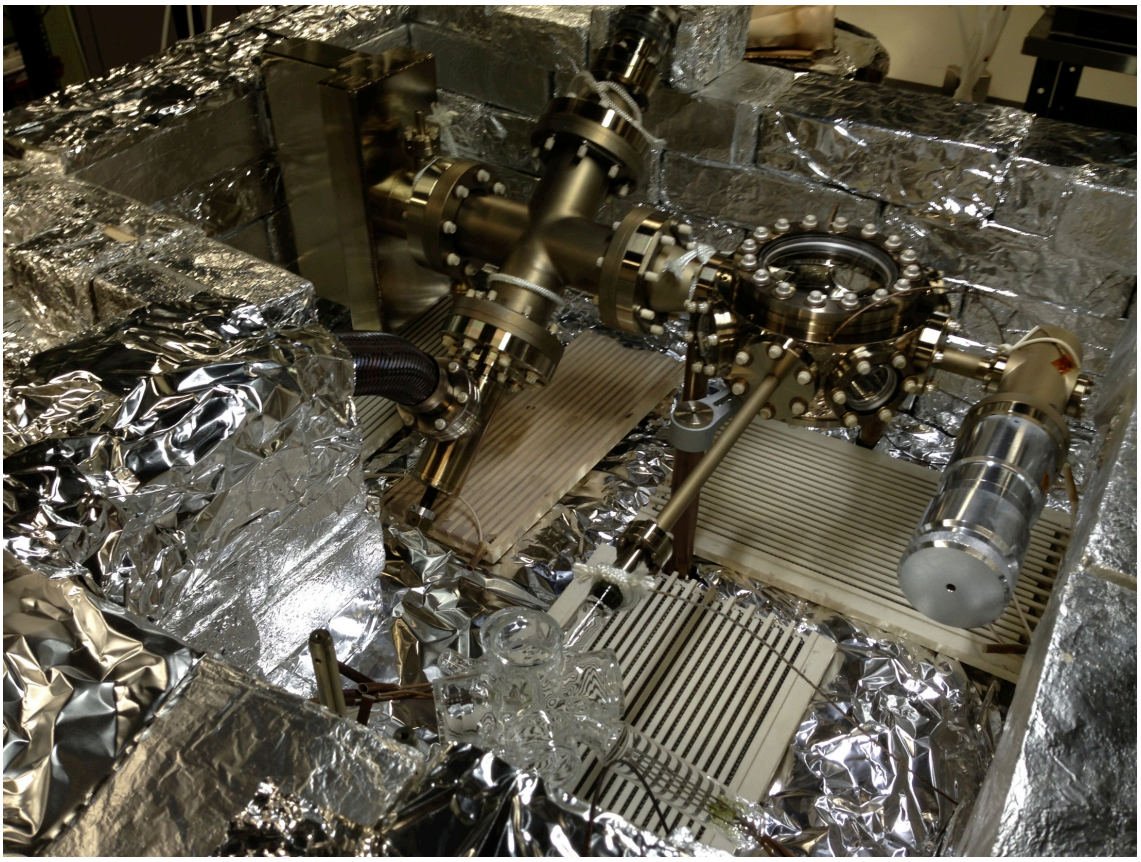

Figure 4.5: Oven construction for vacuum bakeout. Heating plates are placed underneath the apparatus. We make an oven around the chamber using bricks and cover with thermally insulating blankets.

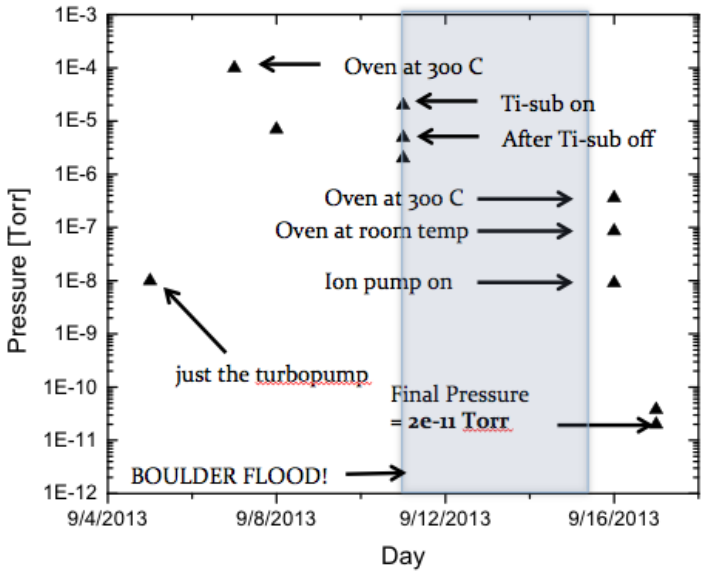

Figure 4.6: Pressure log during the first vacuum bakeout.

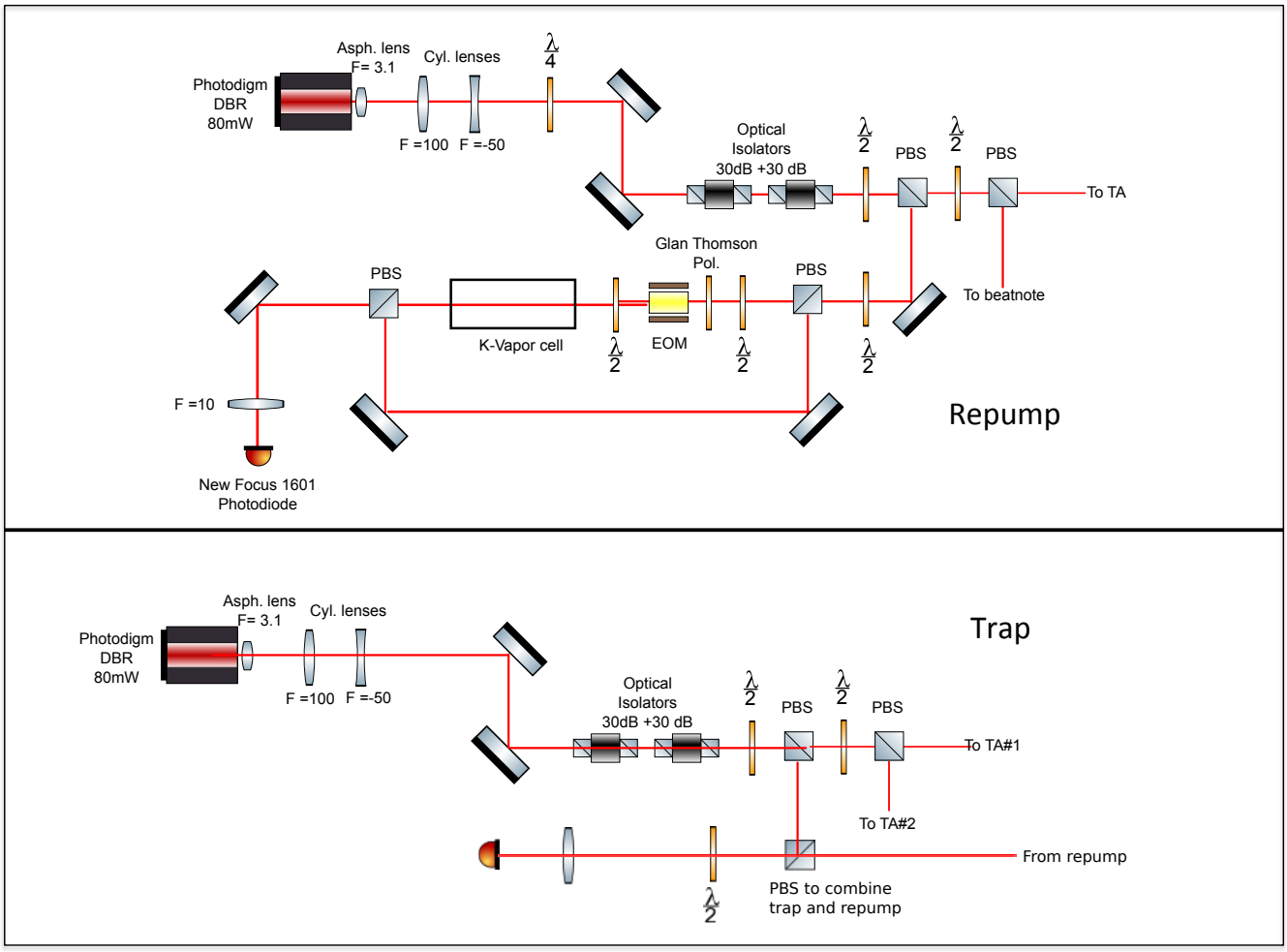

Figure 4.7: D2 Laser setup. We set up two DBR lasers for repump and trap light. The repump laser is locked to the crossover transition of ^{39}K atoms using a spectroscopy in a vapor cell. The trap laser is offset locked to the repump laser using a photodetector.

offset frequency of 666 MHz. The laser setup for trap and repump beams is shown in Figure 4.7.

Because we have two MOTs and require large intensity, 80 mW light from the DBR lasers is not enough. We use three 1.5W Tapered Amplifiers, two for trap beams and one for repump, from Eagleyard(EYP-TPA-0765-01500-3006-CMT03-0000). The setup is shown in Figure 4.8 After an appropriate frequency shifts using AOMs, we split the repump light for the first and second MOT. The first MOT repump is combined with the first MOT trap beam with a PBS and fiber coupled together. The second MOT repump is fiber coupled by itself.

The trap beam from MOT# 2 TA is split into two beams using the 0th and 1st order beam of an 80MHz AOM. The -1st order beam is used for trapping. The 0th order beam is sent to a second AOM to be used for pushing (-82 MHz), optical pumping (-62 MHz) and probing (-47 MHz). Since these processes don't occur at the same time, we use a single AOM and three D-shaped mirrors to pick-up three deflections, corresponding to each frequencies, and fiber couple the beams. Optical pumping beam is sent through a +69 MHz AOM before fiber coupling. During optical pumping and probing stages, the offset lock is shifted to get to the right frequency.

The trapping frequencies and intensities of the trap, repump, push and pump beam are listed below:

Beam	Frequency	Power
Trap MOT 1	-3Γ	120 mW
Repump MOT 1	-3Γ	40 mW
Trap MOT 2	-3Γ	120 mW
Repump MOT 2	-3Γ	10 mW
Push	-3Γ	15 mW
Pump	+3Γ	100 uW

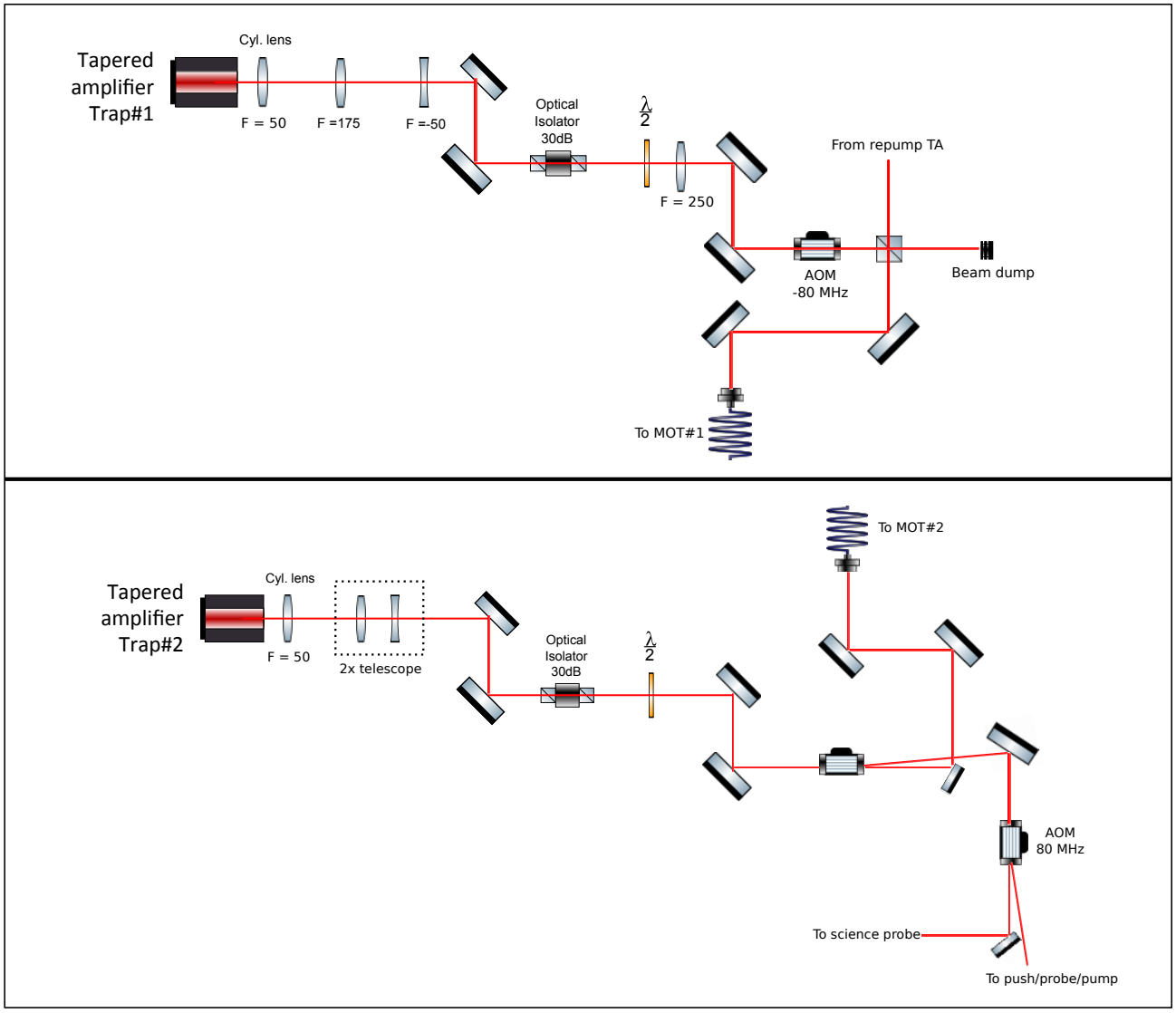

Figure 4.8: Tapered Amplifier setup.

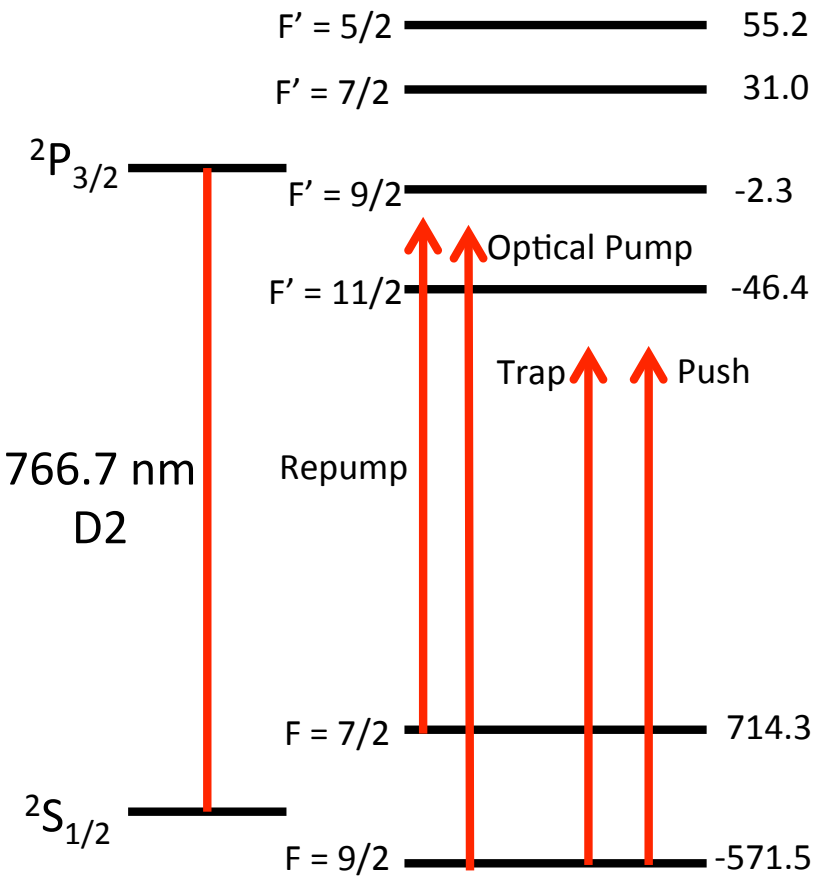

Figure 4.9: ^{40}K D2 transition lines. The frequencies on the right side are in MHz.

4.5 Cart

We transfer atoms from the second MOT chamber to the science cell, using a pair of quadrupole coils which are mounted on a linear stage (cart). The atoms travel a distance of 20.87" (53 cm) from the center of the second MOT chamber to the center of the science cell. The quadrupole coils have 30 turns each and are wound with copper square hollow tubings which allow us to water cool these coils. They serve the purpose of providing quadrupole confinement during MOT stage and the transfer stage.

The coils are mounted on a custom made Parker XR-404 with 700mm of travel. We use Parker BE233GL-NPSN servo motor and GV6K-U6E servo controller. The motion of the linear stage is programmed on a Motion Control software also provided by Parker. We have seen in some JILA labs that this servo/motor can be noisy because they use switching power supply, so they had to use an Aerotech motor. This is not a problem for us.

4.6 Magnetic Trap Description

After discussing various magnetic trap designs, we decided to build a QUadrupole Ioffe Configuration (QUIC) trap around the science cell. Ioffe-Pritchard traps are quite common in JILA, but they have a poor optical access. Plugged quadrupole trap would have been another option, but they require a separate blue-detuned laser and are also quite sensitive to pointing stability. Hence a QUIC trap is an attractive option as it is relatively simple to design design, provides a large optical access and is "quick" to build.

The QUIC trap primarily consists of three coils: a pair of quadrupole coils and a Ioffe coil (Figure 4.10). The Ioffe coil shifts the zero of the magnetic field from the quadrupole pair, thus atoms avoid undergoing Majorana spin-flips. However, because the Ioffe coil also breaks the axial symmetry, the field profile is not symmetric. The field minima is shifted in the direction of the Ioffe coil (Figure 4.11.

We use the quadrupole coils of the QUIC trap as a bias-coil-pair for Feshbach field. Hence,

the quadrupole trap includes an H-bridge circuit. The electronics of the switches is shown in Figure 4.13.

The coils are wound with a square hollow copper tubing, which are good for water cooling. The quadrupole coil pairs have 4x4 turns and have the inner diameter 3.75 in and the outer diameter of 5.12 in. The coils are separated by 1.53 in (inner separation). The Ioffe coil has 4x2 turns and has an inner diameter of 0.72 in and an outer diameter of 1.36 in. The coil is placed 1.18 in from the quadrupole coils center.

With the measured coil resistitivity of 1.88 mOhms/m, we expect the power dissipation on the coils is about 2900 W at the current required for the QUIC trap. Hence, we use JILA-chilled water to cool these coils.

An important part of the magnetic trap design is the field stability. To maintain a 3 mG trap-bottom stability, we need 30 ppm current stability in the Ioffe-coil. We use the circuit shown in Figure 4.12 to stabilize the current in these coils.

4.7 Electronics for the magnetic trap

We use two Keysight 6690A power supplies (15V, 440A) to drive cart coils and the QUIC trap. The cart coils and the Ioffe coil are connected to one power supply and the science quadrupole trap is connected to the other power supply. To switch between cart coils and Ioffe coils, we use a mechanical relay switch from Kissling(29.511.11). These switches can handle up to 500A of current and have a switching time of $\sim$ 60 ms. We also use four of these switches to make an H-bridge to switch between quadrupole and Feshbach configuration (Figure 4.13.

The QUIC trap needs to be stable to about 10 ppm in current noise to avoid heating or losses during the evaporation stage. We use analog servo electronics to maintain the current stability. The electronics are home-built and an improved version of the one designed by Brian DeMarco. We use an IGBT (SKM400GA12V) to regulate the current and Danfysik IT 700-S as a current sensor.

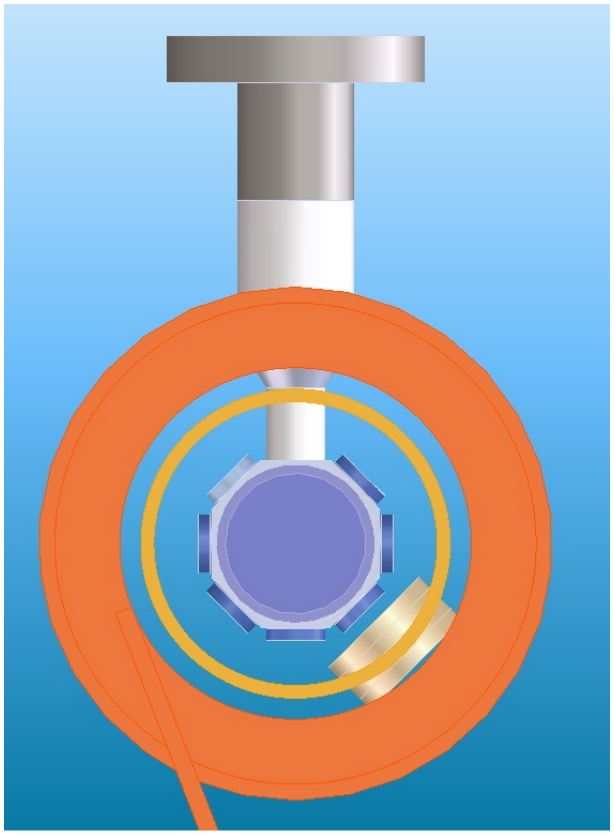

Figure 4.10: The top view of the QUIC trap. The quadrupole pair (orange), the fast-B coil (yellow), Ioffe (light yellow) are visible.

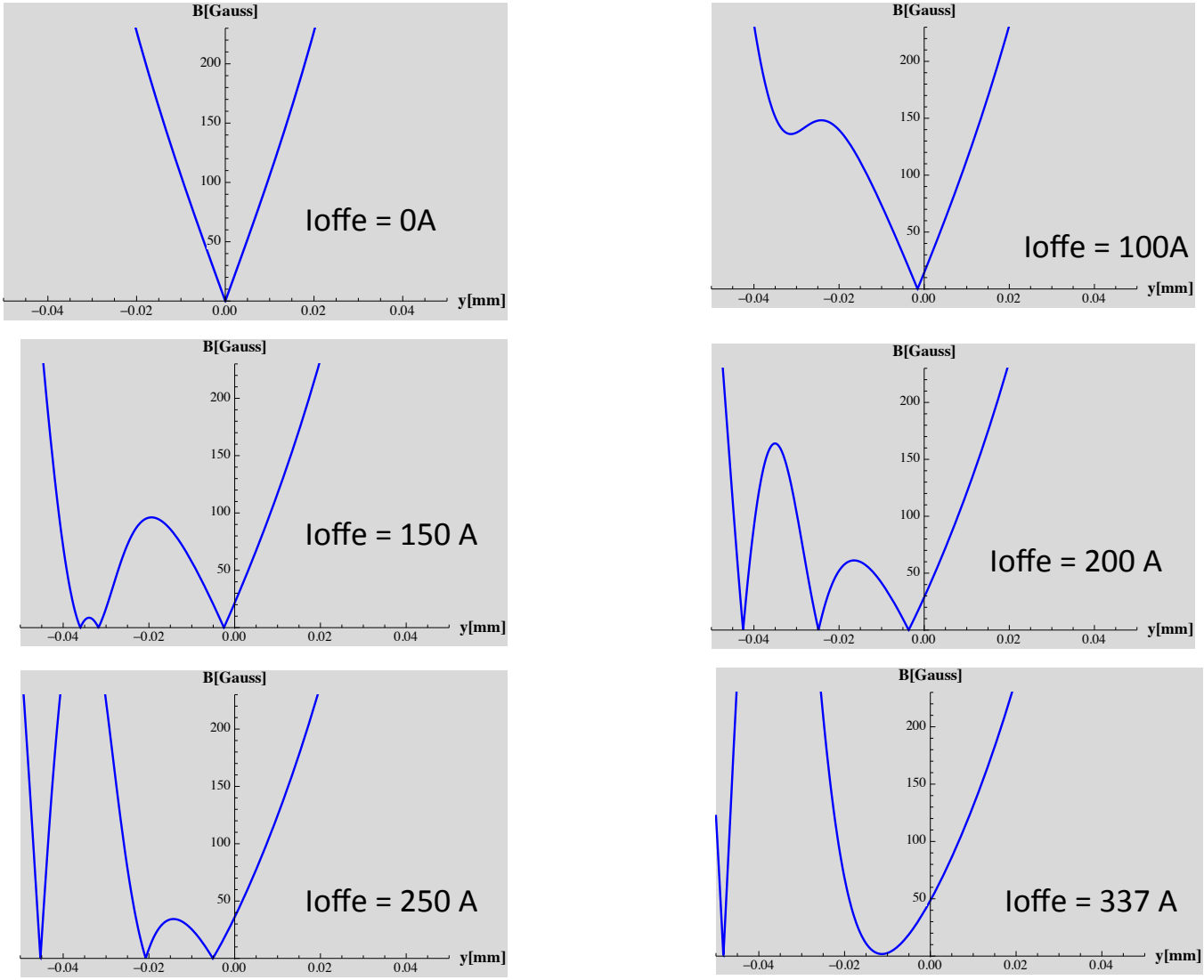

Figure 4.11: B-field profile along the direction of Ioffe-coil while increasing the Ioffe coil current. Quadrupole current = 380 A.

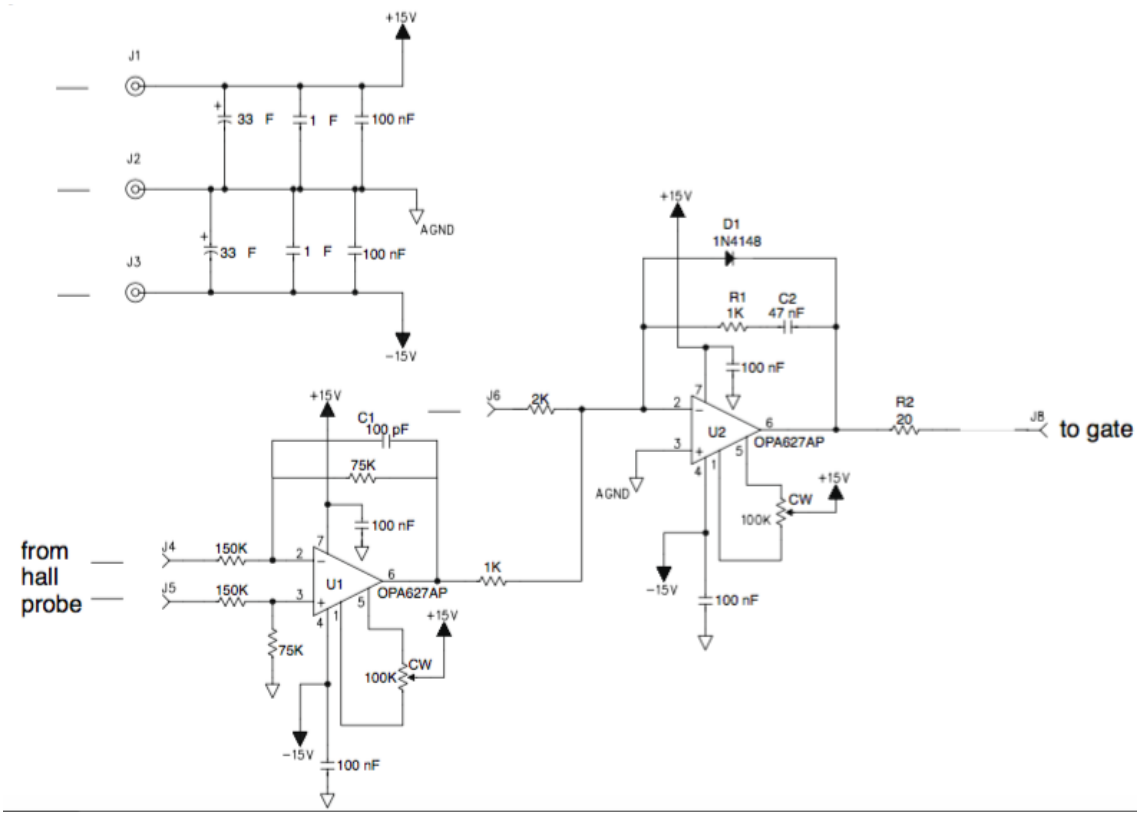

Figure 4.12: Current Servo electronics. This servo is used to control the gate voltage of MOSFETs/IGBTs for MOT coils, shim coils, quadrupole coils and the Ioffe coil.

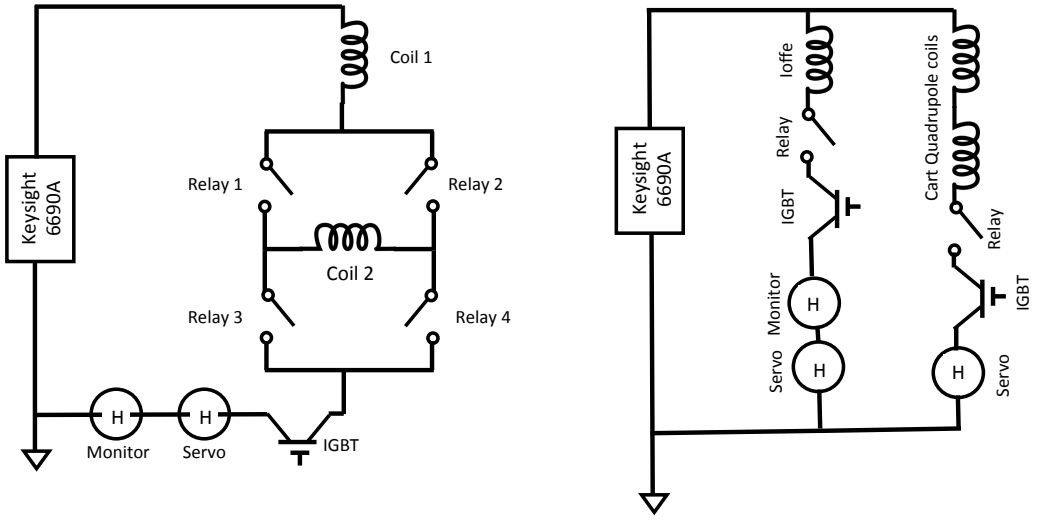

Figure 4.13: Circuit diagram for cart quadrupole trap and QUIC trap. Left: H-bridge setup to switch between science quadrupole trap and Feshbach coils. Right: Switching circuit between the Ioffe coil and the cart quadrupole coil. The element H are the Danfysik IT 700-S, used for in-loop and out-of-loop current sensors for servoing and monitoring purpose respectively. Relays are the Kissling (29.511.11) switches. IGBTs used in these circuits are SKM400GA12V.

4.8 Dipole Trap

The accessible Feshbach resonances in ^{40}K are in the negative Zeeman levels, which are high field seeking. Hence, we load the atoms at the end of magnetic trap evaporation to a far-off-resonant dipole trap (FORT). We use an IPG 10W multimode fiber laser (IPG YLR-10-1075-LP) at 1075 nm for this purpose. We split the beam into two arms and fiber couple them to make a crossed dipole trap. The two arms the beam have orthogonal polarization to avoid potential issue with fluctuating interferences. The schematic of the setup is show in Figure 4.15. The horizontal beam has a beam waist of 25 μm and the vertical beam has a beam waist of 150 μm. The trapping potential in the horizontal direction is given by,

$$U_{\text{dipole}}(x,y,z) = \frac{3\pi c^2 \Gamma}{2\omega_0}\left(\frac{1}{\omega-\omega_0}+\frac{1}{\omega+\omega_0}\right)\left(I_{\text{horizontal}}(x,y,z)+I_{\text{vertical}}(x,y,z)\right) \tag{4.14}$$

$$+mgy, \tag{4.15}$$

where Γ is the excited state linewidth of the $P_{3/2}$ level, ω_0 is the resonant D2-line frequency, ω is the frequency of the dipole trap laser, and $I_{\text{horizontal}}(x,y,z)$ and $I_{\text{vertical}}(x,y,z)$ are the intensity of horizontal and vertical beams respectively. The last term in the equation is potential due to gravity, which becomes important when the trap depth is lowered.

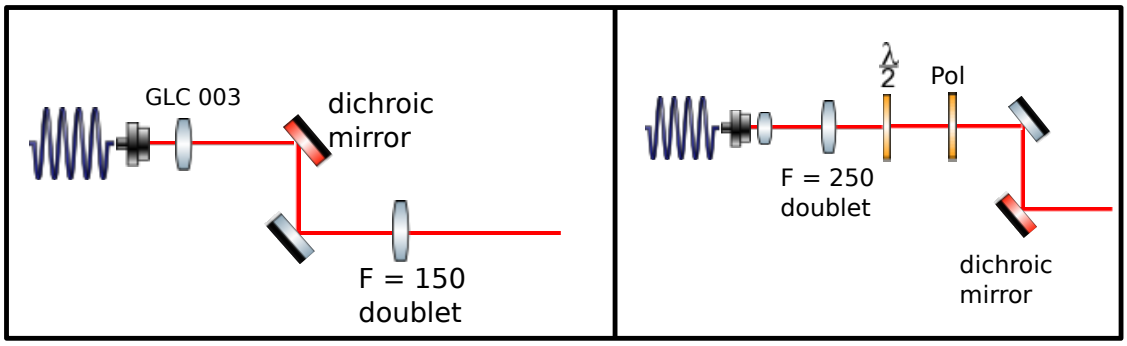

Figure 4.14: Dipole trap setup. Left: Setup for horizontal dipole trap to produce 25 μm beam waist. Right: Setup for vertical dipole trap to produce 150 μm beam waist.

4.9 Computer Control and Data Acquisition

We use two Xilinx FPGA cards to control the experiment. Each of these cards provide 48 digital channels and 8 analog channels. The card is programmed in LabView. The front-end computer control interface is written in MATLAB to be more user friendly.. The sequence is sent as 64-bit information from MATLAB to LabView using TCP/IP communication. This enables the control of the experiment from any computer. Since 16 analog channels are not enough for us, we use two 16-bit 8-channel analog cards (EVAL-AD5360) from Analog Devices. These cards are programmed using 6 digital channels from the FPGA.

In MATLAB, channel numbering starts at 0. Analog channels from FPGA1 are labelled as 100 for AO0, 101 for AO1 etc. and those from FPGA2 are labelled 200 for AO0, 201 for AO1 etc. Digital lines are labelled similarly– 100 for DO0, 101 for DO1 and so on.

All the timings are in seconds and analog voltages are in volts. For digital channels, 0 or OFF is logical low and 1 or ON is logical high. We use an optical isolator board between the FPGA digital lines and the instruments. This helps to prevent potential ground loops and accidental frying of the FPGA board.

Commands that can be used in MATLAB are as follows:

- Aout(channel, time, value) - set the value of an analog channel at the given time
- Aout_ramp(channel, time, ramp duration, start value, end value) - ramp an analog channel from start value to end value at the given time during the ramp duration
- Dout(channel, time, value) - set the value (ON/OFF) of a digital line
- Dout_pulse(channel, time, pulse duration) - generate a pulse in a digital channel
- GPIBout(time, address, command) - send a command to the GPIB address.

An example code to switch the relay from Cart configuration to Ioffe configuration is shown below. This set of codes also sets the voltage and current limit on the power supply.

```
GPIBout(1, 5, 'VOLT 14') % GPIB channel 5 at 1 second
GPIBout(1, 5, 'CURR 440')% GPIB channel 5 at 1 second
Dout(cart_or_ioffe_voltage_multiplexer, ti_coils, OFF) %multiplexer
Dout(cart_relay_switch, ti_coils, ON) %relay
Aout_ramp(cart_coil_servo_control, ti_coils, 100*ms, 0, -1) %current
Aout_ramp(cart_coil_servo_control, 5, 100*ms, -1, 0) %current
```

We use a PixelFly camera and a Princeton Instrument (PI) ProEM CCD camera to acquire images of the atoms. The PixelFly camera is used to image atoms in the second MOT. Princeton Instrument camera is used to acquire images of atoms in the science cell. Even though an EM CCD is an overkill, we found out recently that this is the only camera currently available from PI that has kinetics mode imaging.

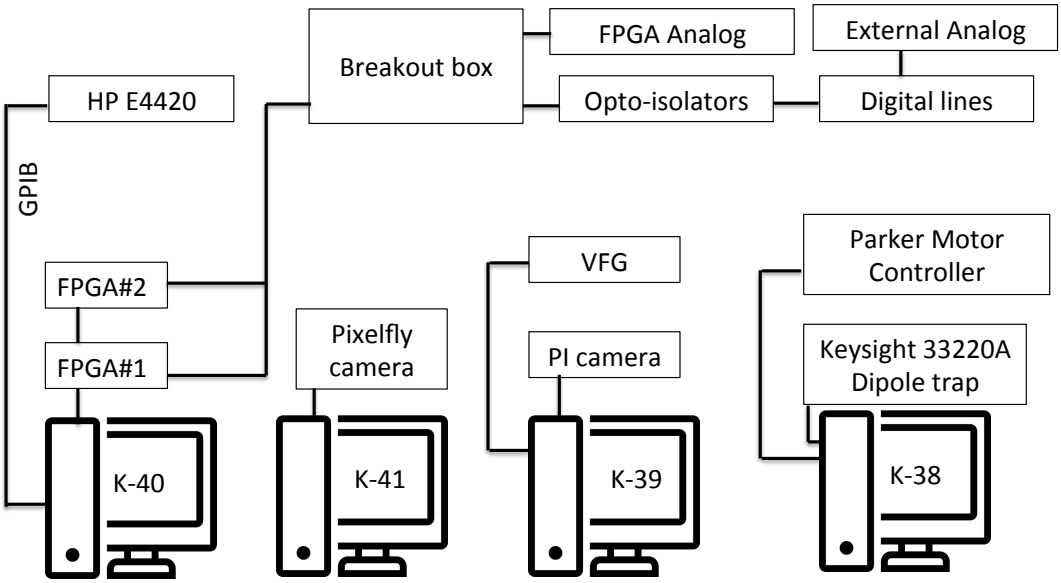

Figure 4.15: Layout of the computer control. We use one main computer for FPGA and GPIB control. Three other workstations are used to acquire data from PixelFly/Princeton Instrument cameras, and to send commands to Versatile Frequency Generator (VFG), Parker Motor and dipole trap waveform. The computers are named after potassium isotopes.

Chapter 5

Cooling to degeneracy

Cooling of the atoms down to degeneracy begins in the dispenser MOT cell. Here, atoms from potassium vapor are trapped in a magneto-optical trap (MOT) and cooled to the Doppler limited temperature. We collect about 10^8 atoms in the first MOT. Since the vacuum lifetime in this chamber is only around one second, we push the atoms to the second chamber, which a better lifetime. Better vacuum lifetime and use of the dark-SPOT repump allow us to trap 5×10^8 atoms in the second MOT. Atoms are further cooled below the sub-Doppler limit using gray molasses cooling technique. At this stage, they are optically pumped into the correct Zeeman level and loaded into a purely magnetic quadrupole trap. The atoms are transferred to the science cell using a translation stage with a unity efficiency. Then, they are loaded to the stationary quadrupole trap. Ioffe coil is adiabatically ramped on to create a harmonic potential. We use a microwave transition ($|F = 9/2\rangle \rightarrow |F = 7/2\rangle$) to evaporate hotter atoms out of the trap. About 2×10^7 atoms are cooled to about $20\mu K$ in this trap. They are then transferred to an optical dipole trap where further evaporation down to degeneracy occurs. We get about 10^5 atoms at $T/T_F = 0.2$ at the end of optical trap evaporation. By putting them in the right Zeeman states, we can access the Feshbach resonance near 202 Gauss to create a strongly interacting ultracold Fermi gas.

5.1 MOT Basics

The first stage of cooling starts with a magneto-optical trap (MOT). Magneto-optical trap works in the principle of Doppler cooling and an inhomogeneous magnetic field [60]. The basic

principle of optical pumping in a MOT is shown in Figure 5.1. The atoms in a quadrupole magnetic field experience a position dependent Zeeman shift in the excited state. When we introduce two counter-propagating circularly polarized red-detuned beams on the atoms, they scatter photons depending upon their position and are driven towards the center of the trap where the magnetic field is zero [60].

For a small Zeeman shift compared to the detuning (δ), the force on the atoms with velocity $\vec{v}$ and displacement ($\vec{r}$) is given by [60],

$$\vec{F} = -\beta\vec{v} - \kappa\vec{r}, \tag{5.1}$$

where $\beta = (8\hbar k^2 \delta s_0)/(\Gamma(1 + s_0 + (2\delta/\Gamma)^2)^2)$, and $\kappa = (\mu B')/(\hbar k)\beta$. Here, $\hbar k$ is the momentum of the photons, s_0 is the I/I_{sat}, Γ is the transition linewidth, μ is the magnetic moment, and B' is the magnetic field gradient. For a typical MOT parameter of the field gradient of ~ 10 G/cm and detuning of a few Γ, the oscillation frequency is a few kHz and the damping rate is a few hundred kHz, making it an over damped system.

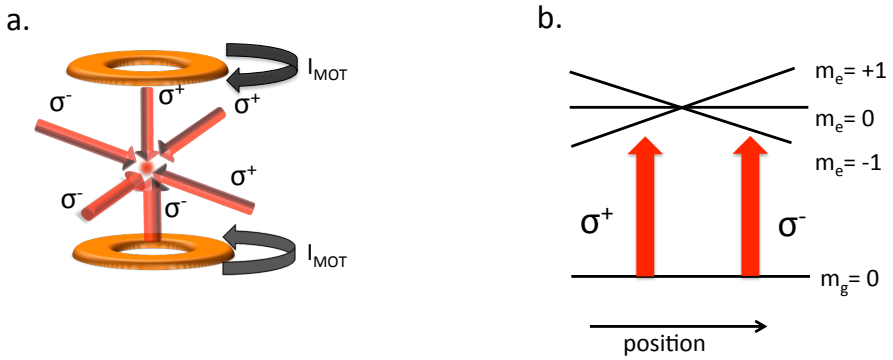

Figure 5.1: a. A sketch of a magneto-optical trap (MOT) setup. Three orthogonal beams are passed through the chamber and are retro-reflected in combination with quarter wave plates to form a $\sigma^+ - \sigma^-$ setup. We run current in opposite direction in the two coils to form a quadrupole magnetic field. b. The basic energy level diagram for a simple MOT transition, which shows shift in energy level as a function of position.

The cooling limit in a MOT depends on the atomic transition linewidth, and is given by,

$$T_{\text{Doppler}} = \frac{\hbar\Gamma}{2k_B}. \tag{5.2}$$

The natural linewidth of the D2 transition in ^{40}K is $2\pi \times 6$ MHz, hence the Doppler temperature limit in the MOT is 144 μK.

5.2 First MOT

The collection MOT is formed with three retroreflected beams. The MOT beams consist of 120 mW of trap and 40 mW of repump power coming out of a single mode fiber. The light is split into three beams and sent through the three orthogonal windows of the collection MOT cell with appropriate polarizations. The beams have a Gaussian waist of 1.4 cm. The quadrupole magnetic field in for trapping is produced by a pair of coils with 110 turns run in quadrupole configuration at 3A.

We collect potassium vapor from following reaction which occurs at around 400 C:

$$2\mathrm{KCl} + \mathrm{Ca} \rightarrow 2\mathrm{K} + \mathrm{CaCl}_2. \tag{5.3}$$

To avoid any deposition of potassium in the collection cell windows, we use heating tapes around each windows to heat the cell at 70 C. When we did not use the heating tapes, we noticed formation of silver potassium layers on MOT windows that affected beam transmission.

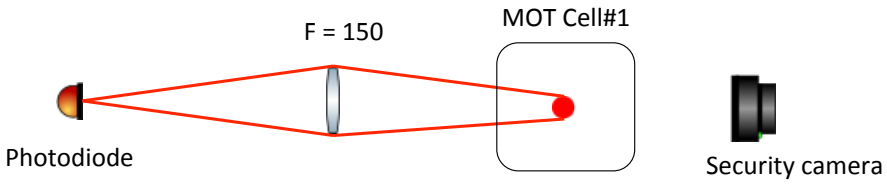

Figure 5.2: Fluorescence measurement of the first MOT. A $2f \rightarrow 2f$ imaging system is setup to collect the fluorescence of the first MOT. By knowing the solid angle of the lens subtained on the atoms, and intensity and detuning of the MOT beams, we can calculate the number of atoms collected in the MOT. There's also a security camera, which is sensitive to near IR light, to view the MOT for troubleshooting purpose.

MOT fluorescence is observed through the half-inch windows. We setup a security camera(for good sensitivity in the IR regime) on one side and a photodiode with one lens to focus the MOT fluorescence on the second side.

The yield of potassium and the fill tau as a function of current is shown in Figure 5.3. We noticed that with a fill time of 1.2 s, 3.8 A is ideal for us. We started to see potassium deposits above 4A.

We scanned the frequency of the trap laser to optimize the filling rate of the MOT. Figure 5.4 shows the results of the scan.

5.2.1 Calculating MOT Number from fluorescence

We setup a single lens imaging system to collect the fluorescence onto a photodiode. The number of atoms in the MOT is given by,

$$\mathrm{N_{atoms}} = \frac{V_{PD}}{\text{gain} \times \text{QE} \times \text{solid angle} \times \hbar\omega \times p_{\text{excited}}/\tau}, \tag{5.4}$$

where gain and QE are the photodiode specifications, solid angle is the measured quantity of the imaging setup, ω is the frequency that corresponds to the 767 nm light, $\mathrm{p_{excited}}$ is the excited state population and τ is the lifetime of the excited state. The excited-state population is given by,

$$p_{\text{excited}} = \frac{I/I_{\text{sat}}}{1 + I/I_{\text{sat}} + 2(\Delta/\Gamma)^2}, \tag{5.5}$$

where I is the intensity of the trap beam, $I_{\text{sat}} = 2.2$ mW/cm^2 and Δ is the trap detuning. Using this model, we typically get the atom number in the first MOT to be around 3×10^7. However, this simple model is not entirely correct. In the next section, I will discuss the more accurate six-level model to get the excite-state fraction.

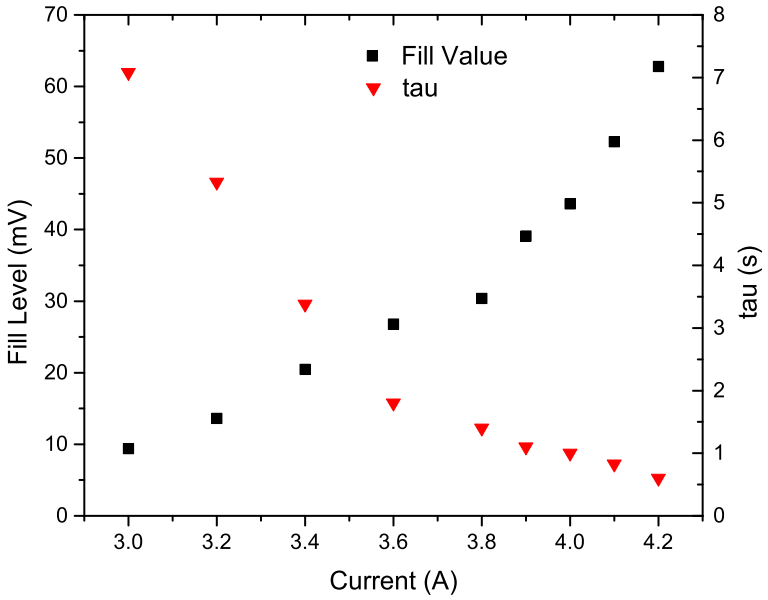

Figure 5.3: Potassium yield vs dispenser current. We raised the dispenser current and waited for a few hours to measure the fill level and the half fill time. The measurement is taken with a photodiode.

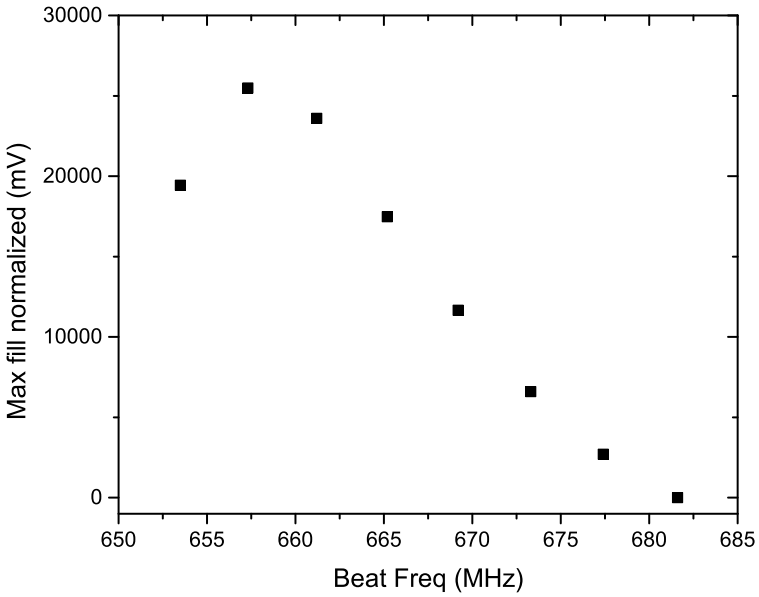

Figure 5.4: MOT fill level vs beat frequency. The y-axis is normalized such that it is proportional to the atom number. The resonance is at 682 MHz.

5.2.2 Six-level MOT

A simple two-level model is not a good model to account for the number of atoms in a ^{40}K MOT because of the complicated energy levels. To get a more precise number, we need to consider the full six-level model which correspond to: $F = 9/2 \rightarrow F' = 11/2, F' = 9/2$ and $F' = 7/2$ and $F = 7/2 \rightarrow F' = 9/2, F' = 7/2$ and $F' = 5/2$ and find the total scattering rate.

From Ref. [60], we have $I_{\text{sat}} = 1.75$ mW/cm^2. Using the branching ratios from ref [61], averaging over polarization (or Zeeman states) gives a factor of 2.5, or $I_{\text{sat}} = 4.4$ mW/cm^2. To find the scattering rate, we first need to find the transition strength and the branching ratio of ground states and excited states respectively. The transition strength is proportional to the square of the matrix element μ_{eg} and is given by,

$$D = \left[\sqrt{(2J+1)(2J'+1)(2F+1)(2F'+1)} \begin{Bmatrix} L' & J' & S \\ J & L & 1 \end{Bmatrix} \begin{Bmatrix} J' & F' & I \\ F & J & 1 \end{Bmatrix} \begin{pmatrix} F & 1 & F' \\ m_F & q & -m'_F \end{pmatrix} \right]^2 \quad (5.6)$$

where the curly brackets denote the Wigner-6j symbols, the parenthesis denotes the Wigner-3j symbol, and $q = \pm 1$ for sigma transitions, q = 0 for π-transitions. For the D2 transition in ^{40}K, the ground state has S =1/2, L=0 and J= 1/2, and excited states has S = 1/2, L = 1, J = 3/2, and I= 4 for both ground and excited states. The matrix c gives the transition strength from F=$\{9/2, 7/2\}$ to $F' = \{11/2, 9/2, 7/2, 5/2\}$ relative to the total transition strength for that F (columns sum to 1). The matrix b gives the transition strength from $F = \{9/2, 7/2\}$ to $F' = \{11/2, 9/2, 7/2, 5/2\}$ relative to the total transition strength for that F' (rows sum to 1).

$$c = \begin{pmatrix} 0.6 & 0 \\ 0.296 & 0.255 \\ 0.104 & 0.37 \\ 0 & 0.375 \end{pmatrix}, b = \begin{pmatrix} 1 & 0 \\ 0.592 & 0.408 \\ 0.295 & 0.741 \\ 0 & 1 \end{pmatrix}$$

The rate equation can derived as follows:

$$\frac{dp_F}{\mathrm{dt}} = R_{F1}(p_1 - p_F) + R_{F2}(p_2 - p_F) - \Gamma p_F \tag{5.7}$$

$$\frac{\mathrm{dp_1}}{\mathrm{dt}} = \sum_{F=\frac{5}{2}}^{\frac{11}{2}} R_{F1}(p_F - p_1) + bF_1\Gamma p_F \tag{5.8}$$

$$\frac{\mathrm{dp_2}}{\mathrm{dt}} = \sum_{F=\frac{5}{2}}^{\frac{11}{2}} R_{F2}(p_F - p_2) + bF_2\Gamma p_F, \tag{5.9}$$

where p_F is the population in the excited state F, $\mathrm{p_1}$ and $\mathrm{p_2}$ are the populations in the ground states, and R_{Ff} is the transition rate from f to F.

$$R_{Ff} = \frac{c_{Ff}\Gamma}{2}\left(\frac{I_\mathrm{f}/I_{\mathrm{sat,Ff}}}{1 + I_\mathrm{f}/I_{\mathrm{sat,Ff}} + 4(\Delta_{Ff}/\Gamma)^2}\right), \tag{5.10}$$

where $I_\mathrm{sat} = I_\mathrm{sat}/c_\mathrm{Ff}$.

In the steady state, we set $\frac{dp_F}{\mathrm{dt}} = 0$ and $\frac{dp_f}{\mathrm{dt}} = 0$. Hence, we get,

$$p_F = \frac{p_1 R_{F1} + p_2 R_{F2}}{R_{F1} + R_{F2} + \Gamma} \tag{5.11}$$

$$p_1 = \frac{\sum_{F=\frac{5}{2}}^{\frac{11}{2}} p_F(R_{F1} + b_{F1}\Gamma)}{\sum_{F=\frac{5}{2}}^{\frac{11}{2}} R_{F1}} \tag{5.12}$$

$$p_2 = \frac{\sum_{F=\frac{5}{2}}^{\frac{11}{2}} p_F(R_{F2} + b_{F2}\Gamma)}{\sum_{F=\frac{5}{2}}^{\frac{11}{2}} R_{F2}}. \tag{5.13}$$

We can substitute Equation for p_F into Equation for p_2. Then, we can solve for p_2 in terms of p_1.

$$p_2 = \frac{\sum_{F=\frac{5}{2}}^{\frac{11}{2}} \frac{R_{F2}+b_{F2}\Gamma}{R_{F1}+R_{F2}+\Gamma}}{\sum_{F=\frac{5}{2}}^{\frac{11}{2}} \frac{R_{F1}+b_{F1}\Gamma}{R_{F1}+R_{F2}+\Gamma}} p_1. \tag{5.14}$$

We can then set p_1 to 1 and calculate p_2. Finally, we can calculate all p_Fs. Then, the excited state population is given by,

$$p_e = \frac{\sum_F p_F}{1 + p_2 + \sum_F p_F}. \tag{5.15}$$

For the values of detuning and intensities we use in our MOT, the two-level model gives a factor of 4 less number than the six-level model. We have verified that the six-level model is consistent with number extracted from absorption images.

5.3 Push to the second MOT

Atoms cooled in the first MOT are transferred to the second chamber with a near resonant beam ($|F = 9/2\rangle \rightarrow |F' = 11/2\rangle$). The atoms collected in the first MOT are pushed in the direction of the second chamber. Once the atoms start to move out of the first MOT, they are off-resonant with the push beam. Hence, they don't get subsequent momentum kicks. We use a continuous beam to push the atoms to the second chamber. We found out that the pulsed and the continuous beam have a similar efficiency of transfer. We, however, noticed that the loading of the second MOT is quite sensitive to the position of the push beam. If the push beam is near the atoms in second MOT, it kills the second MOT instantly. Hence, we used two mirrors to walk the beam: first mirror to efficiently push the atoms from the first MOT and the second mirror to miss the second MOT.

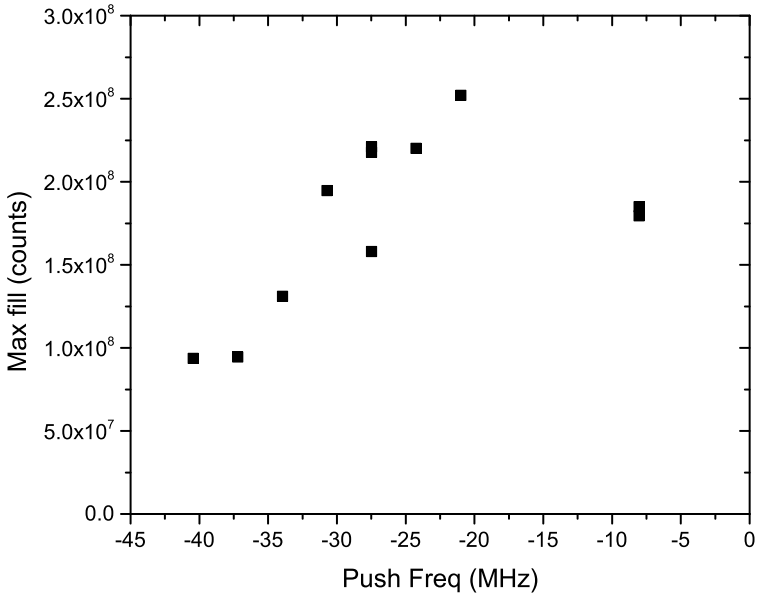

Figure 5.5: MOT fill level vs push frequency detuning.

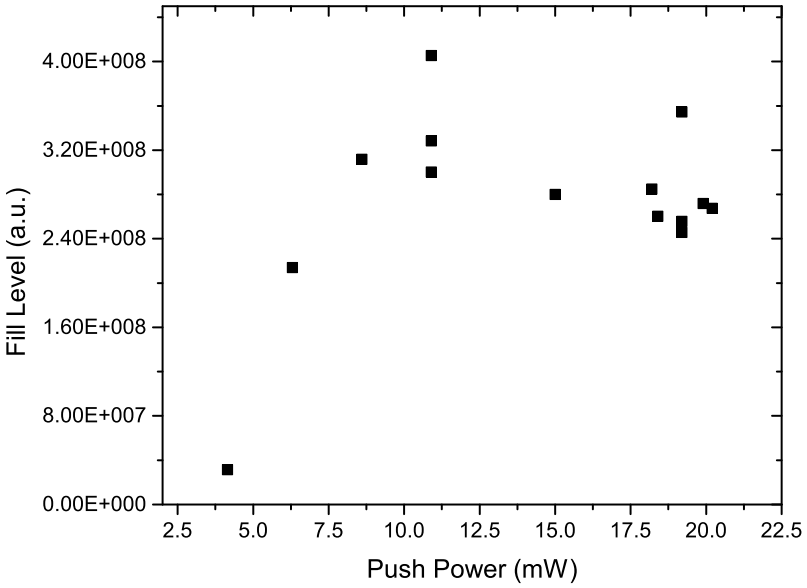

Figure 5.6: MOT fill level vs push beam power.

5.4 Second MOT

Atoms pushed to the second chamber are collected in another MOT formed by three retro-reflected beams. The beams have a Gaussian waist of 1.4 cm. The gradient of 10 Gauss/cm for the MOT is formed by water cooled coils, which also form the quadrupole trap in the subsequent stage. The schematic of the trap, bright/dark repump and the D1 cooling beams are shown in Figure 5.7. We use a dark-SPOT repump for this MOT in order to avoid density dependent losses. We load the MOT for 60 s and collect 10^9 atoms. We have noticed that the dark-SPOT repump improves the number by 10 folds but the loading τ is increased by a factor of 4.

5.4.1 Lifetime

A good vacuum lifetime is desirable for an efficient cooling of atoms in a magnetic trap or an optical dipole trap. For the second chamber we can measure the lifetime of atoms in two ways. The first way is to fully load the atoms into the MOT and then turn off the push beam. We can then monitor the decaying fluorescence signal of the MOT and fit it to an exponential to find the lifetime. Using a bright repump beam, as opposed to a dark-SPOT repump, we observed two different timescales as shown in Figure 5.9. The first lifetime corresponds to the fast decay due to high density of the MOT. The second, longer, timescale comes from the loss due to collisions with background atoms.

The second way to measure the lifetime of the atoms is to load the atoms into a magnetic trap after optical pumping to the right spin states. Then, hold the atoms in the trap for variable amount of time. At the end of the hold, either do an absorption imaging or load them to the MOT followed by a recapture measurement. We found that the lifetime measured this way in the second chamber is around 40s (Figure 5.10), which is shorter than measured using MOT fluorescence. This is because the atoms in a magnetic trap are more sensitive to spin flips and losses due to the scattered light.

We also measured the lifetime in a QUIC trap in the science chamber by doing absorption

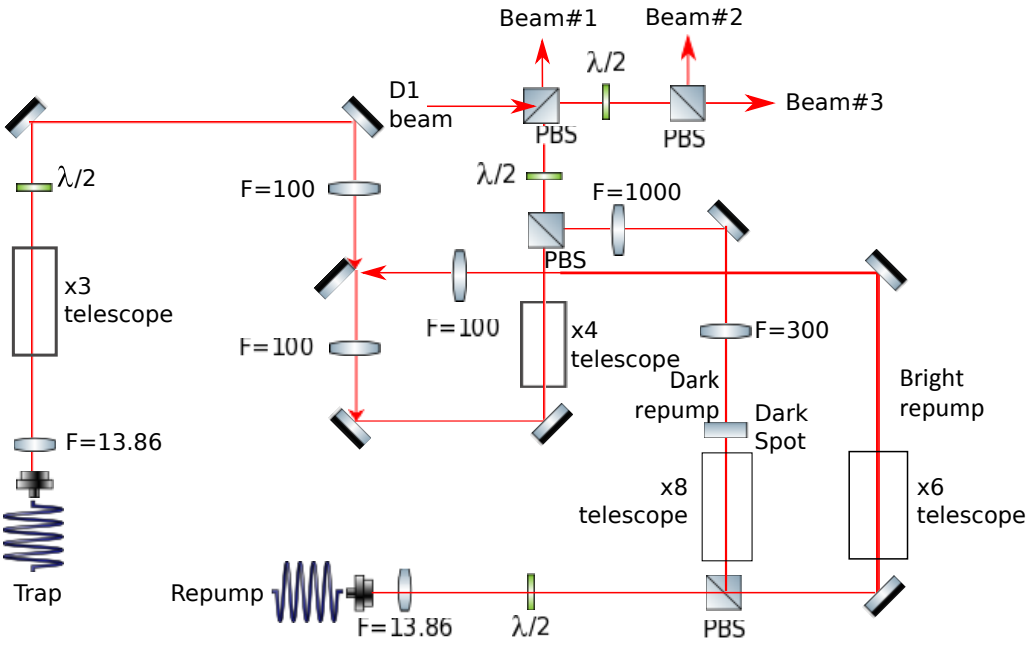

Figure 5.7: Schematic of the second MOT beams. The dark-repump is formed by imaging a 1.6 mm aluminum dot on to the atoms by using F = 300 mm and F = 1000 mm lens setup as seen in the figure above. The bright repump is turned on only during optical pumping stage. D1 beam consists of both trap and repump light out of the fiber.

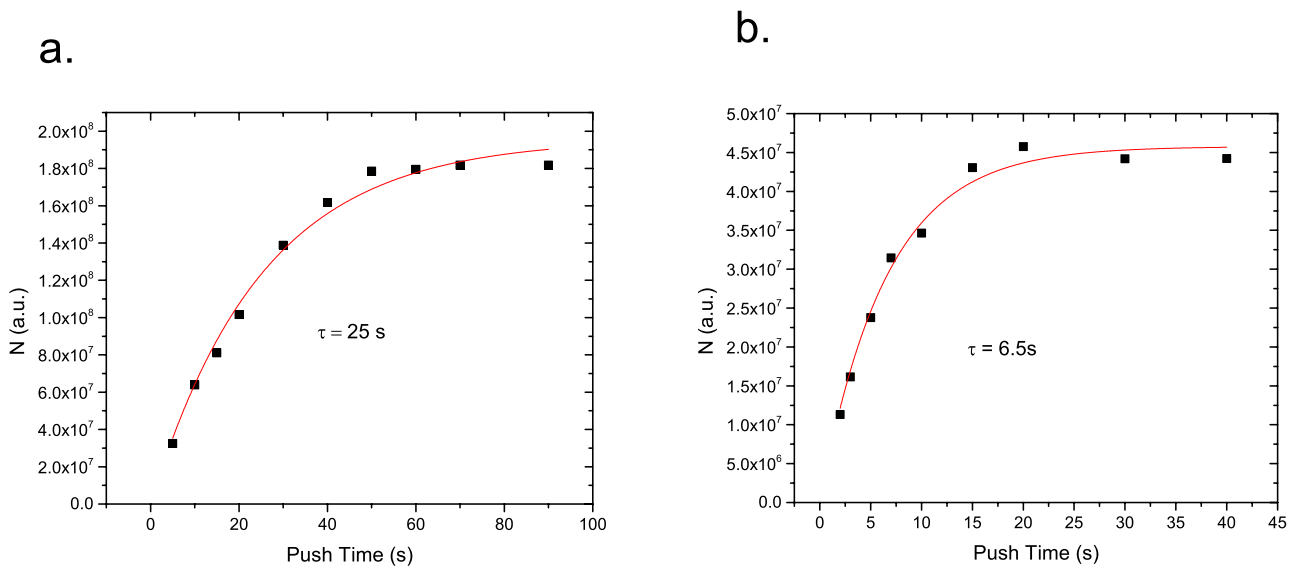

Figure 5.8: MOT fill level vs push time. a. with dark SPOT repump b. without dark SPOT repump. We notice a significant increase in atom number with the dark SPOT repump beams.

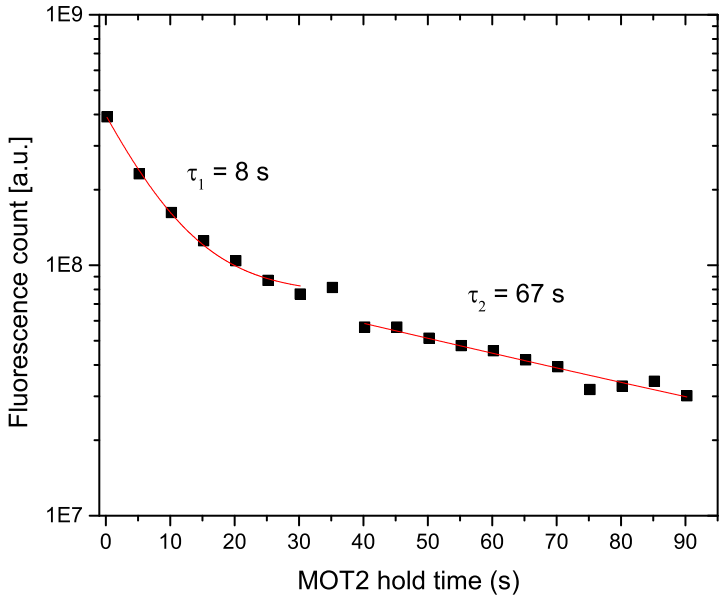

Figure 5.9: Lifetime of atoms in the second MOT. We load the atoms to the MOT and turn off the push beam and wait. We see a two clear timescales, a fast timescale of about 8s corresponding to density dependent losses and a slower timescale corresponding to background losses

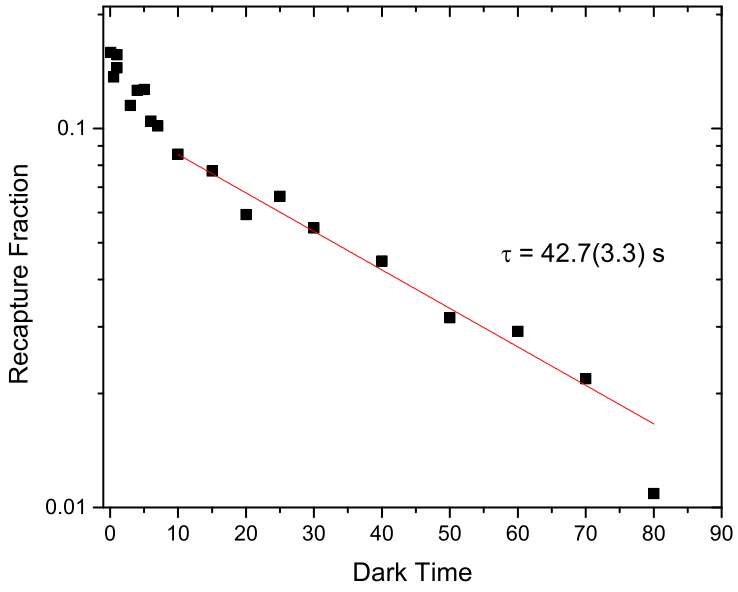

Figure 5.10: Lifetime of atoms in the quadrupole trap in the second MOT chamber. We load the atoms into a quadrupole trap and wait there for a certain time(dark time), then reload the atom to a MOT and measure the recapture fraction. This lifetime is less than the MOT lifetime because atoms are more sensitive to losses due to scattered light in a quadrupole trap. Also, the magnetic trap is more shallow, thus vulnerable to grazing collisions with background gas.

imaging. We found out that the lifetime in the science cell is around 80 s. This is long enough to do evaporation in the magnetic and dipole trap.

5.5 Gray Molasses cooling

Doppler temperature, which is 145 μK for ^{40}K, is the limit to cool atoms in the MOT. Several techniques have been tried to reach below this temperature. For example, molasses cooling with D2 light was tried in late 90s by the group at LENS [62]. The molasses cooling resulted in an inefficient cooling of the gas and worked only for a small sample ($\sim 10^7$ atoms). This was mainly because the excited state in the D2 transition is not well-resolved as in other species. The narrow line 4S-5P cooling was tried by the Toronto group [63] but it is a little bit complicated to implement requiring different set of optics which work in the near-UV regime.

Recently, the group of Christophe Salomon at ENS has implemented gray molasses cooling in potassium [64]. This cooling scheme works on the $^4S_{1/2} \rightarrow {}^4P_{1/2}$, more commonly known as the D1 transition. The cooling works in combination of velocity-selective coherent population trapping (VSCPT) [65] and Sisyphus cooling [66]. VSCPT works by optically pumping atoms into the dark states whose lifetime depends on the square of the atomic velocity. This combines with of Sisyphus cooling, in which atom climb optical potential, created by counter-propagating beams, thus losing the kinetic energy.

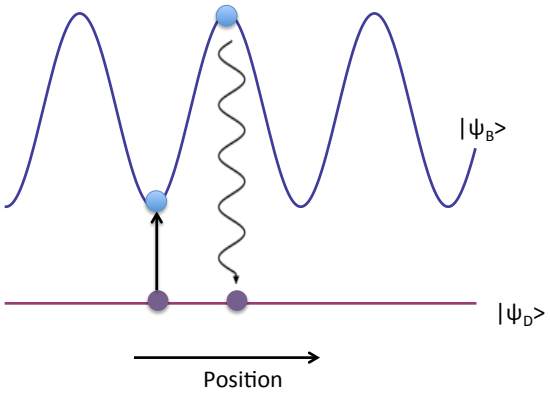

Figure 5.11: Gray molasses cooling. The cooling is a combination of velocity-selective coherent population trapping and Sisyphus cooling.

More specifically, atoms in the dark state do not change energy as a function of position. They can be excited to the bright state. The bright state energy level does vary with position

depending on the intensity and polarization of light. An atom has the highest probably of getting excited into the bright state at the bottom of the potential hill. Once the atom is in the bright state, it starts to climb the optical potential. As it reaches the top, it is optically pumped back to the dark state. As a consequence, excitation, climbing and pumping reduce the temperature of the sample below the Doppler limit.

The transitions for D1 cooling is shown in Figure 5.12. The ground state consists of $|F = 9/2\rangle$ and $|F = 7/2\rangle$ hyperfine manifolds of $^2S_{1/2}$ state. The excited state is the $|F' = 9/2\rangle$ and $|F' = 7/2\rangle$ hyperfine manifolds of the $^2P_{1/2}$ state. These are well separated by 155 MHz. The optical transitions of 770 nm light are blue shifted for both the "trap" $|F = 9/2\rangle \rightarrow |F' = 7/2\rangle$ and the "repump" $|F = 7/2\rangle \rightarrow |F' = 7/2\rangle$ transitions. We denote the detuning for the trap light as Δ and that for repump light as Δ_{repump}. The difference between the trap and the repump light is denoted by δ.

In the experimental sequence, once we load the atoms in the second MOT for 60 s, we change the detuning of the trap beam to move it closer to the resonance (1.5Γ) for 70 ms. This stage is known as compressed MOT (CMOT) which creates a slightly colder and denser MOT suitable for molasses cooling. Then, we turn off the optical beam and the quadrupole field in 100μs. We then shine the D1 beams at the atoms. In Figure 5.13. We vary the detuning of the trap laser Δ while keeping δ to be 0. Note that, since our goal was to improve the condition of the atoms after the transfer rather than optimize the gray molasses itself, we did the measurement of number and temperature at the end of cart transfer in the science cell. We see that the transferred atom number is maximum and the temperature is minimum at $\Delta = 2\Gamma$.

We also vary δ, shown in Figure 5.14, and find some strange behavior in number and temperature which could be due to on-resonance Raman transitions. Next we vary the power (Figure 5.16 and duration (Figure 5.15) of the molasses beams and observe a clear dependence.

In conclusion, we have implemented the D1 molasses beam to improve the initial condition for evaporation in the magnetic trap. Even though we did not fully characterize this cooling stage, we benefited tremendously in both transfer fraction and an efficient evaporation because of this stage of cooling, which I will discuss in the next two sections.

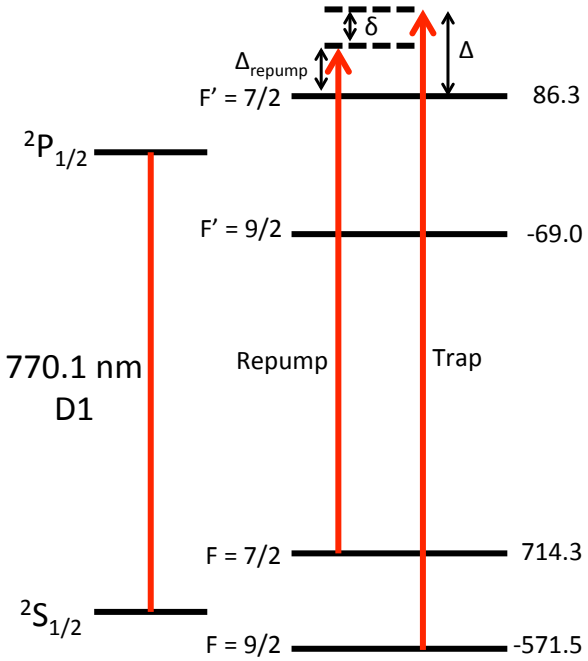

Figure 5.12: D1 transition lines for gray molasses cooling in ^{40}K. The numbers on the right correspond to the frequency shift of the hyperfine levels in MHz.

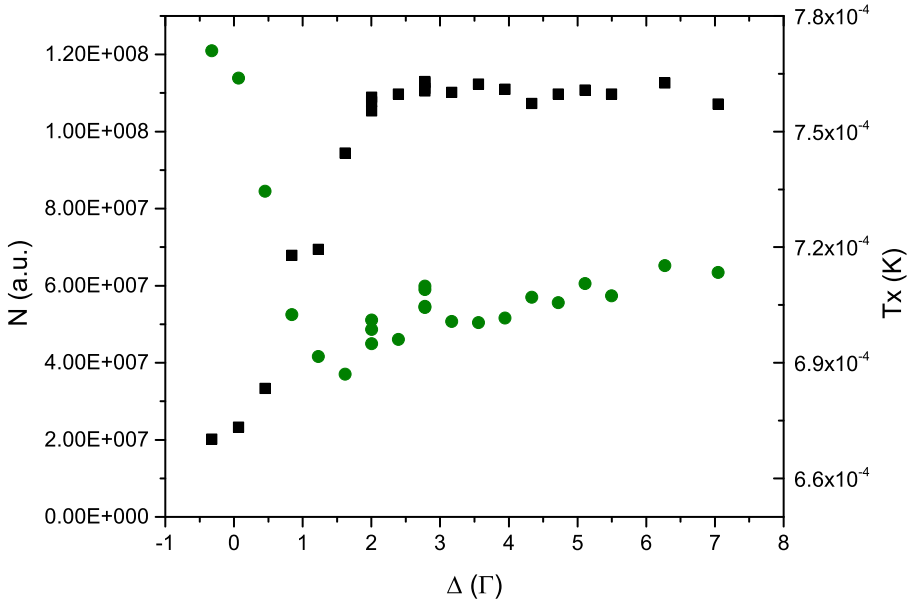

Figure 5.13: Number (black square) and temperature (green circle) of the atoms transferred to the science cell as a function of D1 trap frequency Δ while keeping $\delta = 0$. Note that zero is suppressed for temperature. The reason we don't see a drastic change in temperature is explained in the main text.

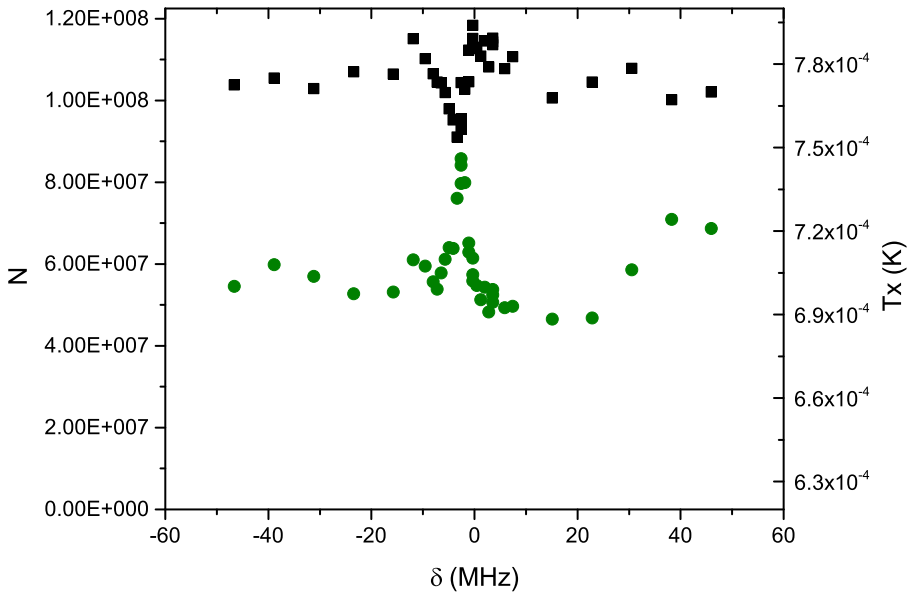

Figure 5.14: Number (black square) and temperature (green circle) of the atoms transferred to the science cell as a function of frequency difference between trap and repump beams δ.

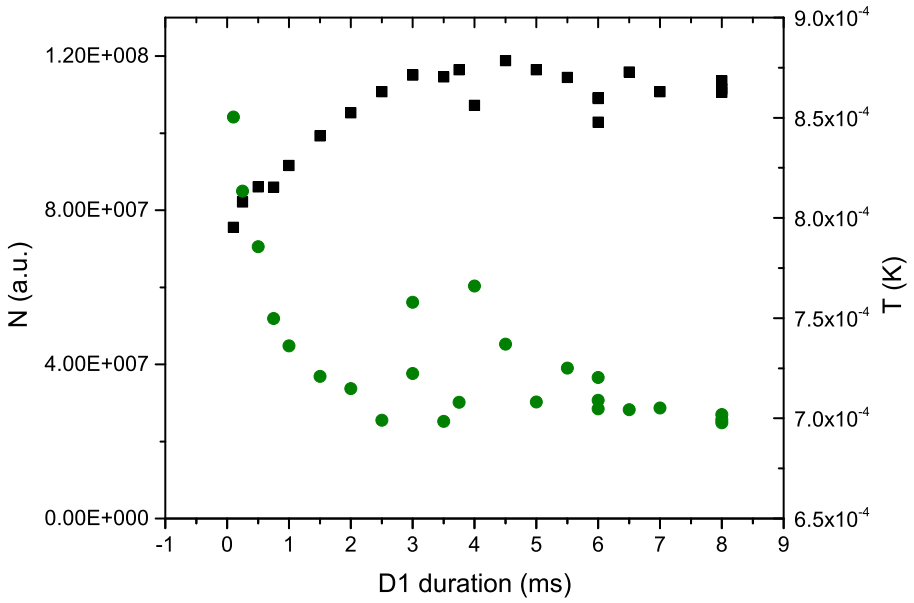

Figure 5.15: Number(black square) and temperature (green circle) of the atoms transferred to the science cell as a function of D1 molasses pulse duration.

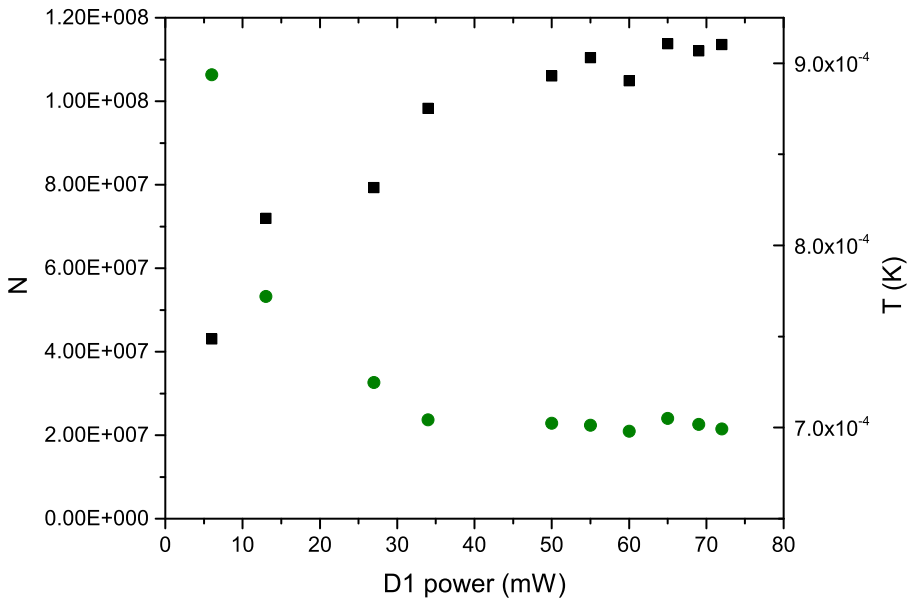

Figure 5.16: Number (black square) and temperature (green circle) of the atoms transferred to the science cell as a function of D1 molasses power (trap plus repump). Repump beam power is 1/10th trap beam power.

5.6 Loading to the quadrupole trap and cart transfer

5.6.1 Trapping in a magnetic trap

Atoms can be trapped in a magnetic trap by using the magnetic dipole moment. Atoms feel a force of $\vec{F} = \vec{\nabla}(\vec{\mu} \cdot \vec{B})$, where μ is the magnetic moment and $\vec{\nabla}$B is the magnetic field gradient. Different Zeeman spin states have different magnetic moments that results in $\vec{F} = g m_F \mu_0 \vec{\nabla} B$, where g is the Lande-g-factor and μ_0 is the Bohr magneton. If we use the low field seeking states, such as $|F = 9/2, m_F = 9/2\rangle$, $|F = 9/2, m_F = 7/2\rangle$ and $|F = 9/2, m_F = 5/2\rangle$ with a positive magnetic moment, these atoms can be trapped in a magnetic trap. $m_F = 9/2$ has a magnetic moment of μ_B, Bohr magneton. Similarly, at low field $m_F = 7/2$ has a magnetic moment of 7/9 μ_B and $m_F = 5/2$ has a magnetic moment of 5/9 μ_B. The Zeeman energy shift of the magnetic Zeeman sub-levels is shown in Figure 5.28.

5.6.2 Optical pumping and loading

Once the atoms are cooled to sub-Doppler temperatures after the D1 molasses cooling stage, they are optically pumped to low field seeking zeeman states using a circularly polarized (σ^+) pulse. For potassium, the $|F = 9/2, m_F = 9/2\rangle$ and $|F = 9/2, m_F = 7/2\rangle$ are low field seeking states. During optical pumping, we keep the bias field at about 4 Gauss.

We scanned the frequency of the transition to find that the most efficient transition is the $|F' = 11/2, m_{F'} = 9/2\rangle$ (Figure 5.17). We also scanned the polarization of the light using a quarterwave plate (Figure 5.19). This way we determine the purely circularly polarized light. Once the atoms are optically pumped, we ramp up the magnetic field gradient to 100 G/cm in 10 ms. The pair of quadrupole coils sit on a track, which allows us to move the atoms to the final science cell region.

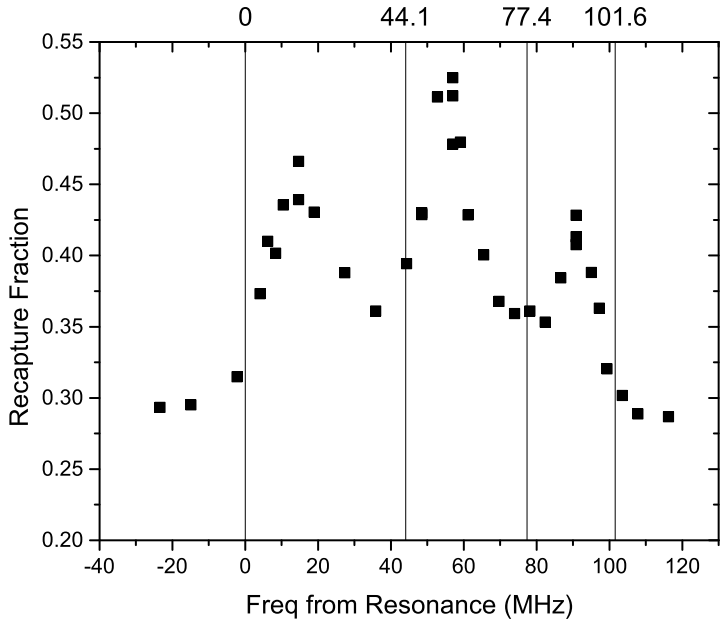

Figure 5.17: Finding the right transition for optical pumping. We vary the optical pumping frequency, load the atoms to the quadrupole trap, hold for a short time and measure the MOT recapture fraction. The four lines corresponds to the energy of the Zeeman levels.

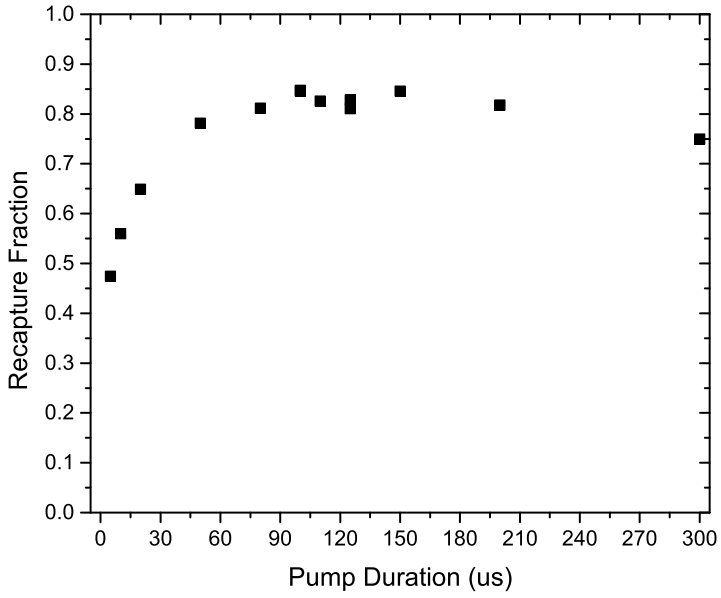

Figure 5.18: We vary the optical pumping pulse duration and measure the recapture fraction. We find out that the recapture fraction saturates beyond 80 μs

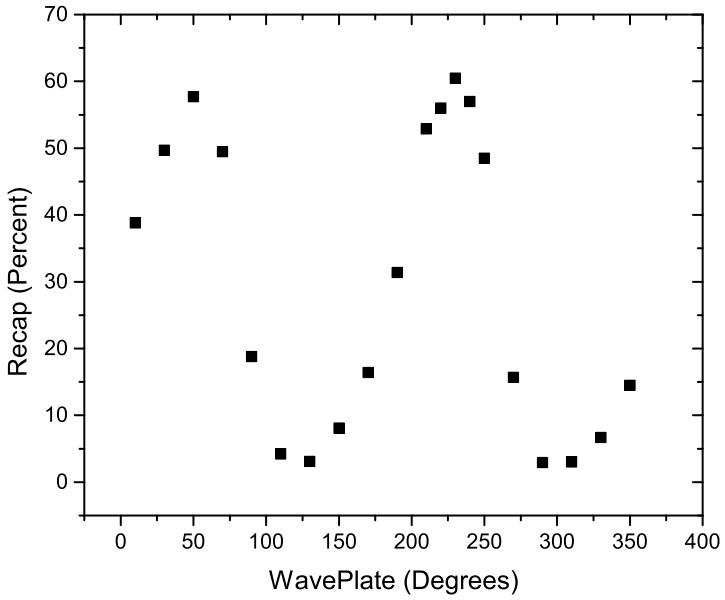

Figure 5.19: Optical pumping transitions needs a σ^+ light. Here, we vary the polarization of light using a quarter-wave plate to find the right polarization.

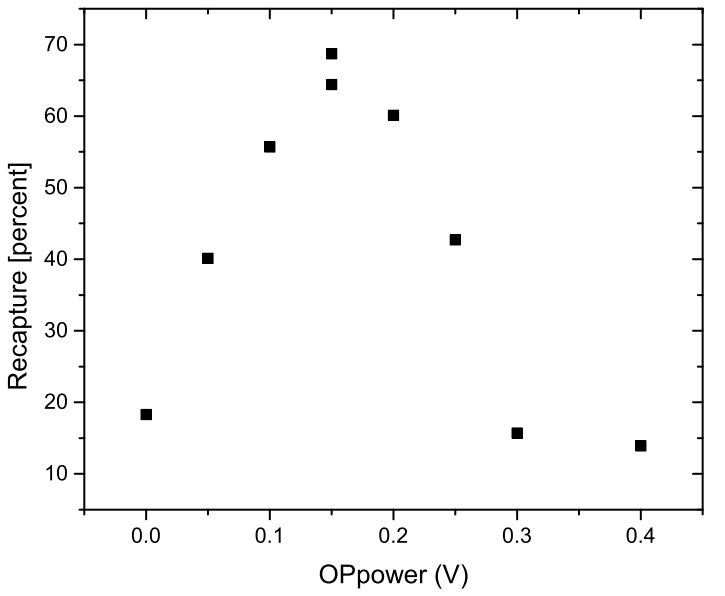

Figure 5.20: We vary the optical pumping power to get the highest number of atoms into the quadrupole trap. We vary the voltage driving the AOM frequency driver. 0.15V corresponds to 13.5 μW of optical power and the power varies linearly with voltage in this regime.

5.6.3 Pros and cons of using a cart

At the building stage of the apparatus, we explored different options for transporting atoms to science cell. The three popular options are: optical transport, multi-coil transport and cart transport. We quickly ruled out the option for optical transport because it requires a high power far-detuned dipole trap. The power requirement is set by the MOT or gray molasses temperature, size of the cloud and the mass of the atoms. That means for potassium it amounts to around 80 W of 1064 nm light. The second option was to do multi-coil transfer, which requires ramping up and down the current in a series of quadrupole coils to guide the atoms smoothly to the science area. Although initially this was our plan, we hesitated at the end because first it seemed like it will take a long time to implement for an efficient transfer of atoms. The other reason is the separation distance between the coils. Since our coils are separated by a large distance, we need to run around 300A of current to produce a field gradient of 100 G/cm in the strong direction. To run 300 A of current, the coils have to be water cooled. It seemed like this will be a big hassle to water cool 8 or 9 pairs of coils.

Finally, we decided to adopt the cart transfer technology that was developed in JILA in late 90s [67]. Implementing cart transfer is relatively straight forward as it requires only a single pair of quadrupole coils. We bought a commercial track from Parker Motion in Denver, installed the cart coils, programmed the motion using the software provided by the company.

One problem of using a cart is the space requirement on the optics table. The other downside is that it forces us to have a magnetic trap in our sequence. With a good gray molasses cooling, we could have tried optical transport and performed all-optical cooling, which would have resulted in a much faster cycle time.

5.6.4 Transfer efficiency

The transfer efficiency of the atoms to the science cell is shown in Figure 5.21. To perform this measurement, we captured the fluorescence of the MOT on the PixelFly camera. Then we

loaded the atoms to the quadrupole trap, and moved them to a specific point. We then moved the atoms back and recaptured back to the second MOT and measured the fluorescence. This gave us the fraction of the atoms captured back in the MOT after the transfer. The one-way transfer efficiency is the square root of that fraction. All the measurements took the same amount of time. We found out that the gray molasses cooling significantly improves the transfer efficiency to the point where it is limited only by the vacuum lifetime.

5.7 Evaporation in the QUIC trap

Once the atoms are transferred to the science cell, we ramp down the cart quadrupole current and ramp up the stationary quadrupole current simultaneous until the field gradient reaches 200 G/cm. We cannot evaporate in the purely quadrupole trap because of the Majorana losses. In a quadrupole magnetic trap there is a zero field region at the center at which the atoms undergo spin flip to untrapped states and are eventually lost from the trap. This phenomena is called Majorana spin flip. Majorana spin flip is avoided as long as the Larmor period of an atom in the magnetic trap remains small compared to the typical flipping time r/v of the field seen by the atom. Following Ref [68], we get the Majorana loss rate is

$$\tau = \frac{mR^2}{\hbar} \tag{5.16}$$

Using this condition, for a cloud of potassium atoms of size 0.5 mm , this means the timescale for Majorana loss is 157 s. However, we spent a couple of months trying to evaporate in a purely quadrupole trap but did not succeed.

We turned the quadrupole potential produced by the quadrupole coils into a harmonic potential by ramping up the current in the Ioffe coil in 500 ms. The field produced by the QUIC trap is,

$$|\vec{B}_{\mathrm{QUIC}}| = |\vec{B}_{\mathrm{q}} + \vec{B}_{\mathrm{Ioffe}}| \tag{5.17}$$

$$\sim B_0 + \gamma y^2 + \frac{1}{2}\left(\frac{\left(\frac{3}{2}\nabla B\right)^2}{B_0} - \gamma^2\right)\rho^2, \tag{5.18}$$

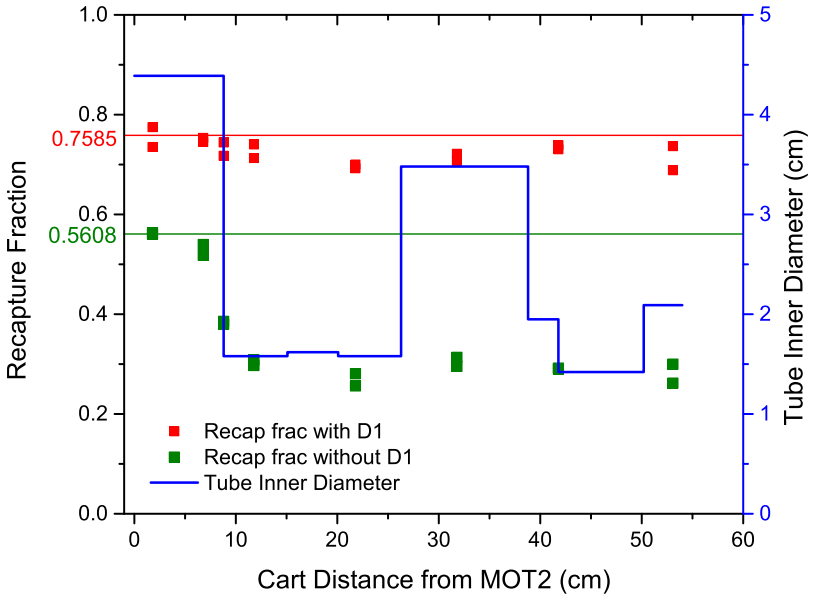

Figure 5.21: We measure the transfer efficiency of the atoms as a function of transfer distance through the transfer tube to the science cell. The red points are with D1-gray molasses cooling and the green points are without molasses cooling. The blue line is the diameter of the transfer tube. The center of the science cell is 54 cm away. We find that the transfer efficiency is only limited by the vacuum lifetime in the case of D1-cooled atoms. Without D1-cooling, we see that most of the atoms are lost coming right out of the chamber going through the narrow part of the tube.

where B_0 is the offset frequency, γ is the axial curvature and $\rho = \sqrt{x^2 + z^2}$. We can then derive the trapping frequency,

$$f_y = \frac{1}{2\pi}\sqrt{\frac{\mu}{m}2\gamma} \tag{5.19}$$

$$f_r = \frac{1}{2\pi}\sqrt{\frac{\mu}{m}\left(\frac{\nabla B^2}{B_0} - \gamma\right)} \tag{5.20}$$

The measurement of the trapping frequency as a function of the field gradient is shown in Figure 5.23.

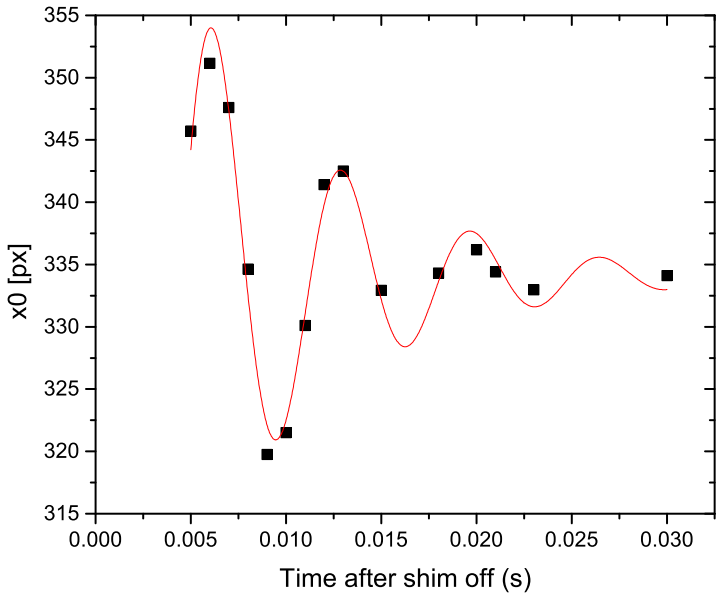

Figure 5.22: We measure the trapping frequency in the QUIC trap by sloshing the atoms with a field gradient pulse and measuring the center position in TOF as a function of hold time.

The background s-wave scattering length of $m_F = 9/2$ and $m_F = 7/2$ is $170a_0$ and is favorable for the evaporation. Until we reach a cold temperature, the p-wave cross-section is also favorable as shown in Figure . We use the microwave transition between $|F = 9/2\rangle$ and $|F' = 7/2\rangle$ transition for evaporation. We sweep the frequency from 1190 MHz to around 1278 MHz in multiple exponential stages. Each stage has its exponential parameters α and β described as follows:

$$f(t) = f_b + (f_0 - f_b)e^{-\alpha t - \beta t^2}, \tag{5.21}$$

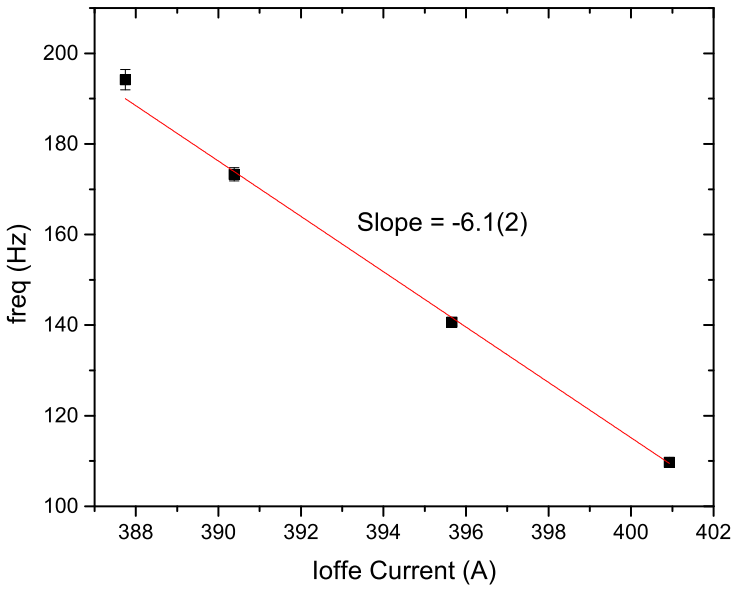

Figure 5.23: We vary the current in the Ioffe coil and measure the trapping frequency.

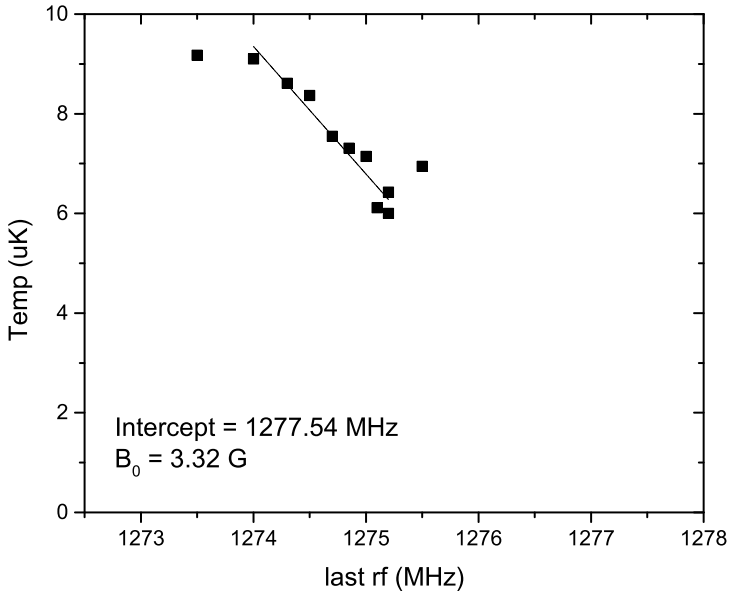

Figure 5.24: We measure the bias field of the QUIC trap by measuring the temperature of the cloud at the end of the evaporation and linearly extrapolating to find the frequency where the temperature goes to zero. Depending on this frequency, we can calculate the magnetic field.

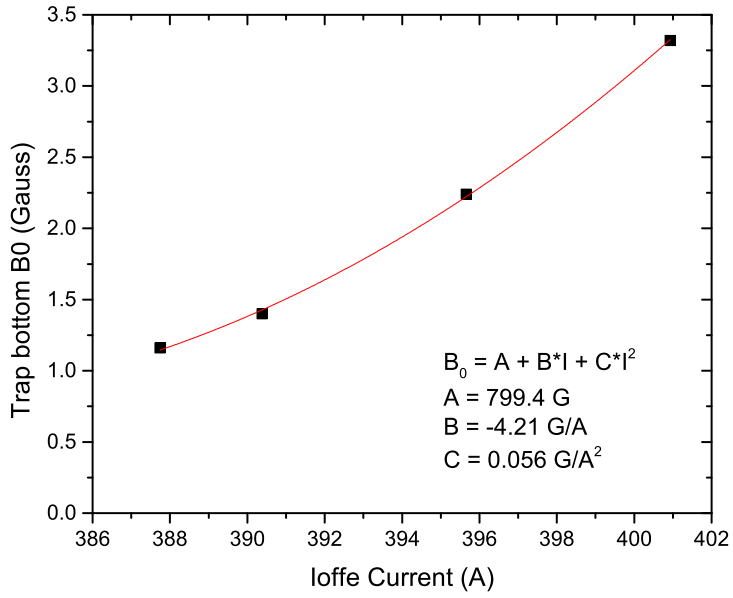

Figure 5.25: We vary the current in the Ioffe coil and measure the bias field. For a good evaporation, we would like to have a bias field of a few Gauss.

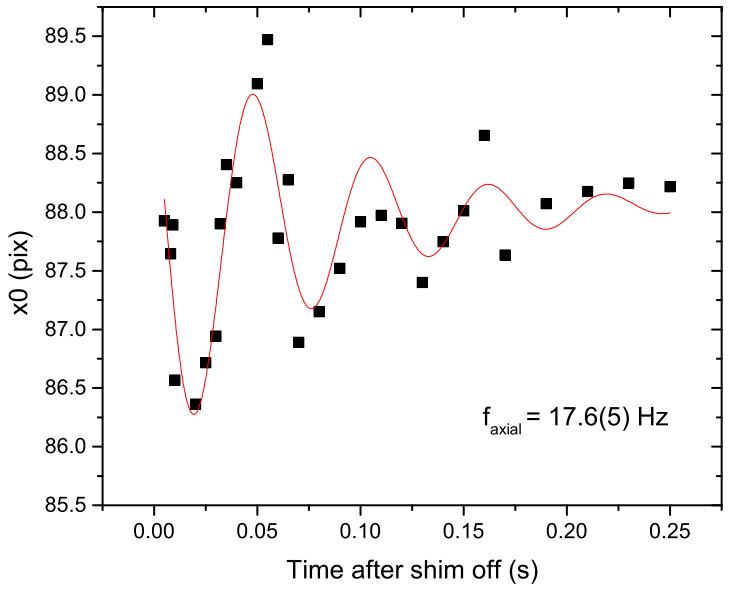

Figure 5.26: We measure the axial trapping frequency of the QUIC trap by sloshing the atoms in the axial direction with a field gradient pulse and measuring the center position in TOF as a function of hold time.

where f(t) is the frequency at time t during evaporation, f_b is the bottom frequency and f_0 is the start frequency for each stage. We optimized the evaporation as follows using the parameters in Table 5.1

Table 5.1: We use three exponential stages and optimized the evaporation in the QUIC trap.

Stage	α (Hz)	β (Hz^2)
1190 - 1250 MHz	0.07	0
1250 - 1270 MHz	0.05	0
1270 - 1278 MHz	0.05	0.001

From the evaporation trajectory, we find that the parameter α = d Log T/ d Log N = 1.05 $>$ 1. From phase space density, we get Γ = d Log PSD/ d Log N = -2.2. The condition for a "runaway" evaporation is that the collision rate increases with evaporation [69]. The collision rate is given by $\gamma = n\sigma v$, where n is the density of the particles in the trap, σ is the collision cross-section, which is roughly constant in the temperature of range of evaporation, and v is the rms velocity. In a simple case of a harmonic trap, the density scales as $\sim N/T^{3/2}$ and v scales as $T^{1/2}$, hence the collision rate scales as N/T. Thus, for a Log T vs Log N plot, we expect a slope of larger than one for a good evaporation.

We typically evaporate the atoms down to 10-20 μK with $N \sim 10^7$. This temperature is low enough for us to load atoms into an optical dipole trap. The typical shot-to-shot number noise (standard deviation/average) at the end of the evaporation is 7% and temperature noise is less than 5%.

5.8 Optical Dipole Trap

The last stage of evaporation occurs in an optical dipole trap (ODT). Since the useful Feshbach resonance to do RF spectroscopy is between $|F = 9/2, m_F = -9/2\rangle$ and $|F = 9/2, m_F = -7/2\rangle$, which are high-field seeking spin states, we cannot continue using a magnetic trap. Atoms are therefore transferred to an optical dipole trap, where trapping of both high and low magnetic

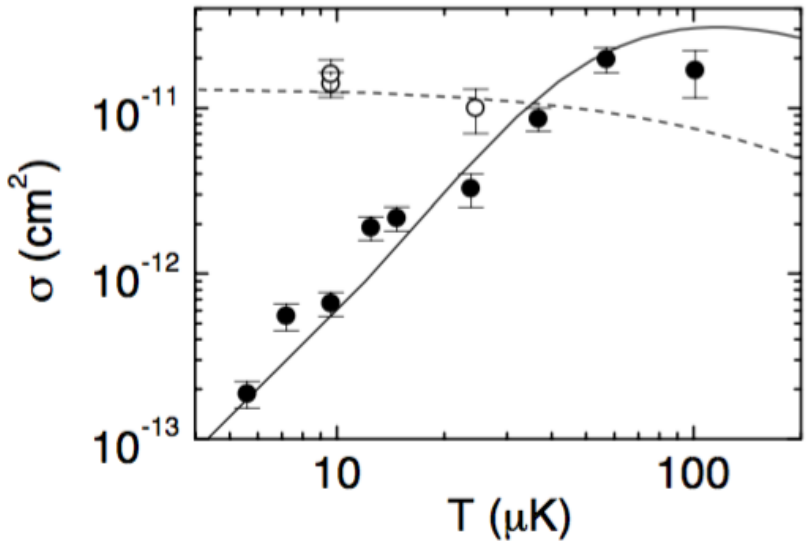

Figure 5.27: Elastic cross-section vs temperature. The plot is reproduced from [11]. The filled circles are the p-wave scattering cross-section for spin polarized cloud and the open circles are the s-wave cross section for mixed spin states. We see that the p-wave cross-section is large down to 100 μK and plummets as the temperature is reduced. The s-wave cross-section is relatively flat as a function of temperature.

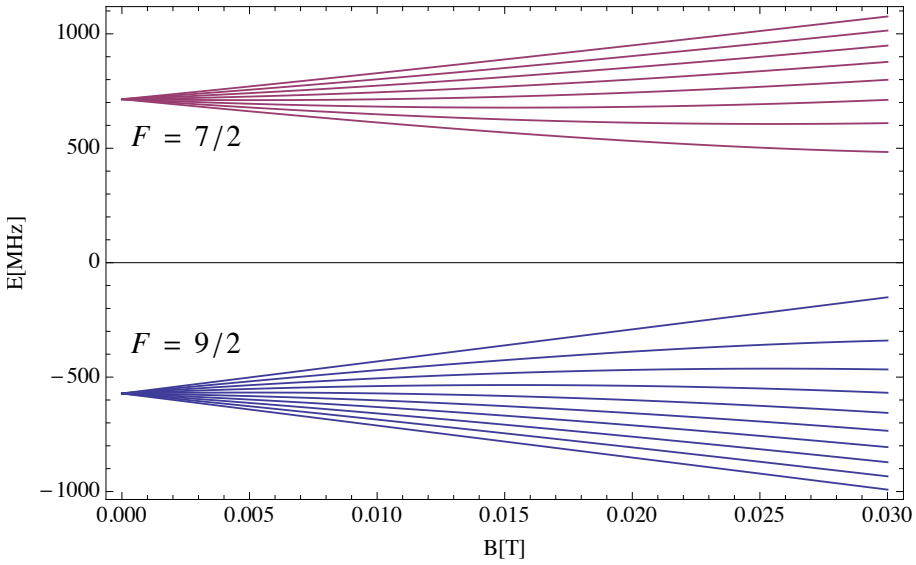

Figure 5.28: Zeeman sublevels of the ground levels in potassium. The evaporation microwave transfers the atoms in $|F = 9/2, m_F = 9/2\rangle$ and $|F = 9/2, m_F = 7/2\rangle$ to $F = 7/2$ hyperfine level, where they become high-field seeking and leave the trap.

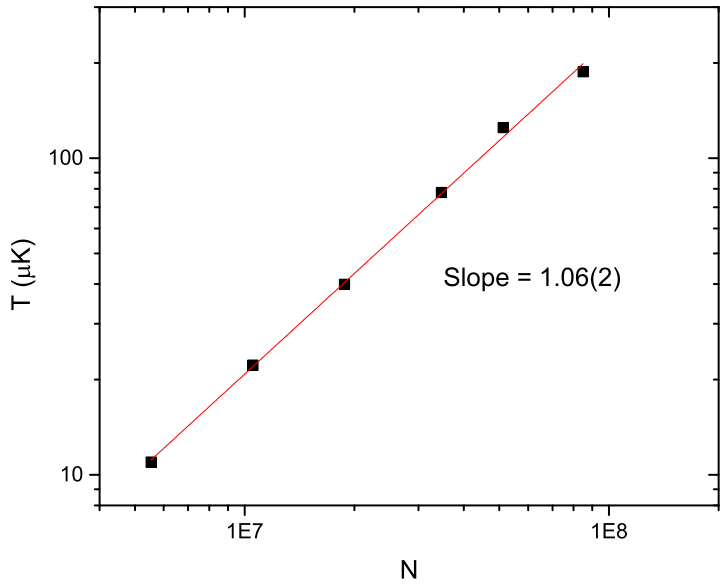

Figure 5.29: The evaporation trajectory of the atoms plotted as Log T vs Log N. For a good evaporation which increases the collision rate, we need the slope of this to be greater than 1.

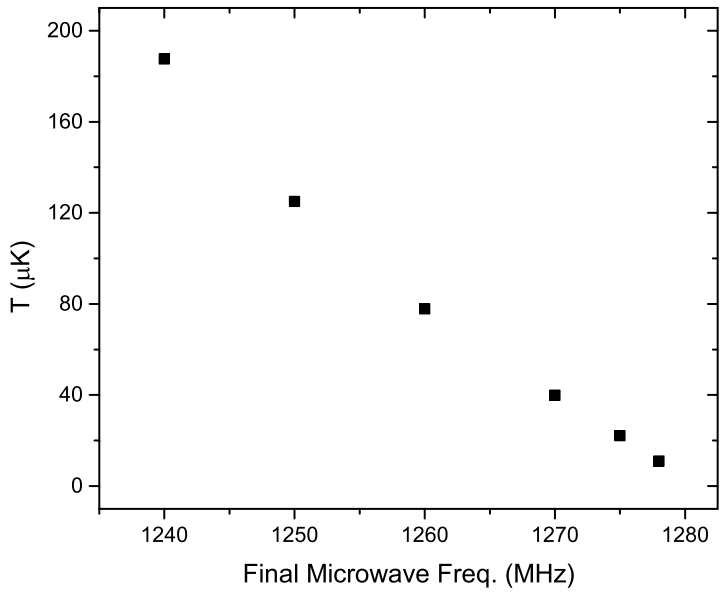

Figure 5.30: The evaporation trajectory of the atoms plotted as temperature vs final microwave frequency.

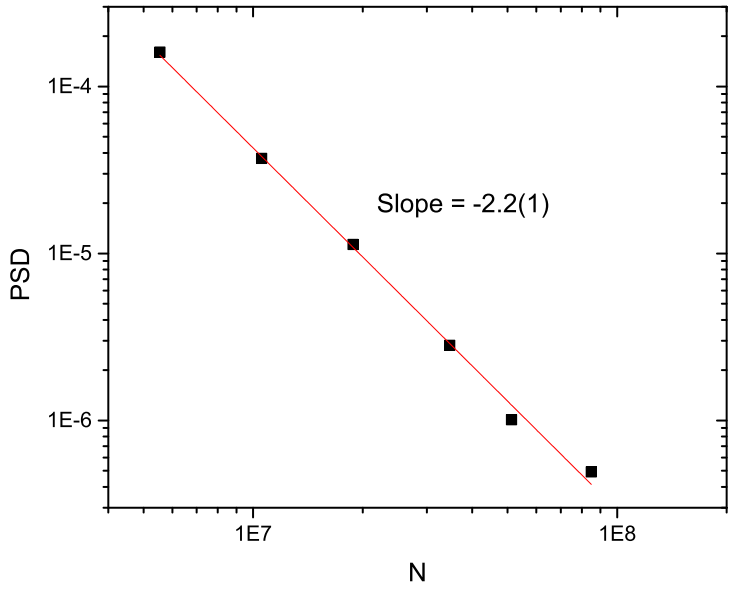

Figure 5.31: The evaporation trajectory of the atoms plotted as Log PSD vs Log N.

field seeking states is possible.

An optical trap works in the principle of atom interaction with a far off-resonant light [70]. The electric field of a laser $\mathbf{E}$ induces an atomic dipole moment $\mathbf{p}$ in an atom that oscillates with the light frequency ω, where $\mathbf{E}(\mathbf{r},t) = \hat{\mathbf{e}}E(\mathbf{r})\exp(-i\omega t) + c.c.$ and $\mathbf{p} = \hat{e}p(r)\exp(-i\omega t) + c.c.$. The amplitude of the dipole moment $\mathbf{p}$ is given by,

$$p = \alpha E, \tag{5.22}$$

where α is the complex polarizability. The interaction potential is given by,

$$U_{dip}(\mathbf{r}) = -\frac{1}{2}\langle \mathbf{pE} \rangle = -\frac{1}{2\epsilon_0 c} Re(\alpha) I(\mathbf{r}), \tag{5.23}$$

where is $\alpha = 6\pi\epsilon_0 c^3 \frac{\Gamma/\omega_0^2}{\omega_0^2 - \omega^2 - i(\omega^3/\omega_0^2)\Gamma}$. Hence,

$$U_{dip}(\mathbf{r}) = -\frac{3\pi c^2}{2\omega_0^3}\left(\frac{\Gamma}{\omega_0 - \omega} + \frac{\Gamma}{\omega_0 - \omega}\right) I(\mathbf{r}), \tag{5.24}$$

where ω_0 is the frequency of the resonance. And the scattering rate is given by,

$$\Gamma_{scatt}(\mathbf{r}) = -\frac{3\pi c^2}{2\hbar\omega_0^3}\left(\frac{\omega}{\omega_0}\right)^3\left(\frac{\Gamma}{\omega_0 - \omega} + \frac{\Gamma}{\omega_0 - \omega}\right) I(\mathbf{r}). \tag{5.25}$$

In our case, $\omega \approx \omega_0$, so,

$$U_{dip}(\mathbf{r}) = \frac{3\pi c^2}{2\omega_0^3}\frac{\Gamma}{\Delta} I(\mathbf{r}), \tag{5.26}$$

$$\Gamma_{scatt} = \frac{3\pi c^2}{2\hbar\omega_0^3}\left(\frac{\Gamma}{\Delta}\right)^2 I(\mathbf{r}), \tag{5.27}$$

where $\Delta = \omega - \omega_0$.

For a Gaussian laser beam, the intensity profile is given by,

$$I(r) = \frac{2P/(\pi w^2)}{1 + z/z_R^2} E^{-r^2/(1+z/z_R^2)}, \tag{5.28}$$

where P is the power of the beam, w is the Gaussian beam waist and $z_R = \pi w^2/\lambda$ is the rayleigh range.

We setup a crossed dipole trap (horizontal and vertical) as described in Chapter 4, with a 1064 nm light. The beam waist of the horizontal beam is 25 μm and that of the vertical beam

is 150 μm. We start with a 2 W beam in the horizontal direction and 150 mW in the vertical direction. The trap depth is 302 μK and the trapping frequency is 3 kHz in the radial direction.

We measure the trapping frequency at the end of the evaporation by modulating the intensity of the beam. We modulate the intensity by using an external set point from a frequency generator in the set point port of the intensity servo at 30% of the amplitude. We see a loss of atoms at twice the trapping frequency (Figure 5.32).

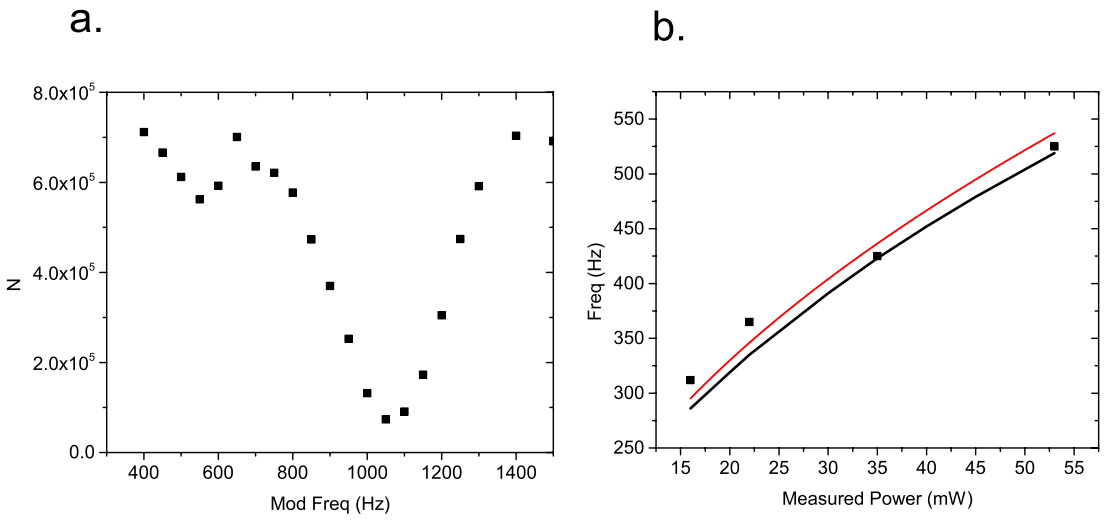

Figure 5.32: a. Measurement of the radial trapping frequency by modulating the horizontal dipole trap beam. We see a loss in number at twice the trapping frequency and a small feature at the trap frequency. We have done a similar measurement to measure the trapping frequency in the axial direction by modulating the vertical dipole trap beam. b. Radial trap frequency vs power of the dipole trap beam. The red line is the fit to $P^{1/2}$ and the black line is from calculation.

We load the atoms into the dipole trap by turning on the dipole trap beam to 2W while at the same time ramping down the quadrupole trap current in 500 ms to half the value. After 400 ms overlap between the quadrupole trap and the optical dipole trap, we shut down the magnetic trap (both quadrupole and Ioffe coil) in 200 μs leaving the atoms trapped only by the optical potential. Then, we do a Landau-Zener transition to move the atoms from positive m_F states (mostly in $m_F = 9/2$ state) to negative m_F states using an RF sweep from 7 MHz to 5 MHz in 10 ms at 20 Gauss. We transfer about 90% of the atoms to the negative spin states. Immediately following the

sweep, we ramp the magnetic field from 20 Gauss to 208 Gauss in 100 ms. At the end of the ramp, we use another RF pulse of 100 μs at 47 MHz to create a 50/50 mixture of $|F = 9/2, m_F = -9/2\rangle$ and $|F = 9/2, m_F = -7/2\rangle$ spin states.

We evaporate the atoms in the dipole trap by lowering the intensity of the horizontal trapping beam. We exponentially lower the power of the beam from 2 W to 20 mW in 12 s.

The evaporation trajectory of a typical evaporation is shown in Figure 5.33. The slope α =Log T/ Log N = 1.8, which means the evaporation is efficient. At the end of the evaporation, we reach about $N = 4 \times 10^4$ and $T = 100$ nK, which corresponds to $T/T_F = 0.1$. The thermometry of fermions at low temperature is described in the next section.

5.9 Thermometry

Thermometry of ultracold atoms can be done by imaging the atoms after a long time of flight. This measures the momentum distribution of the cloud and the average size(momentum) corresponds to the temperature of the cloud. However, this technique only works for a thermal cloud. Once the cloud is degenerate, the cloud is no longer Gaussian. For an in-depth thermometry derivation for trapped Fermi gases, please see ref. [11].

The Hamiltonian for a single particle trapped in a harmonic potential is:

$$H = \frac{1}{2m}\left(p_x^2 + p_y^2 + p_z^2\right) + \frac{m}{2}\left(\omega_r^2 x^2 + \omega_r^2 y^2 + \omega_z^2 z^2\right) \tag{5.29}$$

where ω_r and ω_z are the trap frequency in radial and axial direction respectively. The distribution and the density of states of the particles is

$$n(\epsilon) = \frac{1}{\mathfrak{Z}^{-1} exp(\epsilon/k_b T) + 1}, \tag{5.30}$$

$$g(\epsilon) = \frac{\epsilon^2}{2(\omega_z/\omega_r)(\hbar\omega_r)^3}, \tag{5.31}$$

where $\mathfrak{Z}$ is the fugacity of the gas. The total number of atoms can be calculated by integrating the density of states to $E_F = k_B T_F$, which gives

$$N = \frac{E_F^3}{6\hbar^3\omega_r^2\omega_z}. \tag{5.32}$$

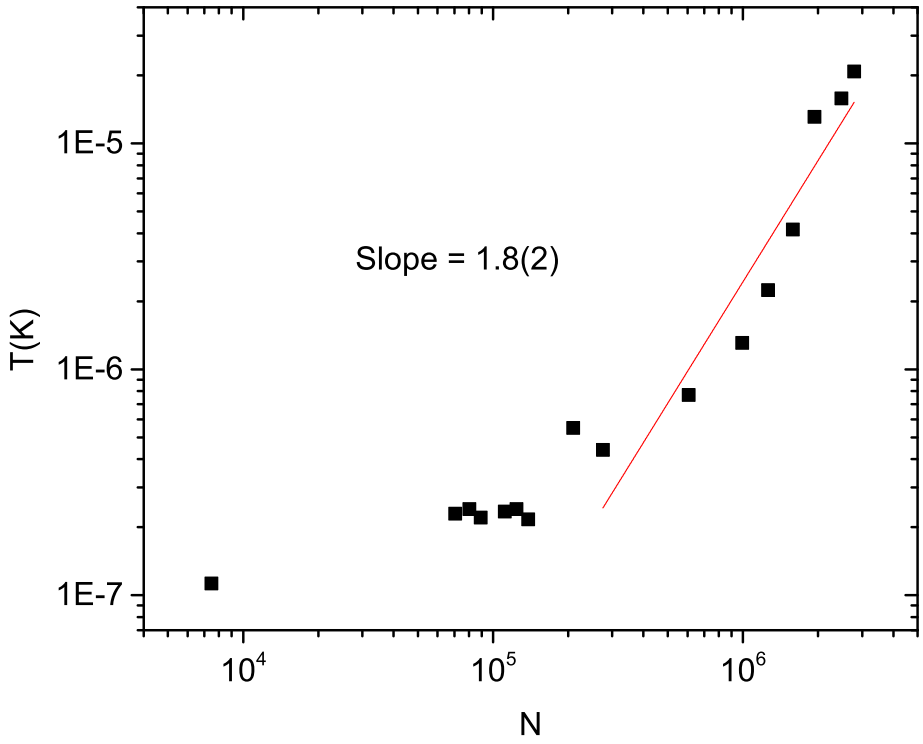

Figure 5.33: Evaporation trajectory for the optical trap evaporation as we lower the horizontal dipole trap intensity. We see that the slope of Log T/Log N is 1.8 which means the evaporation in the dipole trap is much better than that in the magnetic trap. At certain point, we see the evaporation saturates: we see a loss in number without seeing a loss in temperature. This is because for this evaporation we started with an imbalanced gas in $m_F = 9/2$ and $m_F = 7/2$. We lost all of the minority $m_F = 7/2$ atoms and only $m_F = 9/2$ remain. To get to colder temperature, we had to start with a 50/50 mixture of spin states.

Hence, the Fermi energy is

$$E_F = \hbar \left(6\omega_r^2 \omega_z N\right)^{1/3}. \tag{5.33}$$

Now, we can integrate $N = \int_0^\infty g(\epsilon) n(\epsilon) d\epsilon$ to give

$$N = -\frac{1}{\omega_r^2 \omega_z} \left(\frac{k_T T}{\hbar}\right)^3 Li_3(-\mathfrak{Z}), \tag{5.34}$$

where Li_3 is the polylog function. By rearranging this equation and substituting T_F for N, we get,

$$Li_3(-\mathfrak{Z}) = -\frac{1}{6(T/T_F)^3} \tag{5.35}$$

Since we expand the cloud for time t and measure the column integrated profile. The 2D optical depth for a trapped Fermi gas is given by,

$$OD(y,z) = -\frac{\sigma_\lambda}{2\sqrt{1+(\omega_r t)^2}\sqrt{1+(\omega_z t)^2}} \frac{m(k_B T)^2}{\pi \hbar^3 \omega_r} Li_2\left(-\mathfrak{Z} e^{-y^2/(2\sigma_r^2)} e^{-z^2/(2\sigma_z^2)}\right). \tag{5.36}$$

Here, σ_λ is the absorption cross-section, and $\sigma_r^2 = \frac{k_B T}{m\omega_r^2}\left(1+(\omega_r t)^2\right)$ and $\sigma_z^2 = \frac{k_B T}{m\omega_z^2}\left(1+(\omega_r t)^2\right)$ are the cloud size. For the fitting purpose, we reduce this equation to,

$$OD(y,z) = OD_{pk} Li_2\left(-\mathfrak{Z} e^{-y^2/(2\sigma_r^2)} e^{-z^2/(2\sigma_z^2)}\right) / Li_2(-\mathfrak{Z}) \tag{5.37}$$

We fit a two dimensional image of atoms to this equation with fit parameters $OD_{pk}, \mathfrak{Z}, \sigma_y, \sigma_z$ and background offsets. A typical fit of a degenerate Fermi gas to this distribution is shown in Figure 5.34.

By substituting $\mathfrak{Z}$ to equation 5.35 and numerically solving, we can determine T/T_F of the gas. We can then compare this T/T_F to that found by finding T from σ and T_F from N and the trapping frequencies. The comparison of these two fits at various temperature is shown in Figure 5.35.

5.10 Imaging

We can get the number of atoms by doing fluorescence imaging as described in Section 5.2.1. However, this method does not allow us to measure the momentum distribution or temperature of

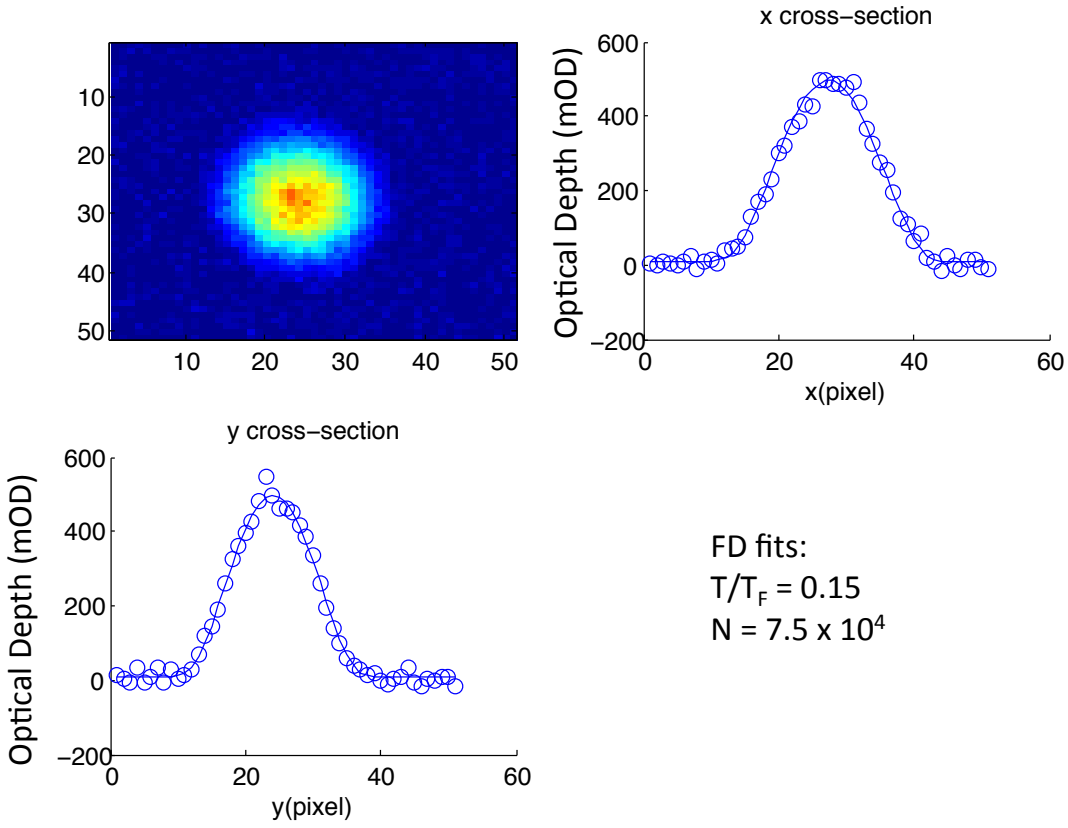

Figure 5.34: An example of a 2D surface fit of a degenerate cloud to an FD fit in 5.37.

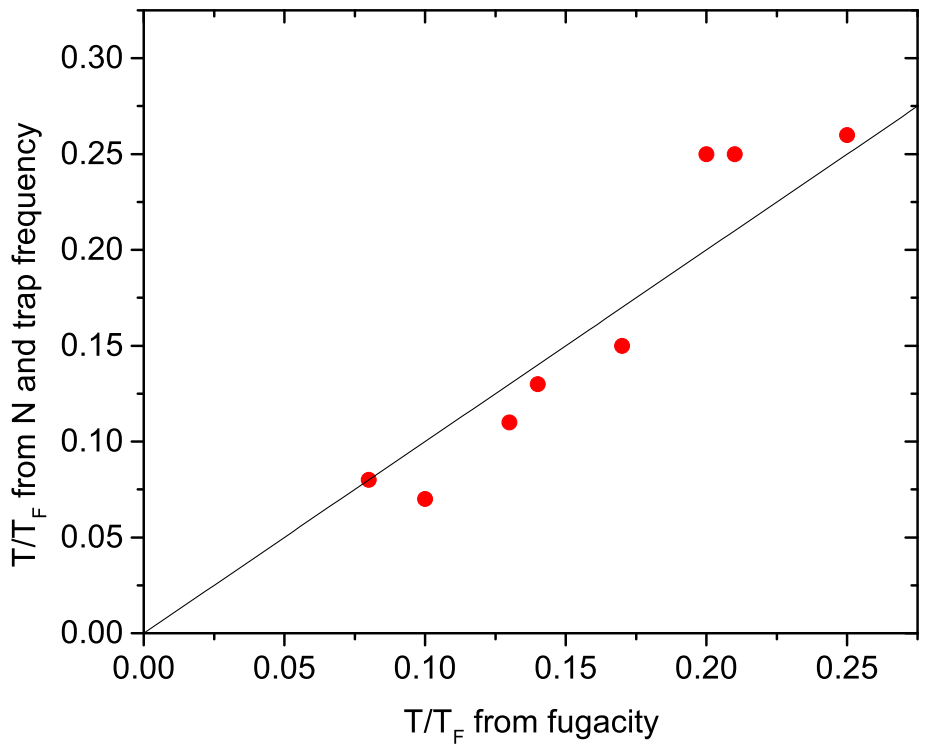

Figure 5.35: A comparison of the temperature of the gas measured in two different ways. The x-axis is the T/T_F extracted from the fugacity of the cloud using an FD fit. The y-axis is the T/T_F extracted by measuring the temperature from σ of the cloud (Equation 5.37) and the T_F from number and trapping frequency. The line has a slope of 1.

the gas. We thus have to perform absorption imaging after a long time of flight compared to the trapping frequency. Absorption imaging works on the principle of Beer's law. When we shine a beam on a cloud of atoms, the intensity of the beam as passes through the gas is

$$I(z) = I_0 e^{-OD(z)}, \tag{5.38}$$

or the total optical depth of the cloud is,

$$OD = ln\left(I/I_0\right) \tag{5.39}$$

Experimentally, we shine a 40μs pulse of the probe light on the atoms and take a picture of the beam after it passes through the atoms on a CCD camera and label as shadow "S". The intensity of the beam is kept to less than 10% of I_{sat} to avoid further correction. We wait 200 ms and let the atoms fall under gravity to the bottom of the cell. At that time, we pulse an identical pulse of light and take another image and label as light "L". We take a third picture without any probing pulse and label as background "B". The optical depth of the cloud is then,

$$OD(y,z) = -ln\left(\frac{S-B}{L-B}\right) \tag{5.40}$$

We can thus do a surface Gaussian fit or a surface Fermi Dirac fit to find the temperature and number of the cloud. The imaging setup to do fluorescence and absorption imaging is show in Figure 5.36. Because the probe beam has to go though a long transfer tube with a narrow diameter, we cannot do a long TOF in this chamber.

The imaging setup for the radial profile in the science cell is shown in Figure 5.37. The probe transition for the atoms are $|F = 9/2, m_F = 9/2\rangle \rightarrow |F = 11/2, m_F = 11/2\rangle$, and $|F = 9/2, m_F = 7/2\rangle \rightarrow |F = 11/2, m_F = 9/2\rangle$ for the positive spin states requiring a σ^+ light. For negative spin states, we use $|F = 9/2, m_F = -9/2\rangle \rightarrow |F = -11/2, m_F = 11/2\rangle$, and $|F = 9/2, m_F = -7/2\rangle \rightarrow |F = -9/2, m_F = 7/2\rangle$.

We do spin resolved imaging by either using the Stern-Gerlach technique or by going to high-magnetic field such that the transition of the different spin states are much larger than the transition linewidth. For the Stern-Gerlach method, we use a small coil placed underneath the cell

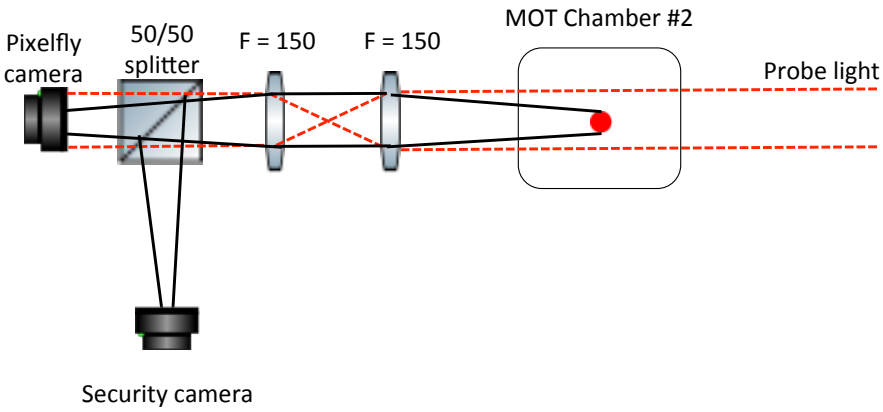

Figure 5.36: Imaging setup for MOT # 2. We can do either absorption imaging or fluorescence imaging with this setup. The setup has a magnification of 1. There's also a 50/50 beam splitter which allow us to look a the MOT fluorescence with a security camera.

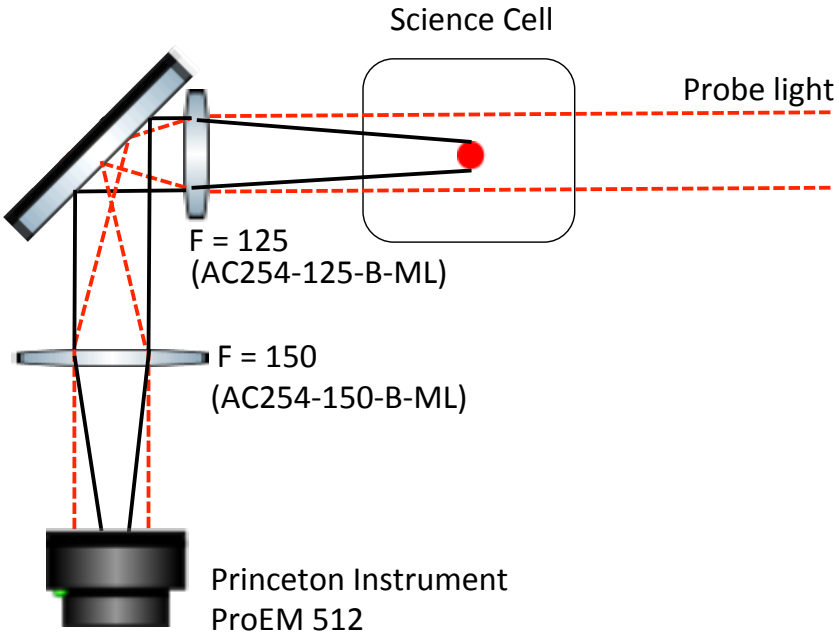

Figure 5.37: Imaging setup for imaging atoms in the science cell in the radial direction. The probe light is sent in the same direction as the horizontal dipole trap.

which produces a gradient of 70 Gauss/cm. During the time of flight, we turn on this coil for 5 ms such that atoms experience a force dependent on the magnetic moment. We do a usual absorption imaging at low field to image various spin states which are spatially separated. An example of such a measurement is shown in Figure 5.38. Note that we stitched two OD images together with different probe polarizations as the transition for positive spin states require a σ^+ probe light and that for negative requires a σ^-.

For high field imaging, we use the Feshbach coil as the bias field for imaging. Near 200G, the transitions for $m_F = 9/2$ and $m_F = 7/2$ are separated by about 45 MHz. We send a linearly polarized beam to the atoms, thus the OD we measure for the atoms needs a factor of two correction(verified experimentally).

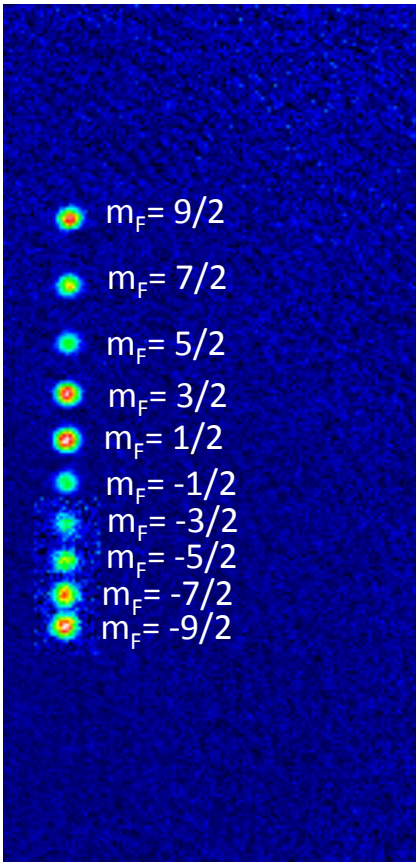

Figure 5.38: Stern Gerlach imaging of the atoms in different Zeeman state. Note that this image consists of two OD images stitched together, one for positive spin states and another for negative spin states.

Chapter 6

Conclusion and Future Work

In this thesis, I presented the work on probing homogeneous Fermi gases using a Laguerre-Gaussian beam. We developed a technique to spatially select the center part of the cloud trapped in a harmonic trap by optically pumping the edge of the cloud to the states dark to the probe light. As a proof-of-principle experiment, we applied this technique to a weakly interacting Fermi gas and directly observed the Fermi surface in momentum distribution. Motivated by the success of this result, we combined the same technique with RF spectroscopy to study strongly interacting Fermi gases. We locally measured the Tan's contact as a function of temperature at unitarity and compared to various many-body theories. We then measured the spectral function of the gas above T_c across BCS-BEC crossover. This study was important to understand the pairing phenomena in the normal phase of the strongly interacting Fermi gases as it is related to the pseudogap phase in high T_c superconductors. Because we were probing the homogeneous sample, we were able to rigorously quantify our measurement and extract quantities like quasi-particle residue (Z), effective mass and Hartree energy shift.

For the second half of my thesis, I presented the work on the construction of the new generation Fermi gas apparatus. This apparatus was a significant upgrade from the old one. The old apparatus, which was the first degenerate Fermi gas machine in the world, was undoubtedly one of the best in the world. The amount of scientific results it produced has been remarkable. However, after 17 years it was getting a little unstable and unreliable. With the advancement that has happened in the last decade in optics and software, it surely needed a major upgrade. The

main problem with the old apparatus was its poor optical access and a long cycle time of around 2.5 minutes. The lasers needed frequent relocking and realignment, some of the old electronics needed to be replaced on weekly basis and the computer control and data acquisition software was running on Windows XP. Keeping all these things in mind, we decided to build a new lab from scratch. We designed a three-chamber setup to trap a large number of potassium atoms and at the same time allow good optical access and a large numerical aperture in the science cell. The science cell in this apparatus is AR-coated on both sides to allow lattice experiments. The double-MOT setup with a dark SPOT repump allowed us to have a large potassium atom numbers. We also implemented the dark molasses cooling scheme with D1-transition of ^{40}K to cool the cloud below the Doppler temperature before loading the magnetic quadrupole trap. This cooling stage enabled us to retain a large potassium number while transferring atoms to the science cell. The QUIC trap, which has only three coils, was constructed to provide a large optical access. The quadrupole coils used in the QUIC trap also served as bias coil to reach large magnetic fields for Feshbach resonance. After evaporation in the QUIC trap and an optical dipole trap, we were able to get a degenerate Fermi gas at a temperature of around $0.15T_F$ with 50,000 atoms.

In terms of scientific goals, we planned to study strongly interacting quenched Fermi gases. For example, we could have studied the dynamic Tan's relation which connects the release energy of Fermi gases before and after the quench to Tan's contact. We could have also studied the dynamics of Tan's contact after the quench. This would have allowed us to get an insight into the timescale of short-range correlation.

Further work on momentum-resolved RF spectroscopy is still needed to understand the phase diagram completely. We had only measured the spectral as a function of interaction strength at fixed temperature. We had performed some initial experiments to look at the gas as a function of temperature at various interaction strengths across the crossover. This would have also allowed us to test our model over a wide range of the phase diagram. In another experiment, we had also tried to develop a new technique to probe the "unoccupied" branch of the spectral function. This technique, which required injecting atoms to strongly interacting states, was analogous to the

inverse-ARPES experiments in condensed matter and could have allowed us to measure the gap in the superfluid phase. However, the signal-to-noise ratio we were getting was too poor to perform any meaningful measurements and needed some improvement.

However, in the fall of 2016, due to the sad and unexpected demise of Debbie, some of her projects needed to be consolidated. The Fermi gas experiment we built is now converted to a strongly interacting BEC experiment. The machine has a capability to study ^{39}K and ^{85}Rb strongly interacting BECs. The quenched ^{85}Rb BEC experiments have definitely excited both experimental and theoretical AMO communities, and the study of these systems seems quite important to understand various few-body and many-body phenomena. I look forward to seeing great scientific research from this machine in coming years.

Bibliography

[1] C. A. R. Sá De Melo, "When fermions become bosons: Pairing in ultracold gases," Physics Today, vol. 61, pp. 45–51, Oct. 2008.

[2] D. S. Jin, B. DeMarco, and S. Papp, "Exploring a quantum degenerate fermi gas," AIP Conference Proceedings, vol. 551, no. 1, pp. 414–425, 2001.

[3] J. P. Gaebler, J. T. Stewart, T. E. Drake, D. S. Jin, A. Perali, P. Pieri, and G. C. Strinati, "Observation of pseudogap behavior in a strongly interacting Fermi gas," Nat. Phys., vol. 6, pp. 569–573, Aug. 2010.

[4] R. Haussmann, W. Rantner, S. Cerrito, and W. Zwerger, "Thermodynamics of the BCS-BEC crossover," Physical Review A - Atomic, Molecular, and Optical Physics, vol. 75, p. 23610, Feb. 2007.

[5] H. Hu, X. J. Liu, and P. D. Drummond, "Universal contact of strongly interacting fermions at finite temperatures," New Journal of Physics, vol. 13, no. 3, p. 35007, 2011.

[6] F. Palestini, A. Perali, P. Pieri, and G. C. Strinati, "Temperature and coupling dependence of the universal contact intensity for an ultracold Fermi gas," Physical Review A - Atomic, Molecular, and Optical Physics, vol. 82, p. 21605, Aug. 2010.

[7] J. E. Drut, T. A. Lähde, and T. Ten, "Momentum distribution and contact of the unitary Fermi gas," Physical Review Letters, vol. 106, p. 205302, May 2011.

[8] N. Navon, S. Nascimbène, F. Chevy, and C. Salomon, "The equation of state of a low-temperature Fermi gas with tunable interactions," Science, vol. 328, no. 5979, pp. 729–732, 2010.

[9] E. Braaten, "Universal relations for fermions with large scattering length," in Lecture Notes in Physics (W. Zwerger, ed.), vol. 836 of Lecture Notes in Physics, pp. 193–231, Springer Berlin / Heidelberg, 2012.

[10] R. Haussmann, M. Punk, and W. Zwerger, "Spectral functions and rf response of ultracold fermionic atoms," Physical Review A - Atomic, Molecular, and Optical Physics, vol. 80, p. 63612, Dec. 2009.

[11] B. Demarco, Quantum Behavior of an Atomic Fermi Gas. PhD thesis, University of Colorado, 2001.

[12] E. M. Lifshitz and L. P. Pitaevskii, Statistical Physics, Part 2, vol. 9 of Landau and Lifshitz Course of Theoretical Physics. Butterworth-Heinemann, 1980.

[13] W. Ketterle and M. W. Zwierlein, "Making, probing, and understanding Fermi gases," in Ultracold Fermi Gases, Proceedings of the International School of Physics "Enrico Fermi" Course CLXIV (M. Inguscio, W. Ketterle, and C. Salomon, eds.), (Amsterdam), IOS Press, 2006.

[14] P. Törmä and K. Sengstock, Quantum Gas Experiments: Exploring Many-body States. Cold atoms, World Scientific Publishing Company Incorporated, 2014.

[15] B. DeMarco, "Onset of Fermi Degeneracy in a Trapped Atomic Gas," Science, vol. 285, pp. 1703–1706, 1999.

[16] C. Regal and D. S. Jin, "Experimental realization of BCS-BEC crossover physics with a Fermi gas of atoms," Adv. Atom. Mol. Opt. Phys., vol. 54, p. 1, 2005.

[17] S. Giorgini, L. P. Pitaevskii, and S. Stringari, "Theory of ultracold atomic fermi gases," Rev. Mod. Phys., vol. 80, pp. 1215–1274, Oct 2008.

[18] C. Chin, R. Grimm, P. Julienne, and E. Tiesinga, "Feshbach resonances in ultracold gases," Reviews of Modern Physics, vol. 82, pp. 1225–1286, Apr. 2010.

[19] C. Pethick and H. Smith, Bose-Einstein Condensation in Dilute Gases. Cambridge University Press, 2002.

[20] V. Gurarie and L. Radzihovsky, "Resonantly paired fermionic superfluids," Annals of Physics, vol. 322, no. 1, pp. 2 – 119, 2007. January Special Issue 2007.

[21] S. Nascimbène, N. Navon, K. J. Jiang, F. Chevy, and C. Salomon, "Exploring the thermodynamics of a universal Fermi gas," Nature, vol. 463, no. 7284, pp. 1057–1060, 2010.

[22] Y. Sagi, T. E. Drake, R. Paudel, R. Chapurin, and D. S. Jin, "Probing local quantities in a strongly interacting fermi gas," Journal of Physics: Conference Series, vol. 467, no. 1, p. 012010, 2013.

[23] B. Mukherjee, Z. Yan, P. B. Patel, Z. Hadzibabic, T. Yefsah, J. Struck, and M. W. Zwierlein, "Homogeneous Atomic Fermi Gases," ArXiv e-prints, Oct. 2016.

[24] T. E. Drake, Measuring local properties of a Fermi gas in the BCS-BEC crossover. PhD thesis, University of Colorado, 2015.

[25] W. Ketterle, D. S. Durfee, and D. M. Stamper-Kurn, "Making, probing and understanding Bose-Einstein condensates," eprint arXiv:cond-mat/9904034, Apr. 1999.

[26] A. L. Gaunt, T. F. Schmidutz, I. Gotlibovych, R. P. Smith, and Z. Hadzibabic, "Bose-Einstein Condensation of Atoms in a Uniform Potential," Physical Review Letters, vol. 110, p. 200406, May 2013.

[27] T. E. Drake, Y. Sagi, R. Paudel, J. T. Stewart, J. P. Gaebler, and D. S. Jin, "Direct observation of the Fermi surface in an ultracold atomic gas," Physical Review A - Atomic, Molecular, and Optical Physics, vol. 86, Mar. 2012.

[28] M. Clifford, J. Arlt, J. Courtial, and K. Dholakia, "High-order laguerre gaussian laser modes for studies of cold atoms," Optics Communications, vol. 156, no. 46, pp. 300 – 306, 1998.

[29] M. Horikoshi, S. Nakajima, M. Ueda, and T. Mukaiyama, "Measurement of universal thermodynamic functions for a unitary Fermi gas," Science, vol. 327, no. 5964, pp. 442–445, 2010.

[30] M. J. H. Ku, A. T. Sommer, L. W. Cheuk, and M. W. Zwierlein, "Revealing the Superfluid Lambda Transition in the Universal Thermodynamics of a Unitary Fermi Gas," Science, vol. 335, no. 6068, pp. 563–567, 2012.

[31] J. T. Stewart, J. P. Gaebler, and D. S. Jin, "Using photoemission spectroscopy to probe a strongly interacting Fermi gas," Nature, vol. 454, pp. 744–747, Aug. 2008.

[32] Q. Chen, J. Stajic, S. Tan, and K. Levin, "BCS-BEC crossover: From high temperature superconductors to ultracold superfluids," Physics Reports, vol. 412, no. 1, pp. 1–88, 2005.

[33] S. Tan, "Annals of Physics Energetics of a strongly correlated Fermi gas," Annals of Physics, vol. 323, pp. 2952–2970, 2008.

[34] S. Tan, "Large momentum part of a strongly correlated Fermi gas," Annals of Physics, vol. 323, pp. 2971–2986, 2008.

[35] S. Tan, "Generalized virial theorem and pressure relation for a strongly correlated Fermi gas," Annals of Physics, vol. 323, pp. 2987–2990, 2008.

[36] E. Braaten, D. Kang, and L. Platter, "Exact Relations for a Strongly-interacting Fermi Gas near a Feshbach Resonance," Phys. Rev. Lett., vol. 100, p. 25, 2008.

[37] S. Zhang and A. J. Leggett, "Universal properties of the ultracold Fermi gas," Physical Review A - Atomic, Molecular, and Optical Physics, vol. 79, p. 23601, 2009.

[38] J. T. Stewart, J. P. Gaebler, T. E. Drake, and D. S. Jin, "Verification of universal relations in a strongly interacting Fermi gas," Physical Review Letters, vol. 104, p. 235301, June 2010.

[39] E. D. Kuhnle, H. Hu, X. J. Liu, P. Dyke, M. Mark, P. D. Drummond, P. Hannaford, and C. J. Vale, "Universal behavior of pair correlations in a strongly interacting Fermi gas," Physical Review Letters, vol. 105, p. 70402, Aug. 2010.

[40] G. B. Partridge, K. E. Strecker, R. I. Kamar, M. W. Jack, and R. G. Hulet, "Molecular probe of pairing in the BEC-BCS crossover," Physical Review Letters, vol. 95, p. 20404, July 2005.

[41] F. Werner, L. Tarruell, and Y. Castin, "Number of closed-channel molecules in the BEC-BCS crossover," European Physical Journal B, vol. 68, no. 3, pp. 401–415, 2009.

[42] Z. Yu, G. M. Bruun, and G. Baym, "Short-range correlations and entropy in ultracold-atom Fermi gases," Physical Review A - Atomic, Molecular, and Optical Physics, vol. 80, p. 23615, Aug. 2009.

[43] T. Enss, R. Haussmann, and W. Zwerger, "Viscosity and scale invariance in the unitary Fermi gas," Annals of Physics, vol. 326, no. 3, pp. 770–796, 2011.

[44] E. D. Kuhnle, S. Hoinka, P. Dyke, H. Hu, P. Hannaford, and C. J. Vale, "Temperature dependence of the universal contact parameter in a unitary Fermi gas," Physical Review Letters, vol. 106, p. 170402, Apr. 2011.

[45] C. A. Regal, M. Greiner, and D. S. Jin, "Observation of resonance condensation of fermionic atom pairs," Physical review letters, vol. 92, p. 040403, Jan. 2004.

[46] Z. Fu, P. Wang, L. Huang, Z. Meng, and J. Zhang, "Momentum-resolved raman spectroscopy of bound molecules in ultracold fermi gas," Phys. Rev. A, vol. 86, p. 033607, Sep 2012.

[47] A. Schirotzek, Y. I. Shin, C. H. Schunck, and W. Ketterle, "Determination of the superfluid gap in atomic Fermi gases by quasiparticle spectroscopy," Physical Review Letters, vol. 101, no. October, pp. 1–4, 2008.

[48] Y. Sagi, T. E. Drake, R. Paudel, and D. S. Jin, "Measurement of the homogeneous contact of a unitary Fermi gas," Physical Review Letters, vol. 109, p. 220402, Nov. 2012.

[49] Y. Sagi, T. E. Drake, R. Paudel, R. Chapurin, and D. S. Jin, "Breakdown of the Fermi Liquid Description for Strongly Interacting Fermions," Physical Review Letters, vol. 114, no. 075301, pp. 1–5, 2015.

[50] M. Scully and M. Zubairy, Quantum Optics. Cambridge University Press, 1997.

[51] K. M. O'Hara, S. L. Hemmer, M. E. Gehm, S. R. Granade, and J. E. Thomas, "Observation of a strongly interacting degenerate Fermi gas of atoms," Science, vol. 298, pp. 2179–2182, 2002.

[52] L. Luo and J. Thomas, "Thermodynamic Measurements in a Strongly Interacting Fermi Gas," J. Low Temp. Phys., vol. 154, no. 1, pp. 1–29, 2009.

[53] J. P. Gaebler, Photoemission spectroscopy of a strongly interacting Fermi gas. PhD thesis, University of Colorado, 2010.

[54] A. Fetter and J. Walecka, Quantum Theory of Many-particle Systems. Dover Books on Physics, Dover Publications, 2003.

[55] A. Damascelli, Z. Hussain, and Z. X. Shen, "Angle-resolved photoemission studies of the cuprate superconductors," Reviews of Modern Physics, vol. 75, pp. 473–541, Apr. 2003.

[56] W. Schneider and M. Randeria, "Universal short-distance structure of the single-particle spectral function of dilute Fermi gases," Physical Review A - Atomic, Molecular, and Optical Physics, vol. 81, p. 21601, Feb. 2010.

[57] C. Chin and P. S. Julienne, "Radio-frequency transitions on weakly bound ultracold molecules," Physical Review A - Atomic, Molecular, and Optical Physics, vol. 71, p. 12713, Jan. 2005.

[58] E. V. H. Doggen and J. J. Kinnunen, "Momentum-resolved spectroscopy of a Fermi liquid," arXiv:1411.7207, Nov. 2014.

[59] J. O'Hanlon, A User's Guide to Vacuum Technology. John Wiley & Sons, 2003.

[60] H. Metcalf and P. van der Straten, Laser Cooling and Trapping. Graduate Texts in Contemporary Physics, Springer New York, 2001.

[61] T. Tiecke, "Properties of potassium," University of Amsterdam, The Netherlands, Thesis, pp. 12–14, 2010.

[62] G. Modugno, C. Benkő, P. Hannaford, G. Roati, and M. Inguscio, "Sub-doppler laser cooling of fermionic 40 k atoms," Physical Review A, vol. 60, no. 5, p. R3373, 1999.

[63] D. McKay, D. Jervis, D. Fine, J. Simpson-Porco, G. Edge, and J. Thywissen, "Low-temperature high-density magneto-optical trapping of potassium using the open 4 s- 5 p transition at 405 nm," Physical Review A, vol. 84, no. 6, p. 063420, 2011.

[64] D. R. Fernandes, F. Sievers, N. Kretzschmar, S. Wu, C. Salomon, and F. Chevy, "Sub-doppler laser cooling of fermionic 40k atoms in three-dimensional gray optical molasses," EPL (Europhysics Letters), vol. 100, no. 6, p. 63001, 2012.

[65] A. Aspect, E. Arimondo, R. Kaiser, N. Vansteenkiste, and C. Cohen-Tannoudji, "Laser cooling below the one-photon recoil energy by velocity-selective coherent population trapping: theoretical analysis," JOSA B, vol. 6, no. 11, pp. 2112–2124, 1989.

[66] C. Salomon, J. Dalibard, W. Phillips, A. Clairon, and S. Guellati, "Laser cooling of cesium atoms below 3 μk," EPL (Europhysics Letters), vol. 12, no. 8, p. 683, 1990.

[67] H. J. Lewandowski, D. Harber, D. L. Whitaker, and E. A. Cornell, "Simplified system for creating a bose–einstein condensate," Journal of low temperature physics, vol. 132, no. 5-6, pp. 309–367, 2003.

[68] W. Petrich, M. H. Anderson, J. R. Ensher, and E. A. Cornell, "Stable, tightly confining magnetic trap for evaporative cooling of neutral atoms," Phys. Rev. Lett., vol. 74, pp. 3352–3355, Apr 1995.

[69] C. J. Myatt, Bose-Einstein condensation experiment in a dilute vapor of rubidium. PhD thesis, UNIVERSITY OF COLORADO AT BOULDER, 1997.

[70] R. Grimm, M. Weidemüller, and Y. B. Ovchinnikov, "Optical dipole traps for neutral atoms," Advances in atomic, molecular, and optical physics, vol. 42, pp. 95–170, 2000.